中国科学技术大学

博士学位论文

RHIC 能区金核-金核对撞中

重味夸克衰变电子椭圆流

和激发态粲介子产生的测量

作者姓名：　　纪媛婧

学科专业：　　粒子物理与原子核物理

导师姓名：　　邵明 教授　董昕 研究员　唐泽波 副教授

完成时间：　　二〇二〇年十二月八日

University of Science and Technology of China

A dissertation for doctor's degree

Measurements of elliptic flow of heavy flavor electrons and D^{*+} production in Au+Au collisions at RHIC

Author: Yuanjing Ji

Speciality: Particle and Nuclear Physics

Supervisors: Prof. Ming Shao, Prof. Xin Dong, Prof. Zebo Tang

Finished time: December 8, 2020

中国科学技术大学学位论文原创性声明

本人声明所呈交的学位论文，是本人在导师指导下进行研究工作所取得的成果。除已特别加以标注和致谢的地方外，论文中不包含任何他人已经发表或撰写过的研究成果。与我一同工作的同志对本研究所做的贡献均已在论文中作了明确的说明。

作者签名：_____　　　签字日期：_____

中国科学技术大学学位论文授权使用声明

作为申请学位的条件之一，学位论文著作权拥有者授权中国科学技术大学拥有学位论文的部分使用权，即：学校有权按有关规定向国家有关部门或机构送交论文的复印件和电子版，允许论文被查阅和借阅，可以将学位论文编入《中国学位论文全文数据库》等有关数据库进行检索，可以采用影印、缩印或扫描等复制手段保存、汇编学位论文。本人提交的电子文档的内容和纸质论文的内容相一致。

保密的学位论文在解密后也遵守此规定。

☑公开　□保密（____ 年）

作者签名：_____　　　导师签名：_____

签字日期：_____　　　签字日期：_____

摘　　要

格点量子色动力学（QCD）计算表明极端相对论重离子对撞产生的高温环境会导致核物质中夸克和胶子的解禁闭，形成一种具有部分子自由度的新的物质形态——夸克胶子等离子体（Quark Gluon Plasma，QGP）。QGP 是研究强相互作用的理想实验室。相对论重离子对撞实验的一个重要目标就是寻找 QGP，并研究它的特性。

重味夸克（粲夸克和底夸克）是研究 QGP 早期动力学性质的一个独特的探针。由于质量远大于 QCD 能标和 QGP 的典型温度，重味夸克在相对论重离子碰撞中主要产生于 QGP 形成之前的初始硬散射过程。该过程可以用微扰 QCD 计算。当 QGP 形成之后，重味夸克与 QGP 发生相互作用，并随着 QGP 的冷却而强子化。通过测量末态重味强子的产生，可以研究重味夸克与 QGP 的相互作用，并进而研究 QGP 的特性。由于其热化时间与 QGP 的寿命相当甚至更长，末态重味强子携带了重味夸克与 QGP 的作用历史信息。因此，重味夸克是研究 QGP 性质的一种"穿越探针"（Penetrating Probe）。

本论文围绕 RHIC 能区相对论重离子碰撞中重味强子的产生开展了三部分工作：1）STAR 实验 54.4 与 27 GeV 金核-金核对撞中重味衰变电子椭圆流的实验研究；2）STAR 实验 200 GeV 金核-金核对撞中激发态粲介子 D^{*+} 产生的实验研究；3）sPHENIX 实验 200GeV 金核-金核对撞中 Λ_c^+ 产生的模拟研究。

重味夸克与各向异性膨胀的 QGP 相互作用会导致末态重味强子的各向异性流。STAR 利用重味径迹探测器（Heavy Flavor Tracker，HFT）在 2014-2016 年采集的 200 GeV 金核-金核对撞数据测量了 D^0 介子的椭圆流，为重味夸克在 QGP 中的输运特性研究提供了重要的实验数据。将重味夸克椭圆流测量扩展到更低能的相对论重离子碰撞中可以研究输运特性对 QGP 温度的依赖关系。论文利用 STAR 实验在 2017-2018 年采集的 54.4 GeV 和 27 GeV 金核-金核对撞数据，测量了两种对撞能量下重味衰变电子的椭圆流，并与 200 GeV 对撞中的结果进行了比较。发现在质心系能量为 54.4 GeV 的金核-金核对撞中，重味夸克衰变电子也具有显著的椭圆流，其幅度与 200 GeV 金核-金核对撞中的重味衰变电子椭圆流相当，在 $p_T > 1$ GeV/c 区间里与轻强子椭圆流相近。该结果表明，粲夸克在质心系能量低至 54.4 GeV 的金核-金核对撞中依然同介质有很强的相互作用。而在 27 GeV 金核-金核对撞中，重味衰变电子的椭圆流在误差范围内与 0 符合，低于 54.4 GeV 对撞中的结果（显著度：1.6σ），这表明在 27 GeV 对撞中粲夸克可能未完全热化。这些结果可以为温度依赖的重味夸克输运特性如空间扩散系数 $\mathcal{D}_s$ 的限制提供重要的实验数据。

重味夸克与 QGP 的相互作用还会改变重味夸克的动量分布和强子化过程，导致重味强子的核修正因子 R_{AA} 偏离 1。STAR 利用 HFT 对 200GeV 金核-金核对撞中 D^0 的核修正因子进行了精确测量，发现在中心对撞中 D^0 在所有横动量范围里都存在产额压低现象。由于粲夸克数在 QGP 演化过程中是守恒的，这表明在 QGP 强子化过程中，不同粲强子组分发生了改变。本论文对 200GeV 金核-金核对撞中 D^{*+} 产生的实验研究是对 D^0 测量的一个非常重要的补充。此外，有理论研究表明，由于 QGP 的作用，D^{*+} 的质量谱有可能会显著展宽，衰变时间可缩短到与 QGP 的热力学冻结时间相当。这可以通过测量 D^{*+} 与 D^0 的产额比来进行实验验证。本论文通过 $D^{*+} \rightarrow D^0\pi^+$，$D^0 \rightarrow K^-\pi^+$ 来重建 D^{*+}，测量了其产额及其与 D^0 产额的比例。测量结果发现 D^{*+}/D^0 产额比值随 p_T 的依赖关系同 PYTHIA 计算得到的质子-质子对撞中的理论预期符合得很好，说明 D^{*+} 存在同 D^0 相似的产额压低，D^{*+} 的强子化过程与 D^0 类似。他们的整体产额压低意味着有其他粲强子具有产额增强现象。此外，研究发现 D^{*+}/D^0 没有明显的中心度依赖关系，与 K^{*0}/K^- 的中心度依赖关系有明显差别，这一结果并不支持 D^{*+} 的衰变寿命与 QGP 热力学冻结时间相当的理论计算结果。

STAR 研究发现在 200 GeV 金核-金核碰撞中 Λ_c^+ 粒子具有产额增强现象，与夸克聚并的强子化机制理论预期相符。但由于统计误差较大，其物理根源还存在较大的争论。如能在预期于 2023 年开始运行的 sPHENIX 实验中安装新一代硅像素探测器，有望在未来提供高精度的重味夸克测量。本论文最后一部分对包含了新一代硅像素探测器的 SPHENIX 实验中重味强子的测量进行了细致的蒙特卡洛模拟研究，得到了粲重子信号显著度和 Λ_c^+/D^0 测量精度。这为这一探测器升级和未来的高精度重味夸克测量提供了重要的参考。

关键词：夸克胶子等离子体；重味夸克；粲夸克；电子；椭圆流；激发态粲介子；横动量谱；能量损失；粲重子

ABSTRACT

Lattice QCD calculations predict that, in relativistic heavy ion collisions where temperature is extremely high, quarks and gluons will deconfine from bound hadrons, and a new matter state, Quark-Gluon Plasma (QGP), will be formed. The matter in early universe is believed to be in QGP state a few microseconds after the Big Bang. This strong coupling QCD matter created in the heavy ion collisions is a natural laboratory to study strong interactions. One of the primary goals for relativistic heavy ion collisions, is to produce QGP and study its properties.

The masses of heavy quarks (HQ) are much larger than QCD scale, so their production cross sections can be calculated by perturbative QCD. As their masses are much larger than QGP typical temperature, their thermal production in the medium is suppressed. Thus, they are dominantly produced in the initial hard scattering processes with large momentum transfer before the formation of QGP in the heavy ion collisions. The thermalization time of heavy quarks is comparable or longer than the lifetime of QGP created in heavy-ion collisions. Therefore, their final kinematics still carry dynamic information about their interaction with the QGP medium.

When heavy quarks transport through the QGP medium, they interact with the background partons in the medium by elastic scattering and gluon radiation. At low momentum, heavy quarks and medium interactions are dominated with elastic scattering. Since heavy quark masses are much larger than the medium temperature, their interactions with the medium can be approximated as multiple elastic scattering with relatively small momentum transfer ($q^2 \sim T^2$), in analogy to "Brownian motion" in molecular physics. Heavy quark motion inside the QGP can therefore be described by a stochastic Langevin simulation. One of the transport parameters, often characterized by a spatial diffusion coefficient $\mathcal{D}_s$ reveals the QGP coupling strength. The $\mathcal{D}_s$ can be constrained by analyzing the experimental data of nuclear modification factor R_{AA} and elliptic flow v_2 of heavy flavor hadrons or their decay daughters at low momentum, and compared to phenomenological models. The strength of measured D^0 v_2 at low p_T at RHIC top energy and LHC is comparable to those of light hadrons. A local peak structure is observed in the D^0 R_{AA} around $p_T \sim 2$ GeV/c, known as "flow bump". It is inferred from current measurements in comparison with model calculations that D^0 meson has obtained collectivity and may have been thermalized in the medium. Based on the available experimental data, the current understanding of the $2\pi T \mathcal{D}_s$ has been constrained

to be around 2–5 near the critical temperature T_c, while the temperature dependence of $\mathcal{D}_s$ has an appreciable uncertainty at higher temperature regions.

The heavy quark (HQ) energy loss mechanism in the medium can be learned from the modification of p_T spectrum of final state heavy flavor hadrons. The gluon radiation process is expected to be suppressed with the increase of parton mass at a given momentum, known as the "dead cone" effect. Therefore, the radiative energy loss of quarks and gluons should follow a mass hierarchy: $\Delta E_b < \Delta E_c < \Delta E_{u,d,s} < \Delta E_g$. Intuitively, HQ R_{AA} is then expected to be less suppressed if only considering radiative energy loss. However, the measured R_{AA} for charm mesons or their decay products from RHIC top energy and LHC is comparable to those of light hadrons up to $p_T \sim 10$ GeV/c. This striking observation reveals the importance of elastic energy loss for heavy quark energy loss mechanism in the QGP. In addition, the mass hierarchy of R_{AA} is also affected by the initial parton spectra and hadronization process. Recently, a charm-bottom hierarchy at intermediate p_T is observed in measurements of R_{AA} of bottom decay daughters from LHC. Based on the theory predictions, the collisional energy loss dominates at low momentum, while heavy quarks loss energy mainly through gluon radiation at high momentum. However, it is not very clear at which momentum will the radiative energy loss takes over the elastic ones.

In this thesis, measurements of the elliptic flow of heavy flavor electron (e^{HF}) in Au+Au collisions at $\sqrt{s_{NN}} = 27$, 54.4 GeV are reported. By lowering the collision energy, one would expect the initial temperature the QGP medium can reach will be different. Therefore, the measurements from different collision energies are expected to offer sensitive information on the temperature dependence of various QGP properties. The measurements are based on the data samples collected during RHIC year run 2017 and 2018 by the Soldnoidal Tracker at RHIC (STAR) detector with a statistics ten times of that in Au+Au $\sqrt{s_{NN}} = 62.4$ GeV collisions collected in year 2010. In this analysis, electrons are identified by combining the energy loss information from the Time Projection Chamber (TPC) subsystem and particle velocity information from the Time Of Flight (TOF) subsystem. The main background sources in this analysis are so called photonic electrons, including electrons originated from photon conversions in the detector material and Dalitz decay electrons from light mesons π^0/η. The yield of photonic electrons can be evaluated by a reconstruction method and removed from the total electrons statistically. The reconstruction method involves a finite efficiency which is estimated by full detector simulation using the embedding technique. The v_2 of inclusive electrons is calculated using the event plane η-sub method. The elliptic flow

of photonic electrons is computed using simulations with the input hadron v_2 from real data.

The results show that e^{HF} has obtained a large v_2 in Au+Au $\sqrt{s_{\mathrm{NN}}} = 54.4$ GeV collisions that is comparable to the e^{HF} v_2 in 200 GeV collisions. The strength of e^{HF} v_2 is also comparable to those of light hadrons at $p_T > 1$ GeV/c in 54.4 GeV collisions. It indicates that charm quarks also have strong interactions with the QGP medium in Au+Au collisions at 54.4 GeV, although the collision energy is nearly a factor of 4 lower with respect to $\sqrt{s_{\mathrm{NN}}} = 200$ GeV. In Au+Au collisions at 27 GeV, the strength of e^{HF} v_2 is lower than 1.6σ lower than that in $\sqrt{s_{\mathrm{NN}}} = 54$ GeV collisions, and consistent with 0 within uncertainty. This might be a hint for that charm quark is not fully thermalized in Au+Au $\sqrt{s_{\mathrm{NN}}} = 27$ GeV collisions.

Measurements of D^{*+} production in Au+Au $\sqrt{s_{\mathrm{NN}}} = 200$ GeV collisions are reported too. The analysis is based on data samples collected by STAR with the Heavy Flavor Tracker (HFT) detector installed during 2014-2016. This measurement is complementary to the D^0 R_{AA} measurements to confirm that suppression of D^0 R_{AA} is not a result from the light quark component of D^0. Measurements of various charm meson species are needed and nearly 23% charm quarks will be hadronized to D^{*+} in ee/ep collisions. D^{*+} has a sizable feed-down contribution to the final state D^0 mesons with about 67% of D^{*+} decay to D^0. Model calculation predicts that D^{*+} life time might be shortened in high temperature and density environment. The final observed D^{*+} yield might get reduced if D^{*+} decays before kinematic freeze-out due to re-scatterings with the hadronic medium. D^{*+} is reconstructed through the channel $D^{*+} \to D^0\pi^+$, $D^0 \to K^-\pi^+$. The result shows that there is no obvious centrality dependence in the D^{*+}/D^0 yield ratio, which indicates that re-scattering effect does not have a significant impact on the final D^{*+} yields. Therefore the measurements of D^{*+} production are able to be combined with D^+ and D^0 measurements for better experimental precision to understand the charm quark energy loss as well as other transport properties. The p_T dependence of D^{*+}/D^0 yield ratio is consistent with PYTHIA calculation in p+p collisions at 200 GeV. As there is no modification of D^{*+}/D^0 yield ratio observed in Au+Au collisions, it can be inferred that D^{*+} R_{AA} has similar suppression as D^0 R_{AA} and D^0 R_{AA} modification is not resulted from D^{*+} feed down. It supports the conclusion that the charm quark has a strong interaction with the medium.

Looking forward towards the future heavy flavor program in heavy ion collisions, the sPHENIX detector is a new generation detector for measurements utilizing hard probes. The innermost tracking system is the Monolithic Active Pixel Sensor Vertex

Detector (MVTX). The sPHENIX detector also features as high trigger and DAQ rate. Precise heavy flavor measurements over a broad momentum range are expected in the future sPHENIX detector. In the last part of this thesis, the simulation of charm baryon measurements in the sPHENIX detecor is reported. We first extract the detector performance for single tracks through full detector simulation, which will be set as the input for the followed fast simulation. From the simulation, we predict the Λ_c^+ signal significance and the statistic uncertainty of Λ_c^+/D^0 ratio in the future sPHENIX experiment in different centrality and p_T bins under different PID scenarios. A systematic measurement of charm baryon Λ_c^+ and possibly Λ_b production in $p+p$, $p+A$ and A+A collisions with the future sPHENIX detector will offer new insights towards heavy quark hadronization and may potentially shed light on the understanding of color confinement in QCD.

Key Words: Quark-Gluon Plasma; Heavy flavor; Charm quark; Electron; elliptic flow; D^{*+}; Spectra; Energy loss; Charm baryon

Contents

List of Figures

List of Tables

Chapter 1   Introduction

1.1   The elementary particles and interactions

The Standard Model (SM) is a theoretical framework that describes the behavior of all known subatomic particles and their interactions. It addresses three of four fundamental forces in the nature including the strong, weak and electromagnetic forces. Gravity is the only fundamental forces that is not included in the SM. The standard model is based on the gauge group SU(3)×SU(2)×U(1). The SU(3) component of the standard model derives from the strong interactions and SU(2)×U(1) is from electroweak interactions.
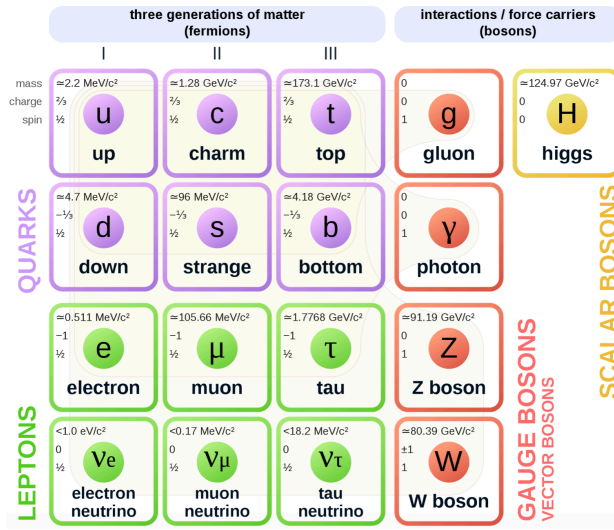
Fig. 1.1   Elementary particles described in the standard model. These particles are regarded as point-like particles and do not have inner structures. The first 3 column in the left are quarks and leptons. The particles in the fourth column are vector gauge bosons. The higgs boson is in the fifth column. Figure is from [1].

In the standard model, matters in the universe are made up of point-like matter particles, while particles interact with each other by the exchange of force carrier particles.The elementary particles described in the SM are summaried in Fig. 1.1. After 2012 when Higgs boson was discovered in the Large Hadron Collider (LHC), all of 17 elementary particles have been discovered in the experiments. According to their spin, these particles can be classified into fermions with half-integer spin and bosons with integer spin.

Force carrier particles are gauge bosons. The strong interaction carrier is gluon g, and weak interaction is Z^0 and $W^{\pm}$, and electromagnetic interaction is photon γ.

Apart from these gauge vector bosons, standard model also introduce a scalar boson *Higgs* to explain why fermions and weak interaction gauge bosons have mass. Matter particles are all fermions, including quarks and leptons. Both quarks and leptons can be classified into 3 generations according to their properties. There are totally 6 quarks flavors discovered in the universe, including up (u) and down (d), charm (c) and strange (s), top (t) and bottom (b). u, c and t carry $+\frac{2}{3}$ electron charge, while d, s and b carry $-\frac{1}{3}$ electron charge. Besides of electric charge, quarks carry color charge and weak charge. So they are able to participant in strong, electromagntic and weak interactions. The leptons also have 6 species, including electron (e^-) and electron neutrino(v_e), muon (μ^-) and muon neutrino (v_μ), tau (τ^-) and tau neutrino (v_τ). Charged leptons carry electric charge and weak charge and are able to participate in electroweak interaction. Neutrinos are neutral particles and only participate in weak interaction. All these particles have corresponding anti-particles with the same mass but opposite charges (such as electric charge, color charge and weak charge).

There still remain some important questions that standard model cannot answer, such as the nature of the dark matter, why matters and anti-matter is asymmetric, the non-zero mass of neutrino, and so on. Although standard model is not perfect, it has successfully explained almost all experimental results and given plenty of precise predictions up till now. In this thesis, we are focusing on the study of strong interactions.

1.2   Quantum Chromodynamics

In the standard model, Quantum chromodynamics (QCD) is the gauge field theory that describes the strong interactions of quarks and gluons based on SU(3) [2-7]. Additional quantum number is introduced for strong interactions, called color charge.

The first hint of the color charge was arguably the discovery of Δ^{++} baryon in 1951[8]. In the Quark Model which had been developed firstly, the flavor and spin of the Δ^{++} baryon is $|\Delta^{++}>= |u^\uparrow u^\uparrow u^\uparrow >$. The wave function of the Δ^{++} is symmetric in the quark model, while Δ^{++} is a fermion and must have an anti-symmetric wave function. This mystery can be solved by introducing a new quantum number, color [3-4]. Then the Δ^{++} baryon wave function can be arranged anti-asymmetric with its 3 quarks having different colors $|\Delta^{++}>= \epsilon^{ijk}|u_i^\uparrow u_j^\uparrow u_k^\uparrow >$. The number of color charge (N_c) can be obtained by measuring "R-value" in e^+e^- collisions. At energies well below Z res-

onance production threshold ($\sqrt{s} \sim 90\text{GeV}$), R is proportional to N_c [6, 9]

$$R_{e^+e^-} \equiv \frac{\sigma(e^+e^- \to \text{hadrons})}{\sigma(e^+e^- \to \mu^+\mu^-)} \simeq N_C \sum_{f=1}^{N_f} Q_f^2 \qquad (1.1)$$

There are 3 kinds of color charge (N_c=3): red, green and blue. Every quark carries one of the three color charges (anti-color charge for anti-quarks) and every gluon carries one color charge and one anti-color charge.

The Lagrangian of QCD is given by [10]

$$\mathcal{L} = \sum_q \overline{\psi}_{q,a}(i\gamma^\mu \partial_\mu \delta_{ab} - g_s\gamma^\mu t_{ab}^C \mathcal{A}_\mu^C - m_q\delta_{ab})\psi_{q,b} - \frac{1}{4}F_{\mu\nu}^A F^{A\mu\nu} \qquad (1.2)$$

where repeated indices are summed over. The γ^μ are the Dirac γ-matrices. The $\psi_{q,a}$ are quark-field spinors. The q refer to the quark flavor and a is the color index running from 1 to $N_c = 3$. m_q is the quark mass. The $\mathcal{A}_\mu^C$ are the gluon fields with index C ($C = 1, ..., N_c^2 - 1 = 8$, which corresponds to 8 kinds of gluons). t_{ab}^C are the generators of the SU(3) group encoding the fact that a quark's color can be rotated by its interaction with a gluon in SU(3) space. The field tensor $F_{\mu\nu}^A$ is given as follows:

$$F^A\mu\nu = \partial_\mu \mathcal{A}_\nu^A - \partial_\nu \mathcal{A}_\mu^A - g_s f_{ABC}\mathcal{A}_\mu^B \mathcal{A}_\nu^C \qquad (1.3)$$

where f_{ABC} are the structure constants of the SU(3) group with $[t^A, t^B] = if_{ABC}t^C$. The quantity g_s is the QCD coupling constant, which is often written as $\alpha_s = g_s^2/4\pi$. The coupling constant α_s is the only fundamental parameter in QCD besides quarks mass.

1.2.1 The running coupling

In Quantum Electro-Dynamics (QED), the virtual electron-position pair excited by the propagator photon would partially screen the interaction between two electric charges. This screening effect results in the scale dependence of the QED coupling constant. It would increase if the two electric charges get closer. Such screening effect also exits in QCD. As is shown in Fig. 1.2 Feynman diagrams (a), quark and anti-quark pair is excited in the vacuum due to the presence of color charge. However, different from photons, gluons carry color charges, so they could have self-interaction. Gluons could scatter and absorb gluons in the QCD vacuum, as shown in Fig. 1.2(b). The colored gluon clouds excited around the two color charges would enhance the interaction between the color charges (anti-screening).

Let's go back to the QCD calculations. The value of the QCD coupling constant α_s depends on the renormalization scale μ. The dependence can be written as the following
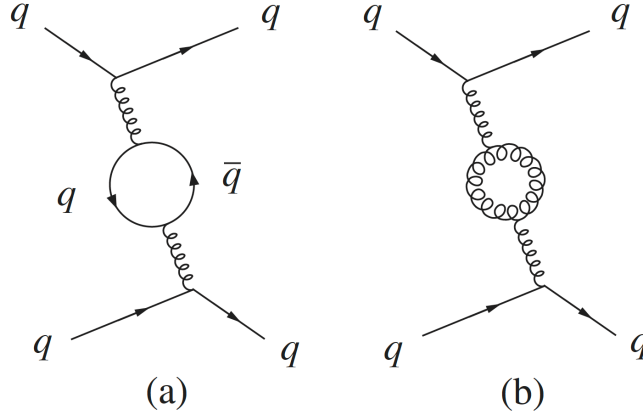
Fig. 1.2   The Feynman diagrams illustrate the lowest order of screening (a) and anti-screening (b) effect between the color charges in the polarization of vacuum.

normalization group equation:

$$\mu^2 \frac{d\alpha_s(\mu_R^2)}{d\mu_R^2} = \frac{d\alpha_s(\mu^2)}{d\ln\mu_R^2} = \beta(\alpha_s(\mu^2)),$$

$$\beta(\alpha_s) = -\alpha_s^2(b_0 + b1\alpha_s + b2\alpha_s^2 + ...)$$
(1.4)

The 1-loop β-function coefficient $b_0 = (11C_A - 2n_f)/(12\pi) = (33 - 2n_f)/12\pi$ where n_f is the number of "light" quark flavors whose mass is lower than μ. Opposite to QED, the sign of the QCD β-function in Eq. 1.4 is negative. This gives rise to the phenomena that as the increase of energy scales the α_s becomes smaller. The leading order of the perturbative solution for α_s is:

$$\alpha_s(\mu) \approx \frac{\alpha_s(\mu_0^2)}{1 + b_0\alpha_s(\mu_0^2)ln(\mu^2/\mu_0^2)} = \frac{1}{b_0 ln(\mu^2/\Lambda_{QCD}^2)}$$
(1.5)

The perturbation approximation is only valid with scales $\mu \gg \Lambda_{QCD}$ ($\alpha_s \ll 1$). The non-perturbative constant Λ_{QCD} is determined experimentally ($\Lambda_{QCD} \simeq 200$ MeV). When μ is taken close to the momentum transfer Q, α_s represent the effective strength of the QCD interaction in the process. Fig. 1.3 shows the experimental measurements of α_s at different energy scales. It is a common practice to take the reference μ_0 at the mass of Z boson since some precise measurements come from Z decay. The current world average is $\alpha_s(M_Z) = 0.1179 \pm 0.0010$ [11]. The curves in Fig. 1.3 shows the QCD prediction corresponding to the labeled $\alpha_s(M_Z)$. The QCD predicted value is consistent with data.

From Eq. 1.5 and Fig. 1.3, it is easily inferred that at very large momentum transfer $Q^2 \gg \Lambda_{QCD}^2$ or equivalent to short distance, quarks and gluons will not interact as $\alpha_s \to 0$, known as *asymptotic freedom*. This property allows us to solve QCD with pertabutive method at large energy scales, which we will discuss in next section. On the other hand, at low momentum transfer $Q^2 \sim \Lambda_{QCD}^2$ or equivalent to longer distance,

the QCD coupling will increase quickly. Pertubative QCD does not work anymore and should be replaced by non-pertubative QCD.

There have been no isolated quarks ever observed while all of the hadrons observed are in color neutral states. The *color confinement* has been a widely accepted hypothesis that hadrons must exist in *color singlet* state that the sum of all color charges equals to zero and quarks can only exist confined in hadrons. If the quark is forced to be seperated from the hadron, the interaction between the color charges will become extremely strong and the quarks cannot escape from the hadron state. Actually before the energy is high enough to separate the quark pair, new quark and anti-quark pairs pop up from the vacuum by the gluonic field between the quark pair and *hadronization* process would happen.
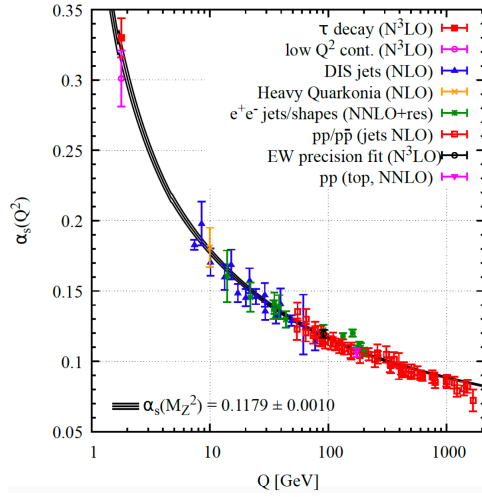
Fig. 1.3   Summary of current measurements of the QCD coupling constant α_s as a function of the energy scale Q. The measured data points agree with the curve from QCD calculations. The picture is taken from [11].

1.2.2   Approach to solving QCD

Two main first-principles approaches to solving QCD are Perturbative QCD (pQCD) and Lattice QCD (LQCD). There are also some phenomenological models such as bag model, constituent quark model, etc. We will only introduce pQCD and LQCD here.

1. Perturbative QCD

As we have mentioned above in α_s calculation, at large energy scale (roughly $Q \geqslant$ several GeV) when $\alpha_s \ll 1$, perturbation theory techniques are applicable. The idea for Perturbative QCD is that in a small coupling $\alpha_s \ll 1$, a given physics observable can be

written into series expansion of α_s [5]:

$$f = f_1\alpha_s + f_2\alpha_s^2 + f_3\alpha_s^3 + ... \tag{1.6}$$

One may just calculate the first n terms of the series with understanding that the remaining ones are small enough to be ignored. f_i is calculated from Feynman diagrams. Note that the calculations are still interactions between partons while there is no free quark or gluon observed. For more practical cases such as hard scattering process, pQCD relies on QCD *Factorization Theorems* as an approximation. It factorizes short-distance parton level process from perturbative calculations and long-distance physics from measurements [12-14]. Long-distance contributions are described as measurable universal functions, such as parton distribution functions, fragmentation functions, multi-parton correlation functions and so on. pQCD is successful in the calculation of heavy quark and jet production cross section in hard scattering process.

2. Lattice QCD

Lattice QCD is a non-perturbative implementation of field theory using the Feynman path integral approach [15]. It is QCD formulated on a discrete Euclidean space-time grid. The quark fields are defined at the vertices of the 4-dimensional lattice and the gluons propagate along the link of vertices, and then we are able to utilize numerical simulations to extrapolate the continuum limit to get the solution. This method requires properly modeling of the action and is suitable for the calculation of static quantities in QCD such as the hadron mass spectrum [5]. For quark gluon plasma related calculation, LQCD are build upon the Euclidean formulation of equilibrium thermodynamics. It plays important role in the calculation of thermodynamic property of quark-gluon plasma in local thermal equilibrium, but is challenging in describing time-dependent phenomena such as QGP transport coefficient.

1.3   QCD phase transition and QGP

Due to the "asymptotic freedom" property of α_s, one may imagine that at high temperatures, the interactions between quarks and gluons become weak due to the large thermal energies. When the temperature is high enough, the hadronic system dissolves into a system of quarks and gluons. This new phase of matter is called *Quark Gluon Plasma*. It is believed that quark gluon plasma filled the early universe during 10^{-6}s after the Big Bang. During $10^{-5} - 10^{-4}$s after the Big Bang, as the temperature decreased, the universe then experienced a continuous QCD phase transition and hadrons are formed. We may also create "Little Bang" in relativistic heavy ion collisions by

hadron collider in the laboratory to study QGP. It is also expected to find QGP at high baryon density such as the core of superdense stars such as neutron star and quark star. We will not discuss it here and more details could be found at [16].
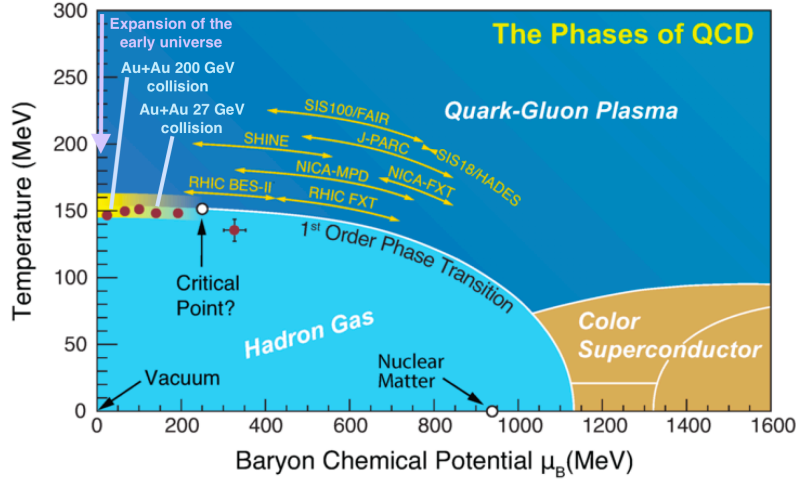
Fig. 1.4 **The schematic of our current understanding of the QCD phase diagram as a function of temperature and baryonic chemical potential μ_B. μ_B represents the excess of quarks over anti-quarks. The yellow shadow indicates the crossover between QGP and hadron gas. The picture is taken from [17].**

Figure 1.4 illustrates our current understanding of the expected feature of the phase diagram of QCD matter in terms of temperature (T) and the baryonic chemical potential (μ_B) [17-18]. Baryonic chemical potential represents the excess of quarks over antiquarks. Around μ_B=0, where the density of quarks and antiquarks are almost equal, the phase transition from QGP to hadron gas is a smooth crossover. As LQCD calculations are more and more accurate now. The predicted temperature of crossover occurs at $\mu_B = 0$ is $T_c = 154 \pm 9$ MeV (critical temperature) [19]. The crossover region is indicated as the yellow shadow in Fig. 1.4. When the μ_B goes higher (about $300 < \mu_B < 1100$ MeV), the continuous cross over between QGP and hadronic matter turns into first order phase transition. It is generally believed that the end of the first order phase transition is a critical point as is pointed in Fig. 1.4. In Au+Au collions at $\sqrt{s_{NN}} = 200$ GeV which is at RHIC top energy, the baryonic chemical potential is very close to zero. At lower collision energies, the initial baryon number of the incident nuclei gradually makes larger contribution to the QCD matter formed in the collisions. So it is possible to increase μ_B and scan the QCD phase diagram by decreasing collision energy. The red data points in Fig. 1.4 are measured by the RHIC Beam Energy Scan (BES) program. The second phase of the BES program with high statistics is undergoing during 2019-2020+ [17, 20], the central goal of BES is to determine whether the critical point does

exist. Other planned or undergoing phase space scan program are also illustrated in Fig. 1.4. At extremely high baryon density but low temperature region, it is predicted that the cold dense quark matter would behave as a color superconductor [21]. Such cold and dense matter is expected to only be found in the core of neutron stars. We expect the measurements of neutron stars via the gravitational waves and X-ray observations could give us a view of properties of cold dense quark matter.
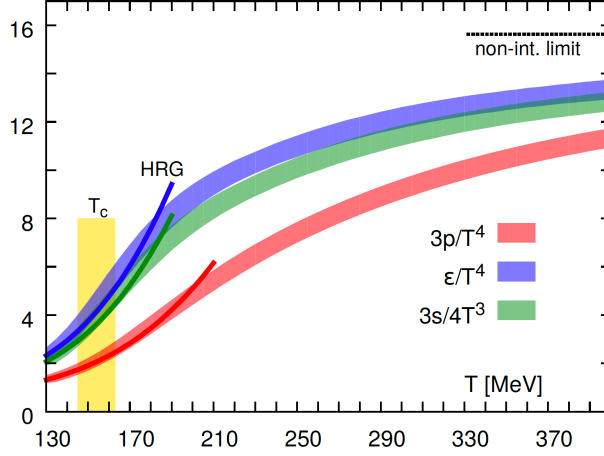
Fig. 1.5   **Pressure p, energy density ϵ, and entropy density s of the hot QCD matter as a function of the temperature from LQCD calculation (bands in the plot). The darker lines refer to the hadron resonance gas (HRG) model prediction. The yellow vertical shadow indicates the cross-over region. The horizontal dash line at $95\pi^2/60$ corresponds to the energy density of the ideal non-interaction gas limit (Stefan-Boltzmann limit). The figure is from [19].**

The QCD equation of state (EOS) from (2+1)-flavor QCD calculation is shown in Fig. 1.5, such as the pressure p, energy density ϵ and entropy density $s = (p + \epsilon)/T$ as a function of temperature T. (2+1)-flavor refers to two light quark (u, d) plus one heavier strange quark s. It is obtained by integrating of the temperature derivative of the QCD partition function ($\ln Z$). The calculation corresponds to the vertical axis of the Fig. 1.4 where net baryon density equals to zero. This plot also indicates that the phase transition is a continuous cross over around $T \sim 150$ MeV at $\mu_B = 0$. The cross over region is indicated as yellow shadow in the plot. At low temperature, Hadron Resonances Gas (HRG) model (darker lines in the plot) is expected to have good description on all thermodynamic quantities, in which all the hadron and hadron resonances are assumed as non-interacting particles. Lattice calculation is consistent with HRG at $T < 155$ GeV. At extremely high temperature $T \to \infty$, as the coupling between quarks and gluons is weak enough to be ignored (due to "asymptotic freedom"), the thermodynamics quantities will eventually reach Stefan-Boltzmann limit, indicated as the upper dash line in

the plot. This also suggests that QGP produced in the heavy ion collisions should be a strong coulping quark gluon liquid instead of weakly interacting gas. The parametrized EOS serves as the input for hydrodynamic models in the heavy ion collisions [18].

1.4   Relativistic heavy ion collisions

Lattice QCD predicts that the quark gluon plasma, which once could be found at anywhere of the early universe, can be created in relativistic heavy ion collisions. Two big questions for the study for QGP in heavy ions collisions are: (1) does this matter really formed in the heavy ion collisions? (2) what are the evolution and properties of this hot medium? In this section, the basic knowledge of heavy ion collisions will be introduced.

1.4.1   Collision geometry

In heavy ion collisions (HIC), the de Broglie wavelength of the nucleons is much smaller with respect to the radius of the nucleus (R), so the impact parameter b could be used to characterize the geometry overlap of the two nuclei. Experimentally, depending on the impact parameter, events are classified into the degree of centrality. When $b = 0$, the collision is regarded as most central collision with centrality 0%. The nucleons in colliding nuclei are classified as participants (marked as dark blue in Fig. 1.6) and spectators (light blue area in Fig. 1.6), according to whether they participant in at least one inelastic collision or not. Impact parameter b cannot be measured directly. In the experiment, event centrality can be defined by the measurable quantities that changes monotonically with b and then taking advantage of models. For example, we measure either number of charged particles N_{ch} by TPC, or spectators (or participants N_{part}) by the detector at zero degree from the beam direction (ZDC). These would be set as the inputs for the Glauber model simulation of nuclear collision geometry. The average number of binary collisions $<N_{coll}>$, and b can be calculated from Glauber model [22].

1.4.2   Space-time evolution of the collision

Figure 1.7 shows the system space-time evolution in a typical heavy ion collisions. Let's start with the time before the collision happens. When two nuclei fly head to head in a velocity close to the speed of light, they look like "pancake" due to Lorentz-contraction along the beam direction in center of mass frame. They pass through each
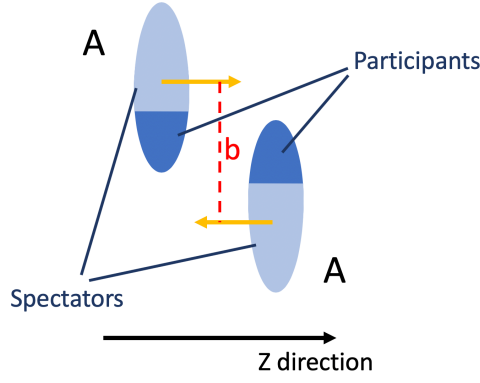
Fig. 1.6   The schematic diagram of impact parameter *b*, participants in overlap zone of the nuclei (marked in dark blue), and spectators (marked in light blue) in nucleus-nucleus collision.

other, deposit a large amount of energy in the overlap zone, and leave behind a highly excited and longitudinally expanding nuclear matter [23].
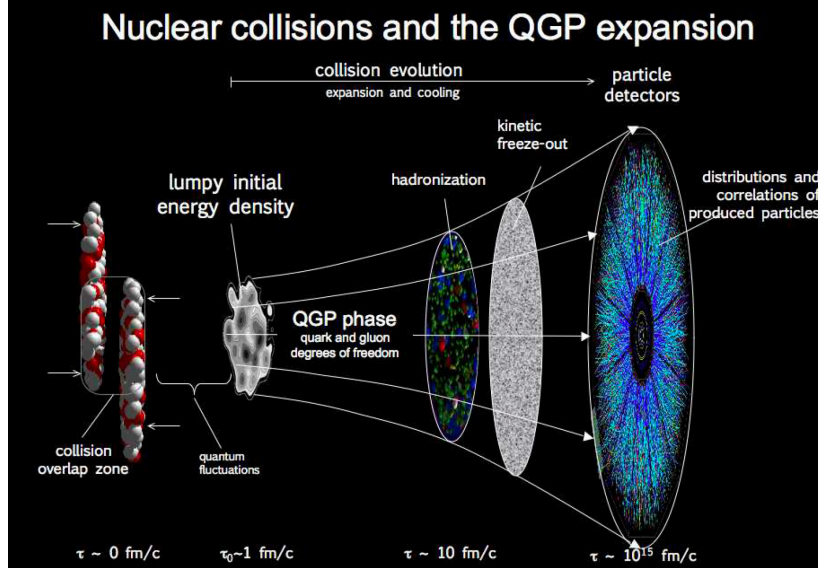
Fig. 1.7   This plot illustrates the space-time evolution of heavy ion collisions. The picture is taken from [24]

During the first $0 < \tau < \tau_0 \sim 1$ fm/c, the system experiences pre-equilibrium stage. The initial collision happens within a very short period $\tau \leqslant 2R/\gamma_{cms}c$ (R is the nucleus radius). The energy density in this stage is very high as a result of Lorentz contraction. Shortly after initial collision, the system reaches approximate local thermal equilibrium in about 1 fm/c. It has aroused interests from theory community for a long time to provide approximate explanation on why such local equilibrium can be established so fast because the coupling is expected to be weak due to "asymptotic freedom". A recent theoretical overview could be found at [25].

When the system is close to local thermal equilibrium, the subsequent evolution can

be described by relativistic hydrodynamics before hadronization happens ($\tau_0 < \tau < \tau_{had}$). The observation of large elliptic flow from the experiment strongly supports the idea that QGP created in heavy ion collisions is a droplet instead of gas. We will further discuss experiment findings in next section. If the local equilibrium has achieved perfectly and QGP is an ideal liquid with infinite coupling (*ideal hydrodynamics*, mean free path λ_{mfp} equals to zero), the system can be described by relativistic Euler equations $T^{\mu\nu}_{ideal} = e u^\mu u^\nu + \mathcal{P} \Delta^{\mu\nu}$ and obeys energy-momentum conservation $\partial_\mu T^{\mu\nu}$. Where e is the energy density, $\mathcal{P}$ is the pressure, and u^μ is the four velocity. For more realistic case, considering near-equilibrium correction and finite coupling (*viscous hydrodynamic model*), the stress tensor is corrected with viscosity part:

$$T^{\mu\nu} = T^{\mu\nu}_{ideal} + \pi^{\mu\nu} + \Pi \Delta^{\mu\nu} \tag{1.7}$$

where Π refers to bulk stress and $\pi^{\mu\nu}$ is shear tensor [26]. The first order expansion of Shear tensor $\pi^{\mu\nu}$ in Eq. 1.7 is given as $\pi^{\mu\nu} = -\eta \sigma^{\mu\nu}$. The unitless quantity specific viscosity η/s is defined, where s is the energy entropy. Figure 1.8 is the selected hydrodynamic model calculations under different viscosity value, the initial condition of which is from color-glass-condensate model (CGC) [27]. The estimated specific viscosity is $\eta/s = 0.08 - 0.16$ in Au+Au collisions at $\sqrt{s_{NN}} = 200$ GeV [28-30]. The small viscosity also indicates that our observed final-state particle properties, such as multiplicity and collective motion, still carry sufficient information of initial stage conditions.

When the system is below critical temperature T_c, quarks and gluons convert to hadrons. As the energy density and temperature decrease, the inelastic scattering rate between different hadron species gradually become too slow to maintain chemical equilibrium. As a result, the yield of final stable hadrons in the system will not change any more, called "chemical freeze-out". The hadrons will still change their momenta through elastics scattering after chemical freeze-out, until the system decreases to "Kinematic freeze-out" temperature. Kinematic freeze-out refers to that the momentum distribution of hadrons will not change any more. After that, the system can be regarded as non-interaction gas. In the hadronic phase, the collective expansion is so fast that the system is hard to maintain local thermal equilibrium. For precise description, the macroscopic hydrodynamic model should be replaced by a microscopic solution of the coupled Boltzmann equations for various hadron species, namely "hadron cascade" [33-35]. For many observables, viscous hydrodynamic model still have a good description in hadron phase until the defined freeze-out temperature T_{fo}.
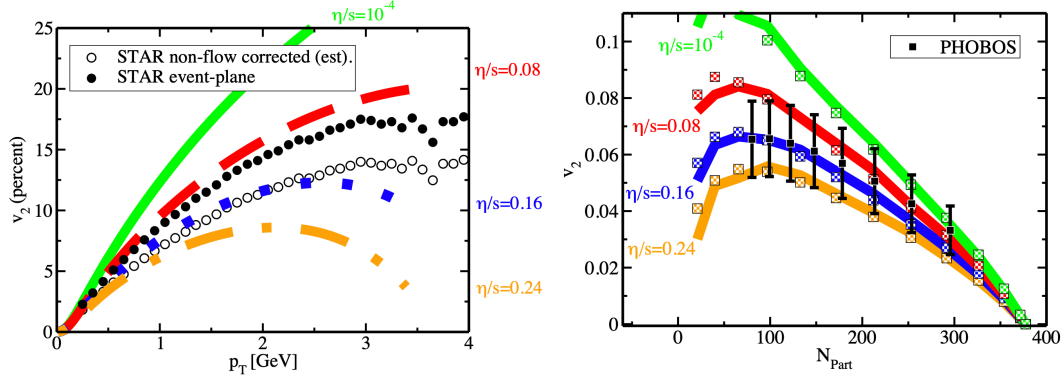
Fig. 1.8 **Elliptic flow v_2 for charge particle measurements in Au+Au collisions at $\sqrt{s_{NN}} = 200$ GeV and its comparison to hydrodynamic model with different specific viscosity η/s. Right plot shows the charge hadron v_2 as a function of p_T in minimum bias events from STAR [31]. Left plot is the integrated p_T v_2 as a function of $<N_{part}>$ from PHOBOS [32]. The initial energy density distribution for the model curves in the plots is from color-glass-condensate (CGC) models. The estimated specific viscosity of QGP at RHIC energy is 0.08-0.16. The picture is taken from [29].**

1.4.3   Experimental observable

1. Flow

Before the experiments at RHIC started, people didn't know if the QGP created at RHIC would be a weakly-coupled quark-gluon cloud because of "asymptotic freedom" of QCD, or a strong interaction system as QCD is still strongly-coupled around critical temperature. In gas picture, the azimuthal distribution of the final state particles is expected to be isotropic, because the momentum direction of a gas particle should be random. On the other hand, if a strongly-coupled liquid is formed from deconfined quarks and gluons, the system will expand faster in the direction with larger gradient pressure. As a result, the initial anisotropic distribution of the energy converts into momentum anisotropy. In the experiment, the anisotropic particle distribution in momentum space can be described as the Fourier decomposition with respect to the reaction plane:

$$E\frac{d^3N}{d^3p} = \frac{d^2N}{2\pi p_T dp_T dy}(1 + \sum_{n=1}^{\infty} 2v_n cos[n(\phi - \Phi)])$$

$$v_n = \langle cos[n(\phi - \Phi)]\rangle, \ n = 1, 2, 3, ... \tag{1.8}$$

Where Φ is the reaction plane angle. The second coefficient v_2 is called elliptic flow.

Fig. 1.10 shows the first measurement of v_2 versus centrality at RHIC from STAR [36]. The centrality is expressed by average charged particle multiplicity in each bin over sthe highest multiplicity observed n_{ch}/n_{max}. The highest n_{ch}/n_{max} refers to the most central collision. Just as hydrodynamic model predicted, elliptic flow is higher in more
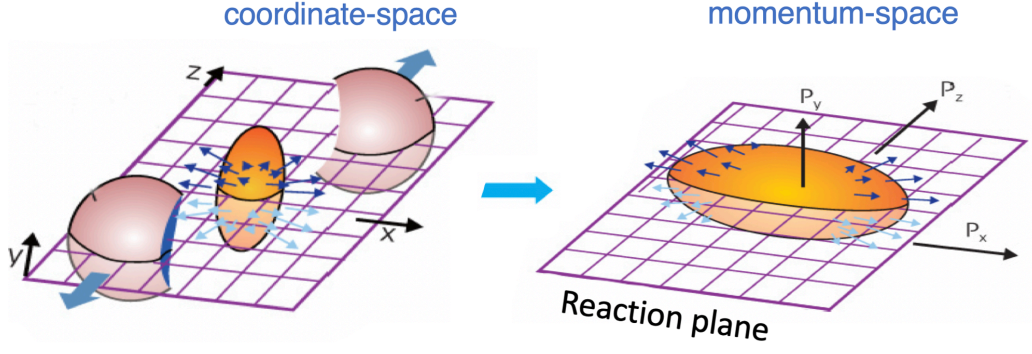
Fig. 1.9 **The initial asymmetric energy density distribution in spatial space results in the asymmetric particle emission in momentum space.**
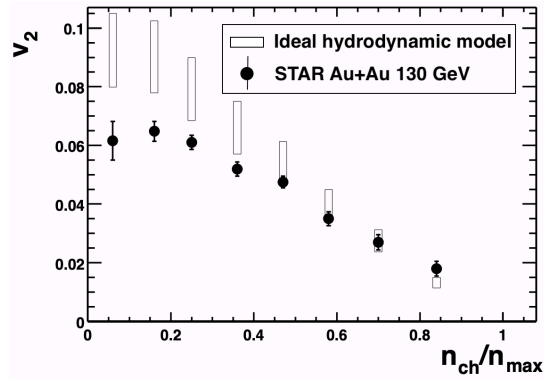
Fig. 1.10 **The first measurement of v_2 versus centrality at RHIC from STAR [36]. n_{ch}/n_{max} is the ratio of average charged particle multiplicity in each bin over the highest multiplicity observed. The higher n_{ch}/n_{max} refers to more central collisions. Open rectangles are hydrodynamic predictions assuming zero mean free path.**

peripheral collisions, where the initial eccentricity of the system is larger. The flow behavior observed at RHIC strongly supports the idea that a strong coupling liqiud-like QGP is produced at RHIC [37].

Figure 1.11 shows v_2 of various hadron species and inclusive charged hadrons as a function of p_T and the comparison with hydrodynamic models in Au+Au collisions at 200 GeV [24, 38-42]. At low p_T ($p_T = 1 \sim 2$ GeV/c), the elliptic flow shows apparent mass ordering with heavier particle having smaller v_2. While at higher p_T, mass ordering is broken and baryon tend to have larger v_2. The mass ordering phenomenon can be understood by hydrodynamic picture of the particle emisson from the fast expansion fireball. To develop sufficient collective flow as the data presents, hydrodynamic model reqiures that the pre-equilibrium is established within very short period of time $\sim 0.2-1$ fm.

Another interesting phenomenon for elliptic flow measurement is NCQ scaling of v_2. NCQ is short for number of constituent quark n_q. For meson $n_q = 2$ and for baryon

$n_q = 3$. We can scale v_2 of various particle species with n_q and plot v_2/n_q as a function of $(m_T - m_0)/n_q$, as shown in Fig. 1.12. The data is from minimum bias events in Au+Au collisions at $\sqrt{s_{NN}} = 62.4$ GeV. At $(m_T - m_0)/n_q < 1$, all of the particles' v_2/n_q fall into a same curve. In heavy ion collisions, hardon at moderate p_T is formed by the competition of traditional fragmentation and quark coalescence. The quark coalescence model assumes that quarks and antiquarks are the effective degrees of freedom in the parton phase and they combine to form hadrons [43]. NCQ scaling phenomenon of hadron v_2 is expected from coalescence model if the constituent quark of hadrons have obtained elliptic flow before hadronization [44-45].
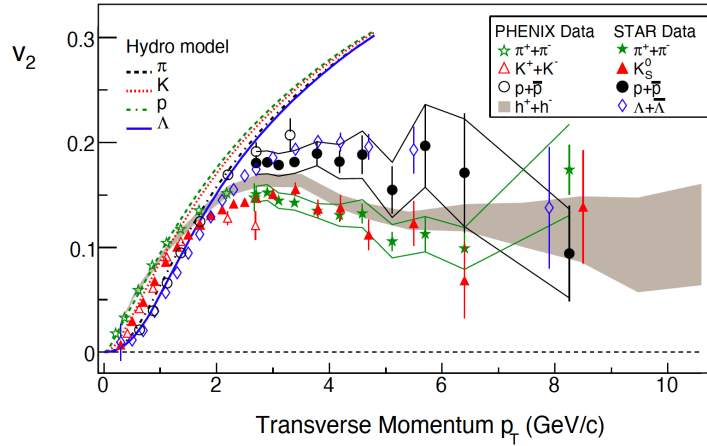
Fig. 1.11 v_2 **of various hadron species and inclusive charged hadrons as a function of p_T and comparison with hydrodynamic models [24, 38-42]. The data are from STAR and PHENIX measurements in Au+Au collisions at $\sqrt{s_{NN}} = 200$ GeV in mid rapidity. The figure is taken from [24].**
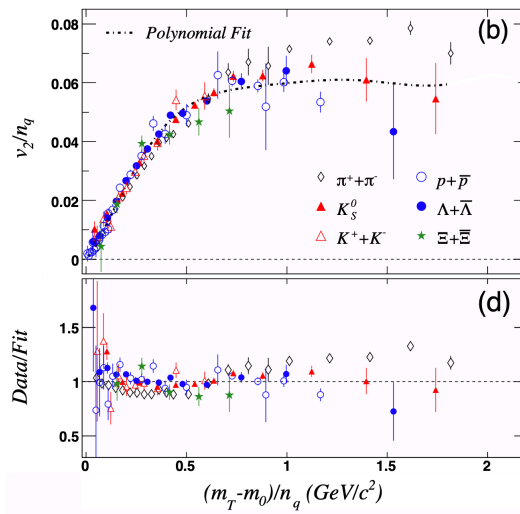
Fig. 1.12   **Number of constituent quark number scaled v_2 for different hadron species in minimum bias events at Au+Au collisions at $\sqrt{s_{NN}} = 62.4$ GeV [42].**

14

2. Nuclear modification factor

When the partons, that are produced in the initial hard scattering processes of heavy ion collisions, traverse the QGP medium, they lose energy via both elastic scattering with particles in the medium (known as "collisional energy loss") or gluon radiation induced by the medium (known as "radiative energy loss"). The final state hadron spectra will be modified due to energy loss of partons. To quantify the modification of hadron spectra with respect to p+p collisions, nuclear modification factor is defined as:

$$R_{AB}(p_T) = \frac{dN_{AB}^h/dp_T}{\langle N_{bin}\rangle \, dN_{pp}^h/dp_T} \tag{1.9}$$

Where AB represents collision system, such as d+Au collision, Au+Au collision. $\langle N_{bin}\rangle$ (also written as $\langle N_{coll}\rangle$) is the average number of binary collisions which can be calculated by Glauber model [46], and h refers to our interested particles, such as identified particle, inclusive charged hadron, etc.

Fig. 1.13 shows charged hadron R_{AB} in Au+Au (R_{AA}) and d+Au (R_{dA}) collisions at $\sqrt{s_{\mathrm{NN}}} = 200\,\mathrm{GeV}$ as function as p_T. Measurements of R_{AB} in small systems, such as d+Au and p+Au, are important for the study of cold nuclear matter effects. The hadron production in intermediate p_T ($2<p_T<6$ GeV/c in Fig. 1.13) is enhanced in d+Au collisions due to initial multiple elastic scattering, known as Cronin effect [47-48]. While in A+A collisions, a large suppression of R_{AA}^h is observed at $2.5 < p_T < 10$ GeV/c, suggesting the production of the hot medium. Fig. 1.14 shows the evolution of charged particle (hadron) and pion R_{AA} in various collision energies and systems (SPS [49-50], RHIC [51-52], LHC [52-55]). Generally, the charged particle R_{AA} distributions are suppressed (<1) over most of the p_T range, reaching local maxima at $p_T \sim 2$ GeV/c and local minima at $p_T \sim 7-10$ GeV/c. Apart from Cronin effect and parton energy loss, the final measured charged particle R_{AA} is also affected by nuclear parton distribution function, radial flow. At high p_T ($p_T > 10$ GeV/c), the suppression mainly results from the energy loss in the medium, known as "jet quenching".

1.5   Motivation of open heavy flavor measurements

Experimental evidences have confirmed the formation of QGP in relativistic heavy ion collisions at RHIC and LHC over the last two decades. This strong coupling hot QCD matter provides us a unique laboratory environment to study the strong interactions. Due to their large masses, heavy quarks (c, b) are regarded as an excellent probe to early dynamics of the system.
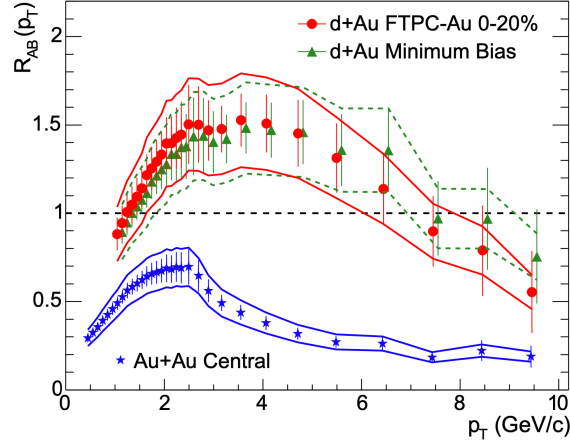
Fig. 1.13   Charged particle nuclear modification factor measurements in d+Au and AuAu collisions at 200 GeV from STAR [56-57]. The figure is taken from [56].
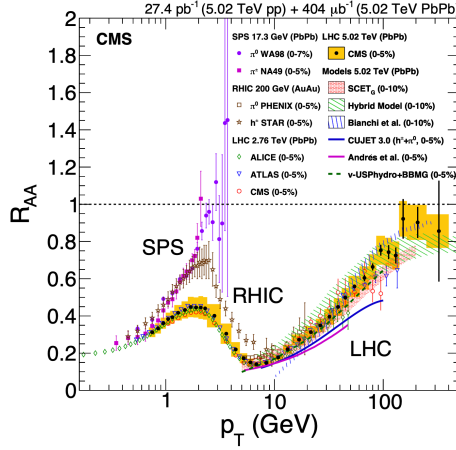
Fig. 1.14   The measurements of charged particle (hadron) and pion nuclear modification factor R_{AA} in Pb+Pb and Au+Au collisions at different energies (SPS [49-50], RHIC [51-52], LHC [52-55]). The figure is taken from [55].

As $m_{c,b} \gg \Lambda_{QCD}$, their production cross section are calculable by pQCD with "factorization theorem". Because their mass are much larger than typical QGP temperature $m_{c,b} \gg T_{QGP}$, the thermal production of the heavy quarks are suppressed [58-59]. So firstly they are predominately produced in the initial hard scattering process with a formation time $\sim 1/2m_Q \sim 0.1$ fm/c, before the formation of QGP. Secondly, the number of heavy quarks is expected to be conserved throughout the evolution of the system. Moreover, the thermal relaxation time of heavy quarks is expected to be larger than light quarks by a factor $\sim m_Q/T \simeq 5-20$ (m_Q refers to the mass of heavy quark). The estimated charm quark thermalization time is on the same order as QGP life time τ_{QGP} at RHIC [60]. For one thing, different from light quarks (thermalized during pre-equilibrium), whose evolution can be described within the hydrodynamic framework, heavy quark thermalization and evolution process are described as a transport approach.

For another thing, the spectrum modification of heavy flavor (HF) hadrons should still carry information of their interaction history with the hot medium.

In the rest of this section, we will discuss the heavy quarks transport, energy loss in the QGP and hadronization in the heavy ion collisions.

1.5.1   Collectivity - Heavy flavor electron v_2

Heavy quarks are able to obtain collective flow by their interaction with bulk particles in the medium. At low momentum, their interaction with the bulk particle is dominated by frequent elastic scattering with relatively small momentum transfer $Q^2 \sim T^2$ compared to the typical thermal momentum of a heavy quarks $p_{th}^2 \simeq 3m_Q T$ (Nonrelativistic). Thus, heavy quark propagation in the QGP can make an analogy to "Brownian motion" in light particle liquid [61]. Their diffusion in the medium can be described by classical Langevin equation as [62]:

$$\frac{d\vec{p}}{dt} = -\eta_D(p)\vec{p} + \vec{\xi}(t) \tag{1.10}$$

Where η_D is the drag coefficient and ξ denotes the random force. In some models, a third item $\vec{f} = -d\vec{p}_g/dt$ is added in the right of Eq. 1.10, describing the recoil force exerted on heavy quarks due to gluon radiation and $\vec{p}_g$ denotes the momentum of radiated gluons [63].
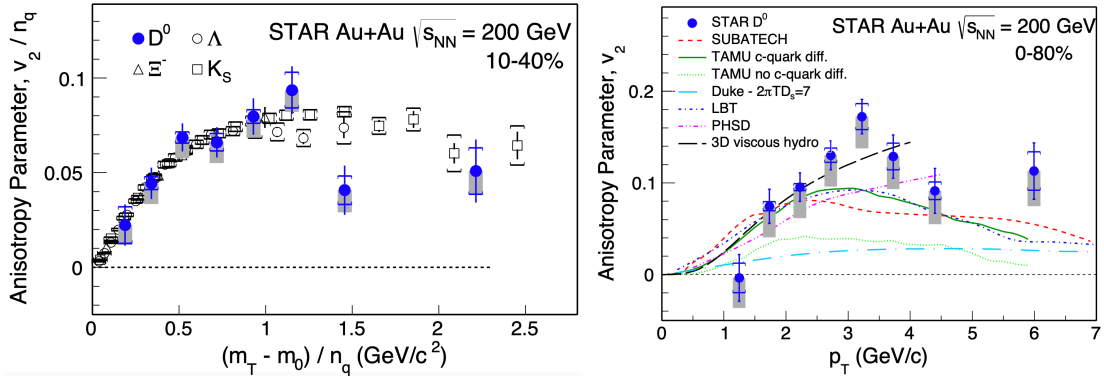
Fig. 1.15   **The measurement of D^0 v_2 in Au+Au collisions at $\sqrt{s_{NN}} = 200$ GeV. The left plot is NCQ scaled v_2 as a function of $(m_T - m_0)/n_q$. The right plot is D^0 v_2 versus p_T compared to model calculations.**

The spatial diffusion coefficient describes the broadening of the spatial distribution with time which is defined via: $\langle x^2 \rangle - \langle x \rangle^2 = 2d\mathcal{D}_s t$, where $x(t)$ is the particle's position and d denotes the dimensions. It characterizes the heavy quark transport property in the QGP. The solution of $\mathcal{D}_s$ is given as [62]:

$$\mathcal{D}_s = \lim_{p_Q \to 0} \frac{T}{m_Q \eta_D} \tag{1.11}$$

17

The dimensionless scaled HF diffusion coefficient $2\pi T\mathcal{D}_s$ is believed as carrying universal information of QGP, similar as shear viscosity η/s and electric conductivity [60, 64]. The basic physics observables that are beneficial to the constraint of $2\pi T\mathcal{D}_s$ are nuclear modification factor R_{AA} and elliptic flow v_2 of charm and bottom hadrons or their decay daughters.

Fig. 1.15 shows the v_2 of D^0 meson and various light flavor hadrons scaled by NCQ scaling as function as $(m_T - m_0)/n_q$ in Au+Au collisions at $\sqrt{s_{\mathrm{NN}}} = 200$ GeV [65]. The D^0 obtain a large v_2 that follows the general trend as those of strange hadrons. The result suggests that charm quark may be close to thermal equilibrium in Au+Au collisions at $\sqrt{s_{\mathrm{NN}}} = 200$ GeV. Fig. 1.18 shows D^0 R_{AA} measurements from RHIC. A local maximum is observed in D^0 R_{AA} distribution at low $p_T \sim 2$ GeV/c due to the collective motion of the charm quark, known as "flow bump".
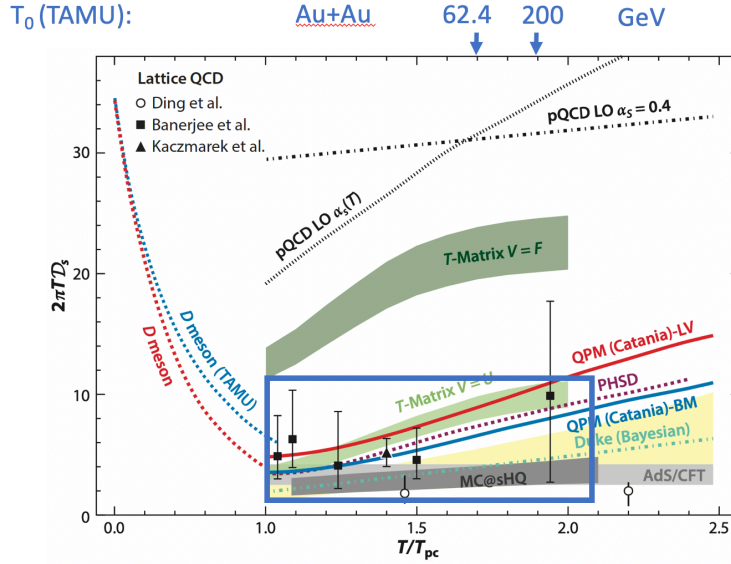
Fig. 1.16   Charm quark spatial diffusion coefficient $2\pi T\mathcal{D}_s$ as a function of reduced temperature T/T_{pc} from lattice QCD calculation [66-68], pQCD calculation [62, 69], Ads/CFT calculation [70], QPM calculation [71], Duke model [72], T-matrix approach [73]. The initial temperature T_0 used in TAMU model [74] in Au+Au collisions at 62.4 and 200 GeV are indicated with blue arrows. Only the theory calculations within the blue box can describe D^0 R_{AA} and v_2 data in Au+Au collisions at $\sqrt{s_{\mathrm{NN}}} = 200$ GeV. The picture is taken from [64].

A summary of the spatial diffusion coefficient $2\pi T\mathcal{D}_s$ as a function of temperature from theoretical calculations is shown in Fig. 1.16 [64]. The blue box on Fig. 1.16 points out the theoretical calculations that can simultaneously describe D^0 R_{AA} and v_2 data in Au+Au 200 GeV collisions. Current theoretical calculations of $2\pi T\mathcal{D}_s$ still have a large uncertainty as we can see from Fig. 1.16. As the initial temperature decreases

with decreasing collision energy, heavy flavor measurements at low energies are beneficial to constrain the temperature dependence of charm quark $2\pi T \mathcal{D}_s$.
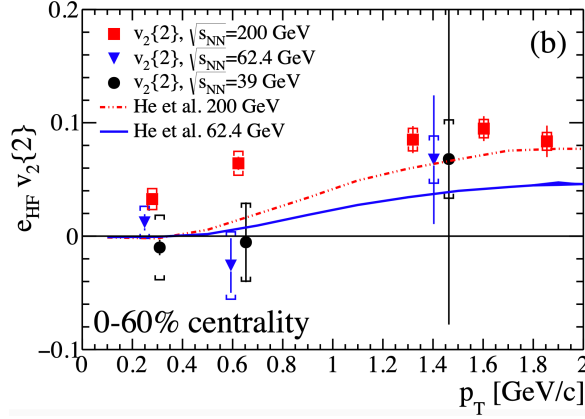
Fig. 1.17   Measurements of heavy flavor electron in Au+Au collisions at 39, 62.4 and 200 GeV from STAR [75].

Previously, STAR has measured the elliptic flow of heavy flavor electrons in Au+Au collisions at 39 and 62.4 GeV, as shown in Fig. 3.36 [75]. However, due to the limited statistics, the uncertainties are too large to get solid conclusion. During RHIC year 2017 and 2018 run, STAR collected large data samples in Au+Au collisions at $\sqrt{s_{\mathrm{NN}}}$ =27 and 54.4 GeV, the statistics of which is ten more times compared to that of 62.4 GeV data taken in 2010. So it is expected that the precision of measurements on heavy flavor electrons v_2 will be improved now. The analysis details will be discussed in Chapter 3.

1.5.2   Energy loss - D^{*+} production

As we have introduced in section 1.4.3, partons lose energy in the hot medium through elastic scattering or gluon radiation. It is expected that radiative energy loss is the dominant source accounting for the energy loss of high p_T partons if making analogy to electromagnetic interaction. The gluon emission of a heavy quark is expected to be suppressed at angles smaller than $\Theta \leqslant m_Q/E$, where m_Q is the mass of the quark, E is the quark's energy, and Θ approximately equals to the ratio of gluon's transverse momentum over its energy [76-77]. This is known as "dead cone" effect. For gluons, as they carry more color charges than quarks, they are more likely to emit gluons. It can be inferred from above discussion that there would be an energy loss hierarchy for gluons and various quarks species: $\Delta E_b < \Delta E_c < \Delta E_{u,d,s} < \Delta E_g$. Thus it was predicted that R_{AA} of HF hadrons or their decay daughters is expected to be less suppressed than light flavor mesons [78]. However, measurements at RHIC show that the suppression level of charm hadrons (or decay daughters) is comparable to that of light flavor hadrons up to

$p_T < 10$ GeV/c (Heavy flavor electron: [79-81], D^0: [82-83]). The experiment results indicate that collisional energy loss also make non-negligible contribution. The final measured R_{AA} is also affected by the initial parton spectra and hadronization process.
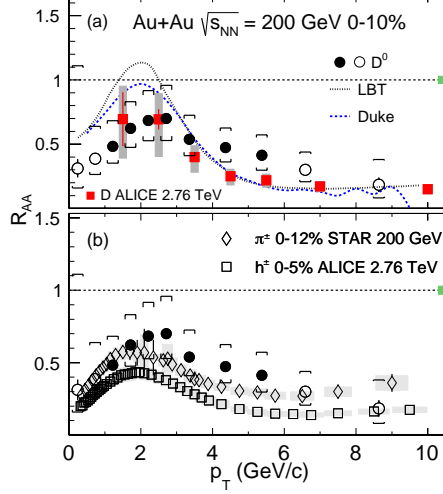
Fig. 1.18   The upper panel is the measurement of D^0 R_{AA} in Au+Au collisions at $\sqrt{s_{NN}} = 200$ GeV [84] and average D meson in Pb+Pb collisions at $\sqrt{s_{NN}} = 2.76$ TeV [85]. D^0 R_{AA} is compared with pions [86] and charged hadrons [87], shown in the bottom panel. The figure is taken from [84].

Open heavy flavor measurements is beneficial to understanding the role of collisional and radiative energy loss. Fig. 1.18 shows current D^0 R_{AA} measurement from STAR. But to get a complete story of charm quark, measurements of other charm hadrons are required, as the constituent quarks of D^0 is $c\bar{u}$ and the R_{AA} structure might be contributed by $\bar{u}$ too. D^{*+} is an indispensable piece for this study, as nearly 24% of charm quarks will hadronized to D^{*+}: $c \to D^0$ (0.614), $c \to D^{*+}$ (0.239). The analysis of D^* production will be discussed in Chapter 4.

1.5.3   Hadronization - simulation of Λ_c^+ production

At large momentum transfer with a perturbative scale, hadronization can be described as fragmentation process. A color-singlet parton i with momentum p_i is hadronized into hadron h with momentum $p_h = z p_i$ $(0 < z < 1)$, and the fragmentation function $D_{i \to h}(z)$ refers to the probability of finding hadron h in parton i. It can be measured in $e^+ e^-$ or ep collisions. However fragmentation picture is challenging in describing the formation of lower p_T hadrons as it becomes non-perturbative. Quark coalescence can be an important mechanism for quarks production at low p_T, especially in heavy ion collisions. In this picture, a naive description is deconfined quarks

and anti-quarks are recombined into bound state hadrons. Based on quark coalescence framework, the magnitude of charm quark elliptic flow can be unfolded from the elliptic flow of charm hadrons, which provides information of charm quark thermalization level. A good understanding of heavy quark hadronization process are important for precise extraction of heavy quark diffusion coefficient from R_{AA} and v_2.

Heavy quarks are dominantly produced in initial hard scattering process, the total number of which is nearly conserved. Thus they serve as a good tool to study the hadronization mechanism in heavy ion collisions. Hadronization is generally studied by taking the ratio of different hadron species. Coalescence models have predicted the enhancement of D_s^+/D^0 ratio in A+A collisions with respect to p+p collisions due to the enhanced strangeness production in A+A collsions [88-89]. A baryon to meson enhancement in heavy ion collisions is also expected by coalescence models. Fig. 1.19 shows Λ_c^+/D^0 and D_s^+/D^0 measurements from STAR and LHC. Although different coalescence models all predict the enhanced Λ_c^+/D^0 ratio, they have a large discrepancy at $p_T < 3$ GeV/c. The enhancement of Λ_c^+/D^0 and D_s^+/D^0 ratio also indicate that Λ_c^+ and D_s^+ make large contribution to total charm cross section at low p_T. More precise measurements over a broad momentum range are desired in the future sPHENIX program [90].
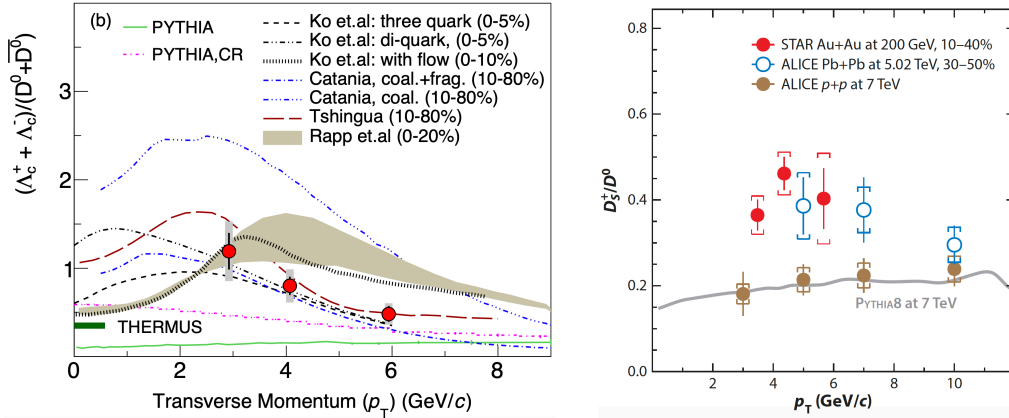
Fig. 1.19   **Left: Measurements of Λ_c^+/D^0 ratio as function as p_T in Au+Au collisions at RHIC. Right: Measurements of Λ_c^+/D^0 ratio as function as p_T in Au+Au, Pb+Pb and p+p collisions.The enhancement of Λ_c^+/D^0 and D_s^+/D^0 are observed in A+A collisions with respect to PYTHIA calculations in p+p.**

Chapter 2   Experimental set up

2.1   The Relativistic Heavy Ion Collider

The Relativistic Heavy Ion Collider (RHIC) is one of the two operating heavy ion colliders in the world, located at Brookhaven National Laboratory in New York. RHIC started its first physics run at 2000, which was the first and highest-energy heavy ion collider at that time. The beam energy of RHIC could reach 100 GeV/nucleon for Au ion and 250 GeV for proton. One of the primary goal of RHIC is to study the formation and properties of QGP. RHIC is also the only polarized proton collider in the world, which enables the study of spin physics at RHIC energy. The STAR detector is the only detector that is currently operating at RHIC. Apart from STAR, another 3 detectors had ever operated at RHIC for heavy ion physics since 2000, including PHENIX (2000~2016), PHOBOS (2000~2005), and BRAHMS (2000~2006). A new state-of-art detector sPHENIX is under construction and will be located at the old PHENIX hall, which is expected to start taking data in 2023. The proposed major upgrade for RHIC is eRHIC [91], the design of which has been selected by US DOE for the future Electron-Ion Collider (EIC) [92] in the United States in 2030s.
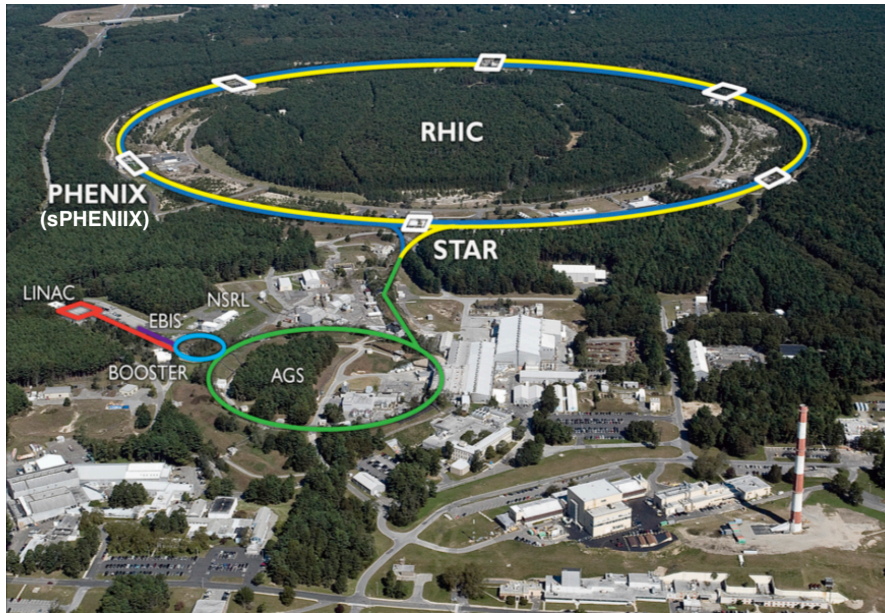
Fig. 2.1   The Relativistic Heavy Ion Collider at Brookhaven National Laboratory. The ion beams start at EBIS, then they are delivered to Booster, and followed by AGS. They will reach a energy of 10.8 GeV/u and travel at a speed of 99.7% light-speed before being injected into the RHIC. The STAR detector is located near the AGS-to-RHIC Transfer Line.

Fig. 2.1 shows the schematic view of the RHIC. For Au+Au collisions, the Au^{32+} ions are created from Au atom by Electron Beam Ion Source (EBIS) with an output energy 17 keV/u. Then the ion beams are accelerated by two small linear accelerators. The Au ion beams are required to reach 2 MeV/u before being delivered to the Booster Synchrotron (Booster), which is a small circular accelerator. Au^{32+} are accelerated to 95 MeV/u in the Booster, traveling at about 37% the speed of light. They are stripped again at the exit of the Booster and turn into Au^{77+}. Then they enter the Alternating Gradient Synchrotron (AGS) and are further accelerated to the RHIC injection energy of 10.9 GeV/u. The Au ions are fully stripped to become Au^{79+} at the exit of AGS. Then they are transferred to RHIC through AGS-to-RHIC beam transfer line [93-94]. For polarized protons, they are first accelerated to 200 MeV in the Linac, then transferred to the Booster, and followed by AGS and RHIC.

2.2   The STAR detector
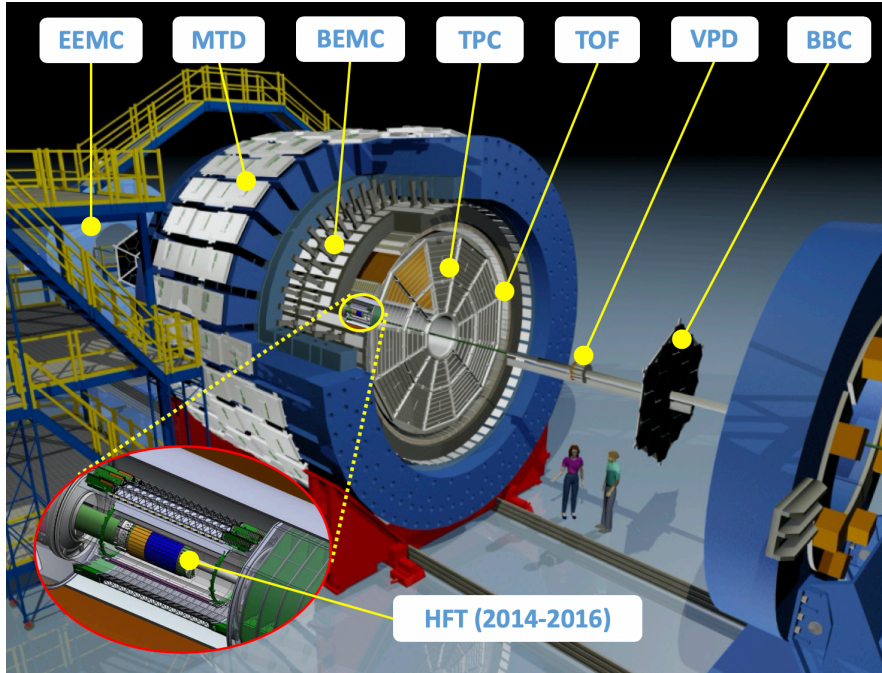
Fig. 2.2   The schematic view of the sub-detector systems of STAR.

The Solenoidal Tracker at RHIC detector (STAR) was designed for the measurements of high multiplicity environment in heavy ion collisions [95]. It is a cylindrical detector covering middle pseudo-rapidity range ($|\eta| < 1$) with a full azimuthal coverage. Fig. 2.2 shows the schematic view of the sub-detector systems of STAR.

The main tracking device is a 4-meters-long Time Projection Chamber (TPC), which

will also provide particle identification (PID) through the ionization energy loss of the particle in TPC gas. Inside the TPC there is Heavy Flavor Tracker (HFT), which operated during 2014-2016. HFT has provided excellent pointing resolution for charged particles, largely improves the significance of charm hadrons measurements. Another important sub-detector for PID is Time of Fight (TOF). Particles are identified by the information of reversed velocity ($1/\beta$) provided by TOF. Outside the TOF detector is the Barrel Electromagnetic Calorimeter (BEMC) [96]. The particles's energy deposited in BEMC and the shape of the shower are beneficial to the separation of high p_T electrons and hadrons. The STAR magnet system, resting outside of BEMC, provides a nearly uniform field parallel to the beam direction with an operating range from 0.25 T to 0.5 T (B $\sim$ 0.5 T in this thesis) [97]. The outermost of the detector system is Muon Telescope Detector (MTD) [98], which was installed in 2014 for muon triggering and identification. It was designed for the measurements of quarkonia via dimuon channel, such as J/ψ and Υ. Along the beam line, there are three fast detectors: the Vertex Position Detector (VPD), the Beam-Beam Counter (BBC) and the Zero Degree Calorimeter (ZDC). All of them are located both in west and east side of the STAR detector. They are used for the minimum bias trigger, event selection and luminosity monitor. The VPD detectors also provide the event "start time" for TOF and MTD detector as well as the primary vertex position along the Z-direction.

TPC, TOF and HFT have played an indispensable role for the analysis discussed in Chapter 3 and 4. We will introduce them in detail in the following sections.

2.3   Time Projection Chamber

Time Projection Chamber (TPC) is the primary tracking detector of STAR covering full azimuthal angle within a pseudo-rapidity acceptance of $|\eta| < 1.8$. [99]. It can record the tracks of charged particle and measure their momenta over a range from $\sim$ 100 MeV/c to 30 GeV/c. Fig. 2.5 shows the first event in Au+Au $\sqrt{s_{\mathrm{NN}}} = 200$ collisions recorded by STAR TPC. The schematics of the STAR TPC structure is shown in Fig. 2.3. The TPC is 4.2 m in length and 4 m in diameter, which is filled with gas and has an inner electric field of about 135 V/cm. The typical drift velocity of ionization electrons in STAR TPC is about 5.45 cm/μs. The ionization electrons drift toward the nearest endcap and the signals are collected by Multi-Wire Proportional Chambers (MWPC) with readout pads [99]. The TPC readout is divided into 12 sectors at each endcap (totally 24 sectors). Fig. 2.4 shows one of the readout sector. Each sector is split into

inner and outer subsectors. The outer subsectors are fully covered by wide pad rows without space between them. More ionization electrons can be collected with full pad coverage so that the resolution of dE/dx measurements can be improved. The pads of inner subsectors are smaller, which are designed for good hit resolution and suitable for high track density region. They are arranged in separate rows with large space between the rows. A Inner Sector TPC (iTPC) upgrade had been proposed in 2015 and full installation has been finished before RHIC Run 2019 [100]. Two iTPC sectors were installed during RHIC Run 2018, but the hits on these two sectors were excluded in the tracking. Details of iTPC project could be found at [101].
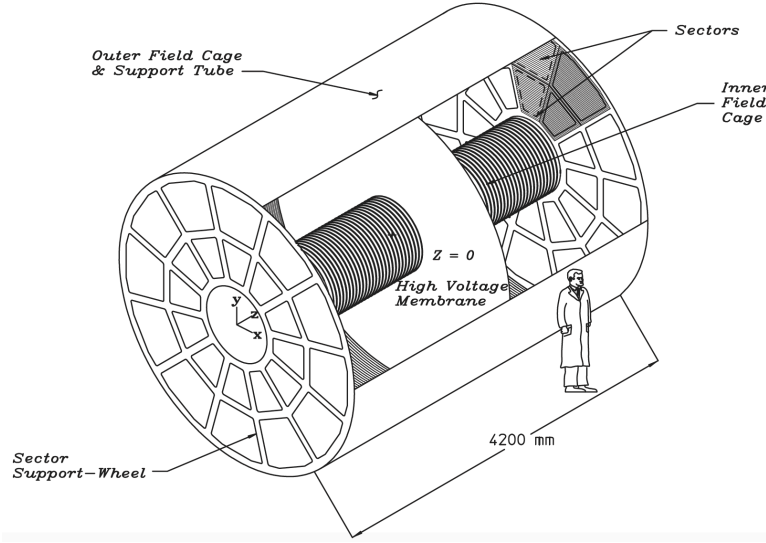
Fig. 2.3   The schematics of the STAR TPC structure. The picture is taken from [99].
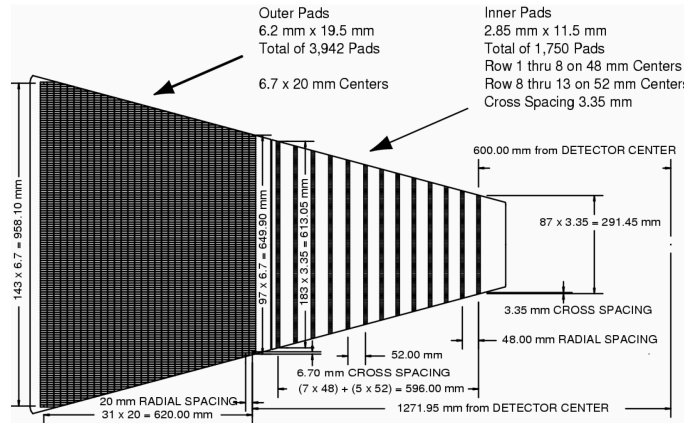
Fig. 2.4   The schematic diagram of anode pad plane with one full sector. Taken from [99].

The energy loss of charge particles in the medium can be described by Bethe-Bloch equation [10]:

$$-\frac{dE}{dx} = Kz^2 \frac{Z}{A} \frac{1}{\beta^2} \left[\frac{1}{2} \ln \frac{2m_e c^2 \beta^2 \gamma^2 T_{max}}{I^2} - \beta^2 - \frac{\delta}{2} \right] \tag{2.1}$$

26

It can be inferred from Eq. 2.1, at a certain momentum ($p = m_0\beta\gamma$), charged particles with different masses may have different energy loss (dE/dx) in the TPC gas. In STAR, the theoretical value for the energy loss of charged particles are calculated by the Bichsel functions [102-103]. The dE/dx resolution measured by the TPC is about 8% for a track crossing 40 pad-rows. Fig. 2.6 shows the energy loss as a function for charged particles in Au+Au collisions at 200 GeV in Run14. The TPC can seperate K/p up to $p \sim 1$ GeV/c and π/K up to $p \sim 0.7$ GeV/c at $B = 0.5$ T.
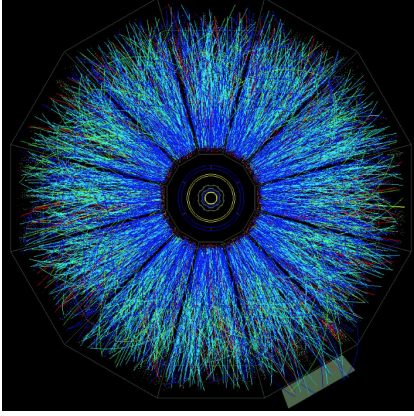
Fig. 2.5   The first Au+Au event at $\sqrt{s_{NN}} =$ 200 GeV recorded by STAR TPC [104].
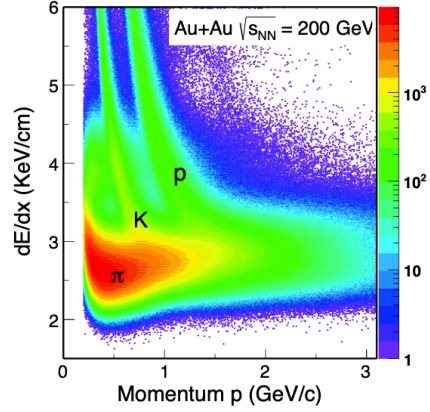
Fig. 2.6   TPC dE/dx versus momentum in Au+Au 200 GeV collisions. Taken from [83].

2.4   Time Of Flight detector

The main goal of time of flight (TOF) system at STAR is to extend particle identification capability to moderate momentum range at mid-rapidity. The TOF detector is based on the technology of Multigap Resistive Plate Chambers (MRPC). Its installation completed in year 2010. The TOF is composed of 120 trays, covering $|\eta| < 0.9$ in pseudo-rapidity and 2π in azimuthal direction. Each tray consists of 32 MRPC models with 6 readout on each module. Fig. 2.7 shows the structure of a single MRPC module.

The whole TOF system consists of two subsystems, VPD for the "start" time (t_1) and the barrel TOF for the "stop" time (t_2). Combining with path length information provided by TPC, the inverse velocity of charged particles can then be calculated as:

$$\frac{1}{\beta} = c\frac{\Delta t}{L} = \frac{\sqrt{p^2 + m^2c^2}}{p} \tag{2.2}$$

where $\Delta t = t_2 - t_1$. The timing resolution of the TOF system is better than 100 ps in heavy-ion collisions. With such resolution, π/K separation is extended to $p \sim 1.6$
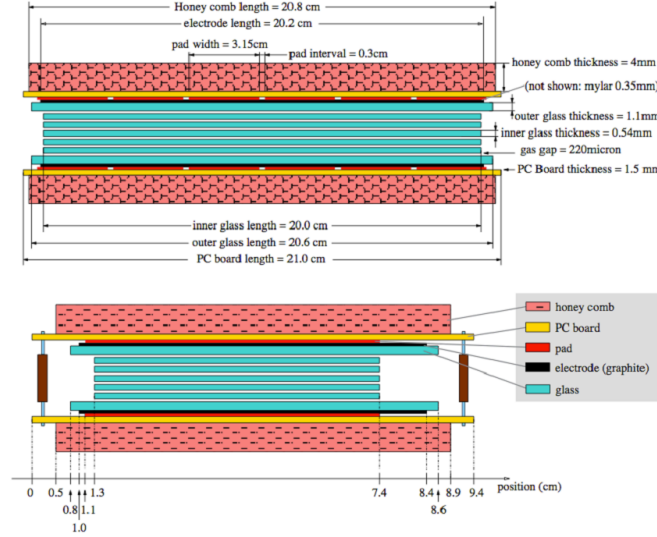
Fig. 2.7   The structure of a single MRPC module in long (upper picture) and short (lower picture) side view.
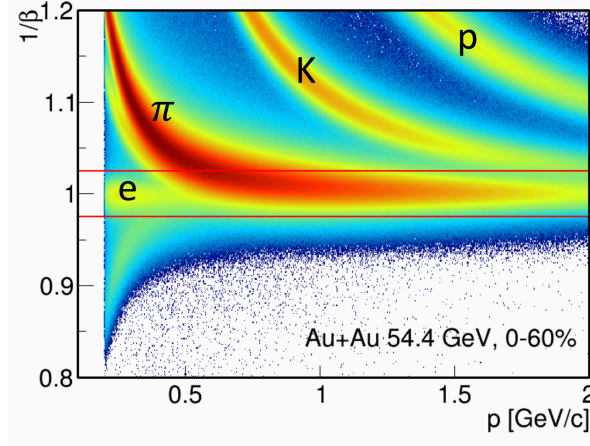
Fig. 2.8 $1/\beta$ distribution as a function of momentum for charged particles in Au+Au $\sqrt{s_{\mathrm{NN}}} = 54.4$ GeV.

GeV/c. Fig. 3.6a shows the $1/\beta$ distribution of charged particles measured by TOF in Au+Au $\sqrt{s_{\mathrm{NN}}} = 54.4$ GeV.

2.5   Heavy Flavor Tracker

The Heavy Flavor Tracker (HFT) was installed in the STAR detector during RHIC run year 2014-2016. It is consisted of 3 silicon sub-detectors with 2π azimuthal coverage, including one-layer Silicon Strip Detector (SSD) [105] in the outmost, one-layer Intermediate Silicon Tracker (IST) and the two-layer PIXEL (PXL) [106] detector in the innermost. The PXL detector is based on the first generation of Monolithic Active Pixel Sensors (MAPS) sensors. The second generation of MAPS sensors will be ap-

plied to ALICE ITS2 and sPHENIX MVTX detector. The schematic view of the HFT lay-out is shown in Fig. 2.9 [107]. Some basic parameters for 4 layers of HFT detector are listed Table 2.1 [108]. Fig. 2.10 shows the DCA resolution of identified particles in the transverse plane (XY) as a function of p_T in Au+Au $\sqrt{s_{\mathrm{NN}}} = 200$ GeV collision in Run 2014 [83]. With HFT detector, the DCA resolution of the tracking system can achieve ~ 30 μm at $p_T = 1.5$ GeV/c in both XY plane and along the beam direction, while the life time of D^0 is about ~ 200 $\mu m/c$. The excellent DCA resolution provided by HFT detector enables precise measurements of heavy flavor hadrons in the STAR experiment by reconstructing their displaced secondary vertex.
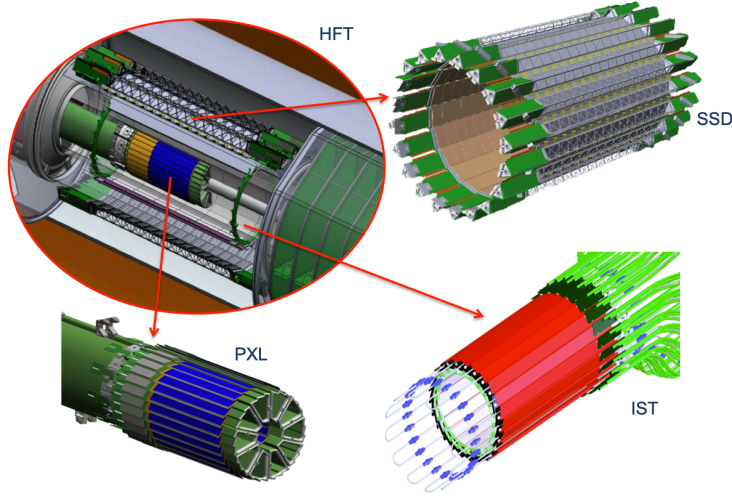
Fig. 2.9   The schematic view of the HFT lay-out. Taken from [107].

Table 2.1   Basic parameters for different layers of HFT [108].

Items	PXL-1	PXL-2	IST	SSD
Radius (cm)	2.8	8	14	22
Length (cm)	20	20	50	106
Radiation thickness	$\sim 0.39\%$ X_0 [*]	$\sim 0.52\%$ X_0	$< 1.5\%$ X_0	$\sim 1\%$ X_0
$|\eta|$ coverage ($<$)	2.0	1.0	1.2	1.2
Sensitive units (μm$\times\mu$m)	20.7$\times$20.7	20.7$\times$20.7	600$\times$6000	95$\times$73000

[*] The radiation thickness of PXL-1 was 0.52% X_0 in 2014, and changed to 0.39% X_0 in 2015 and 2016.
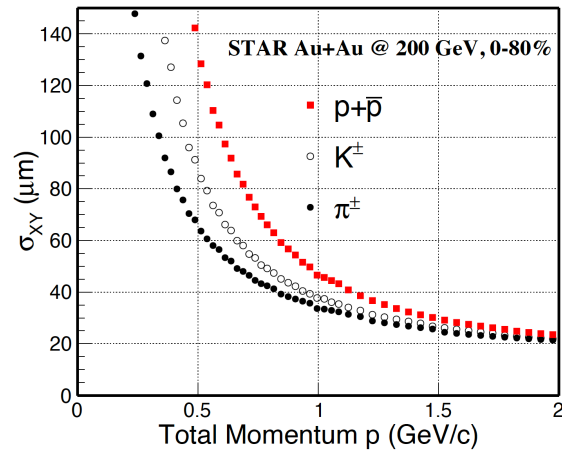
Fig. 2.10   DCA resolution of π, K and p in the transverse plane (XY) as a function of p_T in Au+Au collision in Run 2014 [83].

Chapter 3   Measurements of elliptic flow of heavy flavor electrons

In this chapter, we will discuss the measurement of elliptic flow (v_2) of the electron from heavy flavor hadrons decay (e^{HF}) in Au+Au collisions at $\sqrt{s_{NN}}$ = 54.4 and 27 GeV at the STAR experiment.

3.1   Overview of the analysis

The STAR collaboration has dedicated measurements on charm mesons and baryon via hadronic decay channels at Au+Au 200 GeV utilizing Heavy Flavor Tracker (HFT)[65, 83, 109]. When going to low energies, direct construction of heavy flavor hadrons becomes quite challenging. The charm hadrons production cross section decreases faster with the decrease of collision energy $\sqrt{s_{NN}}$ than that of the light flavor hadrons. The HFT detector has been removed in the BES II program. It is difficult to suppress combinatorial background purely relying on the TPC tracking if constructing heavy flavor hadrons through typical hadronic decay channels directly[82-83]. Hence, the semileptonic decay channel is a better solution to access the heavy flavor properties in the hot medium at low energy in the STAR experiment.

The correlations between the heavy quark and the electrons can be examined with p+p 54 GeV events generated by PYTHIA 8. We calculate $<cos(\phi_e - \phi_{c/b})>$, as a function of electron transverse momentum, where ϕ is the particle azimuthal angle. Heavy flavor electron can well represent their parent quark (charm/bottom) directions at $p_T > 1.2$ GeV/c, where $<cos(\phi_e - \phi_{c/b})>$ is larger than 0.95, as shown in Fig. 3.1.
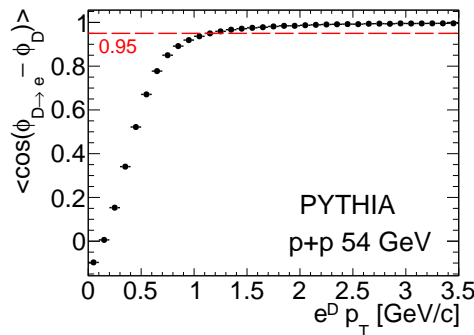
Fig. 3.1   The correlation between the azimuthal angle of e^{HF} and that of their parent quark as a function of e^{HF} p_T.

In order to extract heavy flavor electrons e^{HF}, one need to identify the inclusive

electrons e^{inc} and then substract the background electrons. The main sources for the background electrons are from photon conversion and pseudo-scalar meson (mainly from π^0 and η) Dalitz decay, so the heavy flavor electrons e^{HF} are also called as "Non-Photonic electrons" and the background are called as "Photonic electrons" (e^{pho}). To calculate the number of photonic electrons, reconstruction method is used, which will be discussed later in section 3.4 and 3.5. Then the number of the heavy flavor electrons can be written as:

$$N^{e^{HF}} = N^{e^{inc}} \cdot p - N^{e^{pho}} \tag{3.1}$$

where p is the purity of inclusive electron after electron identification (eID) cut. Based on the definition of flow Eq: 3.2, the heavy flavor electron elliptic flow v_2^{HF} can then be calculated as Eq. 3.3, where v_2^{pho} is the photonic electron v_2. The ratio refer to the fraction of the contamination hadrons in the inclusive electrons after eID and v_2^h is their elliptic flow. Details of the elliptic flow extraction will be discussed in section 3.8.

$$E \frac{d^3N}{d^3p} = \frac{d^2N}{2\pi p_T dp_T dy}(1 + \sum_{n=1}^{\infty} 2v_n cos[n(\phi - \Phi)]) \tag{3.2}$$

$$N^{e^{HF}} \cdot v_2^{HF} = N^{e^{inc}} v_2^{inc} - N^{e^{pho}} v_2^{pho} - \sum_{h=\pi,K,p} f_h \cdot N^{inc} v_2^h \tag{3.3}$$

3.2   Data set and event selection

This analysis is based on the minimum bias triggered data collected in RHIC run year 2017 and 2018. The trigger IDs used in the analysis are summarized below:

- Au+Au 54.4 GeV: 580001, 580021
- Au+Au 27 GeV: 610001, 610011, 610021, 610031, 610041, 610051

The concept of centrality is widely used to describe the percentile of hadronic cross section in heavy ion collisions, which is directly related to the impact parameter b of the collision[110]. It can be determined by comparing charged particle multiplicity (N_{ch}) between data and Glauber model[46, 111-112]. Considering overall statistics, we choose to use only one centrality bin, 0-60%, in the analysis.

A series of event level cuts on primary vertex position are applied in order to reject bad events, which are summarized below. Primary vertex is reconstructed by Time Projection Chamber (TPC) tracks. The origin of the frame is defined at the center of the STAR detector and the Z-direction is along the beam direction.

- $\sqrt{V_x^2 + V_y^2} < \mathbf{2\ cm.}$ Require the collisions inside the beam pipe.

- $|V_z^{VPD} - V_z^{TPC}| < 3$ cm. Vertex Position Detector (VPD) is two fast detectors sitting at east and west side of the TPC. VPD can also provide a vertex position along the beam direction from the time difference of the two detectors' signal. This cut is for suppression of pile-up events. It is only applied to the 54.4 GeV data. For 27 GeV data, due to the lower multiplicity, the VPD firing probability is much less. To save statistics, we don't require the $V_z^{VPD} - V_z^{TPC}$ cut for 27 GeV data. The luminosity for Au+Au 27 GeV running is lower, so the pile-up effect is small in 27 GeV even without the V_z difference cut.

- $|V_z| <$ **35 cm.** This cut is selected based on two considerations. First is the collisions should happen within the central region of the TPC to ensure uniform acceptance. Secondly, as the main backgrounds in this analysis are from photon conversion electrons. To increase the signal to background ratio, we need to avoid collisions happens around high density materials. To choose the suitable V_z and pseudo-rapidity (η) range, we select electrons with rough PID cut $0.75 < n\sigma_e < 2$ && $|\frac{1}{\beta} - 1| < 0.025$, and plot 2D distribution of the number of identified electrons in each event as the function of V_z and η, shown in Fig.3.3. The bump structure at $|V_Z| > 40$ cm in Fig.3.3 come from the photon conversion electrons converted at the supporting structure of the beam pipe, which is perpendicular to the Z-direction and located at about $V_z \sim 54$ cm [113]. The cut is set on $|V_z| < 35$ cm and $|\eta| < 0.8$ to avoid the bump structures.

- $|V_x, V_y, V_z| > 10^{-5}$ **cm.** Require the events have valid vertex information.
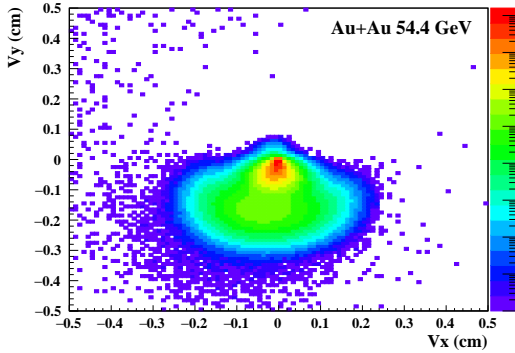
Fig. 3.2   The primary vertex distribution in XY-plane (V_x verus V_y)
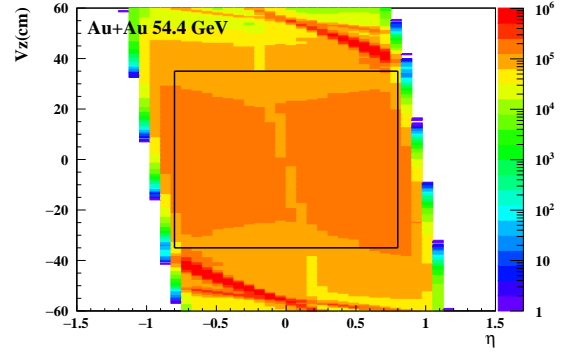
Fig. 3.3   The number of electrons as a function of Z-direction of the primary vertex (V_z) and the η of tracks.

We use the multiplicity measured by the TOF to further suppress pile-up events. Figure 3.4a shows the correlation of multiplicity measured by the TPC and the TOF for Au+Au collisions at 27 GeV. There is strong correlation for good events but outliers for pile-

up events. We applied the following cut to select good events. Figure 3.4b shows the distribution of reference multiplicity measured by TPC before and after the cut for Au+Au collisions at 54.4 GeV. Below cuts are applied for the reduction of pile up events:

- Au+Au 54.4 GeV: TOF Multiplicity>TPC Refmult ×2.88-155
- Au+Au 27 GeV: TPC RefMult ×1.8+15>nTofMatch>TPC RefMult×0.75-20

(a) TOF Multipicity verus Refmult.

(b) RefMult w and w/o cut.
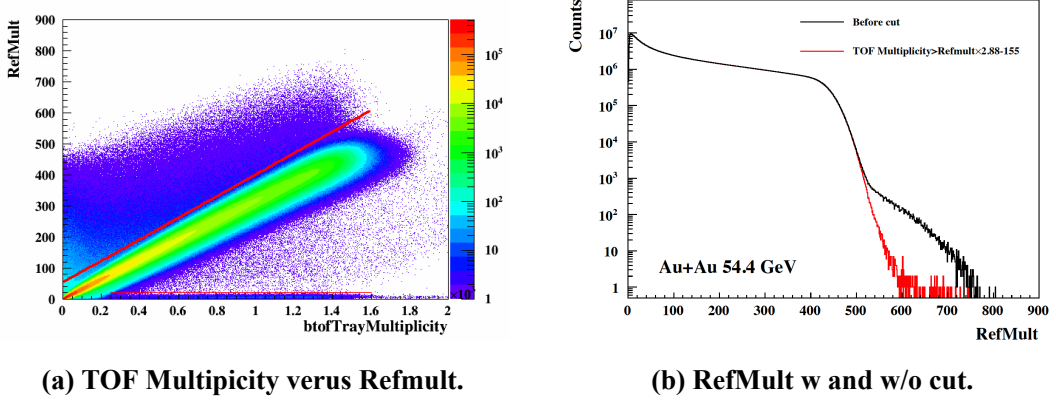
Fig. 3.4   Refmult distribution and pile up rejection.

A summary of the production library, as well as the data sample size after event selection are listed in the Table 3.1.

Table 3.1   Number of events used in this analysis

Year	Energy	Library	Vertex Z cut	Total statistics
2017	54.4 GeV	P18ic	$|V_z|$ <35 cm	558 M
2018	27 GeV	P19ib	$|V_z|$ <35 cm	239 M

3.3   Inclusive electron selection and purity calculation

3.3.1   Track selection

The life time of heavy flavor hadrons is very short compared to the TPC track pointing resolution, so heavy flavor electrons can be regarded as coming from primary vertex. Table 3.2 lists the track quality cuts for the inclusive electrons. We set cut on global track's Distance to the Closet Approach (DCA) to the primary vertex and require tracks must be primary tracks. Track quality cuts can not only ensure better momentum resolution but also help to reduce photon conversion electrons, which is one of the main background sources in this analysis. Because the start position of photon conversion electrons are usually far away from the primary vertex. The ϕ distribution of inclu-

sive electrons after basic track quality cuts is shown as the black line in Fig. 3.5. To suppress the electrons originated from photon conversions in the TPC gas, we require that the single electron tracks must have at least 1 hit in the first 3 TPC layers, which is equivalent to that the position of the first hit point of the track is $\sqrt{x^2 + y^2} < 70$ cm. The two peaks of the black line in Fig. 3.5 around $1.25 < |\phi| < 1.95$ are due to the electrons converted in the support structure of the beam pipe along the Z-direction. The tracks within $1.25 < |\phi| < 1.95$ region would be rejected to reduce the fraction of photon conversion electrons in inclusive electrons.
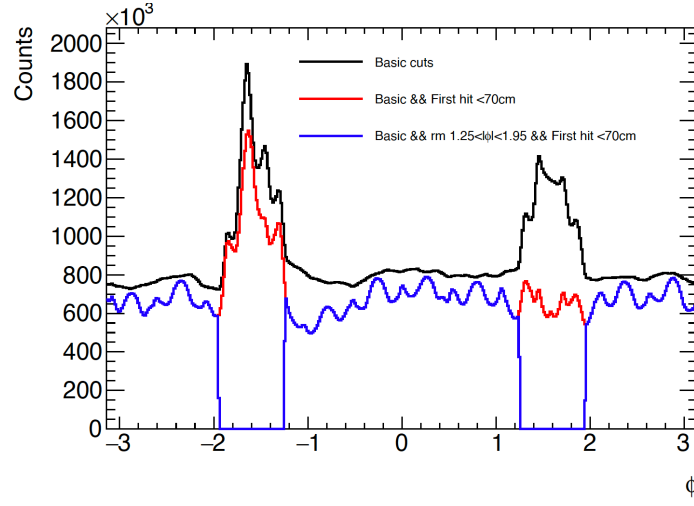
Fig. 3.5   Inclusive electron ϕ distribution with different cuts in Au+Au 54.4 GeV

3.3.2   Inclusive electron identification

The inclusive electrons are required to be identified by combining the information measured by TPC and TOF. TPC is able to distinguish different particle species by measuring particle ionization energy loss (dE/dx) in the TPC gas (Eq 2.1). Experimentally, the normalized dE/dx, $n\sigma_x$ (x can be π, K, p, e etc.) is widely used. The definition of which is shown in Eq. 3.4:

$$n\sigma_x = \frac{1}{R} \ln \frac{\langle dE/dx \rangle_{measured}}{\langle dE/dx \rangle_x} \tag{3.4}$$

where $\langle dE/dx \rangle_{measured}$ is the measured track mean $\langle dE/dx \rangle$ and $\langle dE/dx \rangle_x$ is expected mean $\langle dE/dx \rangle$ if assuming the track is particle x, and R is STAR TPC ln(dE/dx) resolution, depending on number of hits in the TPC used for dE/dx measurement (nHits-Dedx), pseudo-rapidity of the track, momentum of the track, TPC gas component and so on. Combining with the track information provided by TPC, the TOF system are able to identify particles with the same momentum but different masses according to the inverse velocity ($1/\beta = c\tau/L$). The PID cuts for inclusive electron selection are

Table 3.2   Inclusive electron selection track quality cuts for both energy

Basic cuts	
$p_T > 0.2$ GeV/c	Make sure tracks can pass through the TPC
$|\eta| < 0.8$	See Fig. 3.3
$|gDCA| < 1.5$ cm	DCA to the priamry vertex, which is to reduce tracks coming from secondary vertex.
Primary track	Require tracks coming from primary vertex, which is to supress secondary vertex tracks and ensure better momentum resolution.
nHitsFit> 20	Number of TPC hit points used in the track fitting. The maximum hit points is 45.
nHitsDedx> 15	Number of TPC hit points used in <dE/dx> measurement
nHitsFit/nHitsMax> 0.52	Ratio of used and maximum possible number of TPC hit points, which is to avoid one track splitting into two tracks
Cuts for photon conversion electron rejection	
TopologyMap[0]>>8 & 0x7	Having at least 1 hit in the first 3 TPC Pads, which is to reduce the photon conversion electrons produced in the TPC gas.
$|\phi| < 1.25$ or > 1.95	Avoid the ϕ region where detector material density is high

summarized in Table 3.3. Fig.3.6a shows $1/\beta$ distribution from TOF. A band below $1/\beta = 1$ is observed in Fig.3.6a. In high multiplicity environment, if the particle hit the TOF detector without leaving a trace in the TPC, such as neutral particles or electrons converted at the materials in the space between TPC and TOF, the hit would be associated with a TPC track from charged particles[114]. The tachyon band and pion band are merged with electron band at $\sim p_T > 0.5$ GeV/c, bringing the hadron contamination to the TOF-seleted electron samples. Fig.3.6b is dE/dx distribution as function as momentum after TOF selection.

Table 3.3   Inclusive electron selection PID cuts for both energy

Cuts	Notes
$p_T < 0.8$ GeV/c: $p \times 3.5 - 2.8 < n\sigma_e < 2$ $p_T > 0.8$ GeV/c: $0 < n\sigma_e < 2$;	TPC dE/dx
$\lvert 1 - \frac{1}{\beta} \rvert < 0.025$	TOF $1/\beta$
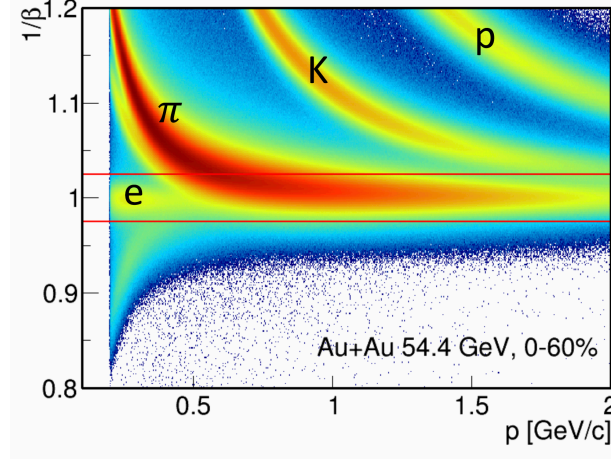
(a) $1/\beta$ distribution from TOF
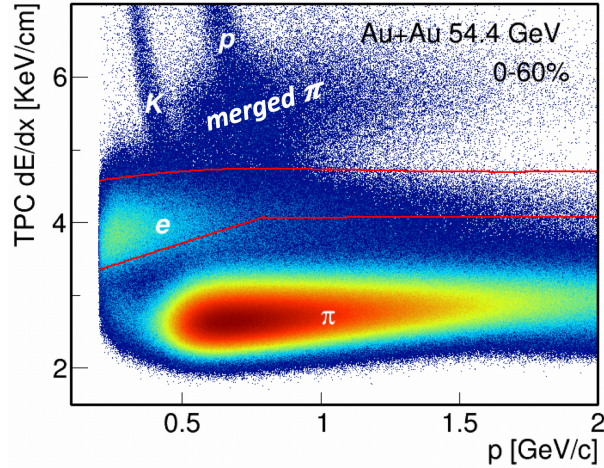
(b) TPC dE/dx distribution after TOF selection

Fig. 3.6   Electron identification.

3.3.3 Electron purity study

One important thing in this analysis is to estimate the purity of inclusive electrons. As it is shown in Fig. 3.6b, there are some momentum regions where electron dE/dx band crosses over with other hadrons. In these momentum regions, electron purity will drop very quickly. To ensure the systematic uncertainty is under control, these regions

will be excluded and only the p_T range with high electron purity will be used in later on analysis.

We estimate the electron purity by fitting $n\sigma_e$ distribution to determine electrons relative yield within PID cut range. We project $n\sigma_e$ in fine momentum bins (Fig. 3.6b), so that $n\sigma_e$ distributions of hadrons are close to Gaussian distribution. As we have seen in Fig. 3.6b, in addition to identified particles, such as π/K/p, so called merged pions are also one of the hadron contamination sources. When two tracks are too close to each other, TPC can't separate them due to finite spatial resolution. These tracks would be recorded with approximately two times larger dE/dx than normal pions (Because π meson production yield is highest among all final state particles). Merged pion samples can be selected by TOF identified pion with large dE/dx. K/p samples are extracted by TOF PID. π samples are extracted by two methods, reconstructing $K_s \rightarrow \pi\pi$ or TOF PID. Pion samples from $K_s \rightarrow \pi\pi$ is pure but the statistics is limited at $p > 2.5$ GeV/c, so we regard this method as the default one. Detailed cuts for particle samples are listed below:

- p: $|M^2 - 0.879| < 0.02$ GeV^2/c^4, $|n\sigma_p| < 4$
- K: $|M^2 - 0.243| < 0.005$ GeV^2/c^4, $|n\sigma_K| < 4$
- π (from TOF PID): $|M^2 - 0.019| < 0.003$ GeV^2/c^4, $|n\sigma_\pi| < 4$
- π (from K_s):

  Tagged pion (0.3<gDCA<3 cm) $|\frac{1}{\beta_\pi} - \frac{1}{\beta_{th}}| < 0.01$,

  Partner pion (0.3<gDCA<3 cm) $|\frac{1}{\beta_\pi} - \frac{1}{\beta_{th}}| < 0.04$,

  Pair cut: K_s DCA < 0.9 cm, K_s decay length > 4 cm, $cos(\theta) > 0.7$, pair DCA < 0.8 cm

- Merged pion: $|n\sigma_\pi| > 5$, $|M^2 - 0.019| < 0.003$ GeV^2/c^4
- $M_{ee} < 0.04$ GeV/c^2, tagged electron $|n\sigma_e| < 2.5$, use partner electron for the electron sample.

Particle samples are shown in Fig. 3.7. The default method for the purity fitting is using Multi-Gaussian fit. Firstly we fit $n\sigma_e$ distribution of different particle samples with normalized Gaussian function and extract σ and mean value. Then fitting the projected Fig. 3.6b utilizing Multi-Gaussian function with fixed width and mean value, as well as free constant value. The total fitting function is shown in Eq. 3.5:

$$f^{total} = C_e \cdot Gaus(\mu_e, \sigma_e) + C_\pi \cdot Gaus(\mu_\pi, \sigma_\pi) + C_K \cdot Gaus(\mu_K, \sigma_K)$$
$$+ C_{merged\ \pi} \cdot Gaus(\mu_{merged\ \pi}, \sigma_{merged\ \pi}) + C_p \cdot Gaus(\mu_p, \sigma_p)$$

(3.5)

Fig. 3.8 shows an example for $n\sigma_e$ Multi-Gaussian fitting. Electron purity is calculated as the integral yield ratio between electron and total fitting function within PID cut
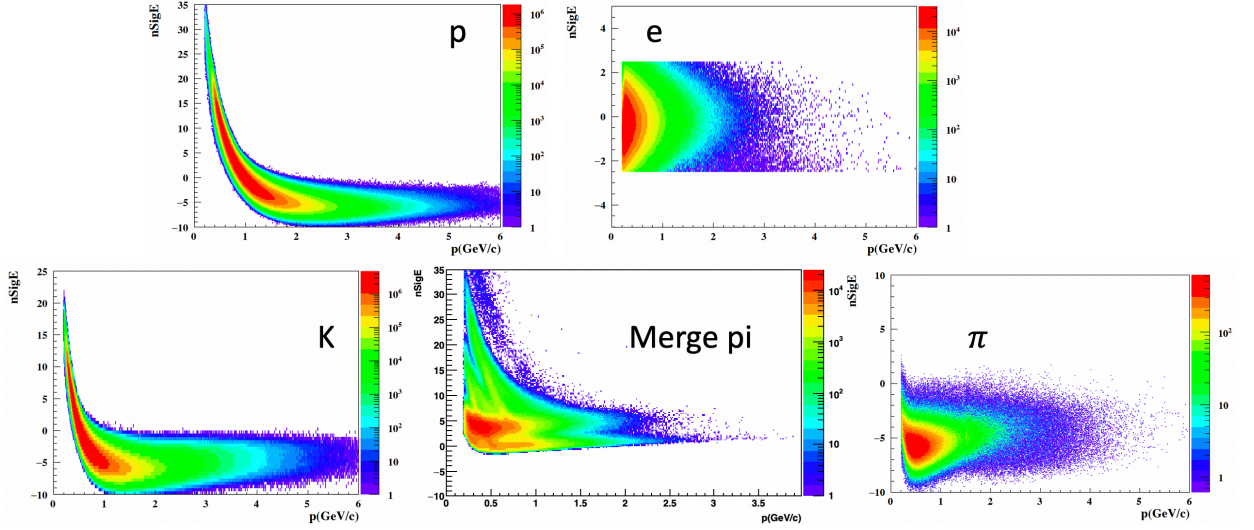
Fig. 3.7   Particle sample $n\sigma_e$ distribution

(Constant parameters are gotten from Multi-Gaussian fitting).

$$\text{purity} = \frac{\int_{n\sigma\ cut} f^e}{\int_{n\sigma\ cut} f^{total}}$$

(3.6)

$$f^e = C_e \cdot Gaus(\mu_e, \sigma_e)$$

For the dE/dx cross over regions, we use exponential function to extrapolate the yield of π and electron, and then set constrains on constant parameters in the function during the fitting. Above procedures will give default electron purity for later on calculation.
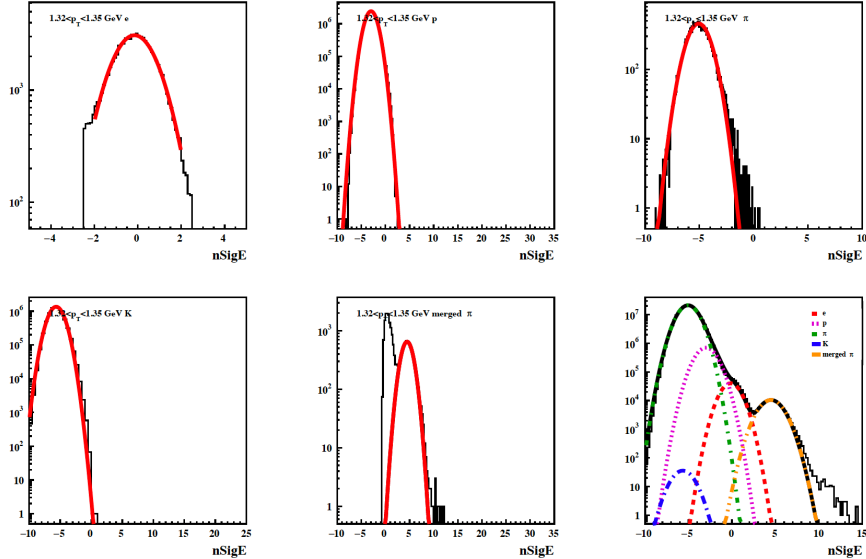
Fig. 3.8 $n\sigma_e$ Multi-Gaussian fitting

For systematic uncertainty, we try several methods and take the largest difference as the systematic error band:

    1. remove constraints on constant parameters in the function, still use Multi-

Gaussian function for fitting.

2. change pion sample to TOF pion, and remove constraints on π constant parameter C_π, and still use Multi-Gaussian function for fitting.

3. replace Gaussian function with normalized pion $n\sigma_e$ distribution histogram in Eq. 3.5, and remove constraints on π constant parameter C_π.

4. change pion sample to TOF pion, use pion $n\sigma_e$ histogram for the purity fitting, and remove constraints on π constant parameter C_π.

In the last step, we need to transform momentum to p_T. We fill 2D histogram Fig. 3.9a after electron PID cut and then profile mean p_T versus momentum Fig. 3.9b.

(a) 2D distribution of p versus p_T (b) Profile of p_T versus p
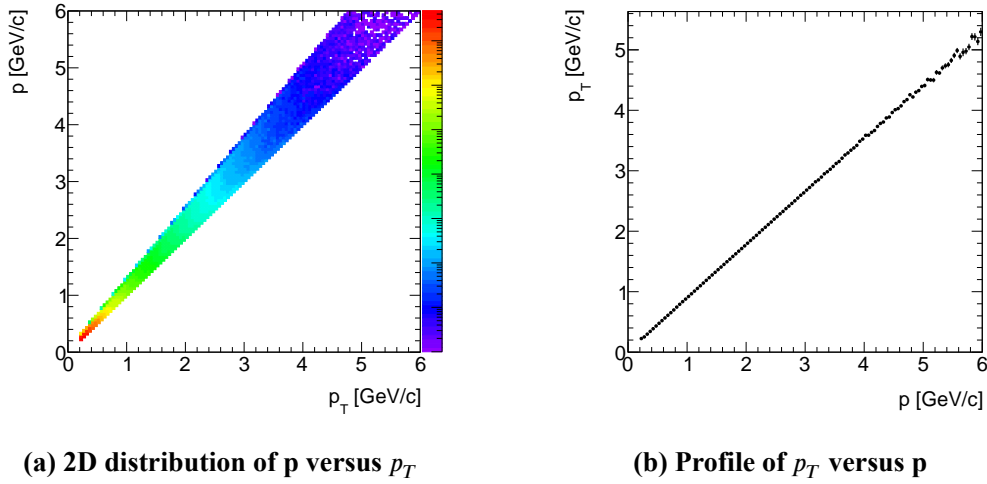
Fig. 3.9   Transport momentum to transverse momentum
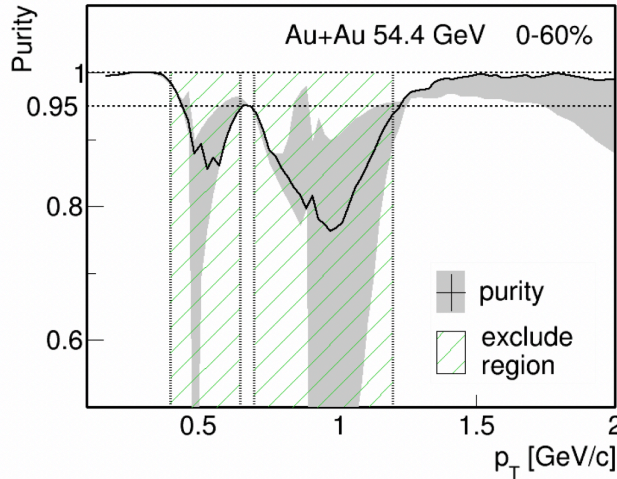
Fig. 3.10   The black line in the plot shows the mean value of inclusive electron purity. The gray band refers to the estimated systematic uncertainty. The p_T range marked in green shadow will be excluded in the analysis because of the low purity and large uncertainties.

The final electron purity is shown in 3.10. Electron purity would decrease very fast at $p_T > 2$ GeV/c because the pion dE/dx moves closer to the electron band. Then the total yield of inclusive electrons can be calculated as

$$e^{Inc} = purity \times e^{PID} \tag{3.7}$$

3.4   Photonic electron tagging

The dominate sources for photonic electrons are listed below:

Dalitz decay:

1. $\pi^0 \rightarrow e^+ e^- \gamma$ (B.R. 1.174%)
2. $\eta \rightarrow e^+ e^- \gamma$ (B.R. 4.22%)

Gamma conversion:

1. $\pi^0 \rightarrow \gamma\gamma$ (B.R. 98.823%)
2. $\eta \rightarrow \gamma\gamma$ (B.R. 39.41%)
3. direct photon

We cannot determine whether a single track is a photonic electron or not, but we can extract the number of photonic electron statistically. The reconstruction method is used for photonic electron tagging, demonstrated in Fig. 3.11a. The tagged electrons, which are the same tracks as inclusive electrons, are paired with partner electrons. Then we reconstruct the invariant mass of electron pair, shown in Fig. 3.11b. The combinatorial backgrounds of the photonic electrons are reconstructed by like-sign method. We set very loose cut for partner electrons and electron pairs to enhance the photonic electron reconstruction efficiency. The cuts are listed below:

Partner electrons:

- global tracks;
- global $p_T > 0.25$ GeV/c, $|\eta| < 1$;
- $|n\sigma_e| < 3$;
- nHitsFit>20, nHitsFit/nHitsMax>0.52.

Electron pairs:

- $M_{ee} < 0.1$ GeV/c^2;
- pair DCA<1 cm.

The total number of photonic electrons can be calculated as:

$$e^{reco} = e^{UL} - e^{LS},$$

$$\text{UL : unlike sign, LS : like sign} \tag{3.8}$$

$$e^{pho} = e^{reco}/\epsilon_{reco}$$

where ϵ_{reco} is the reconstruction efficiency. We will discuss it in the following section.
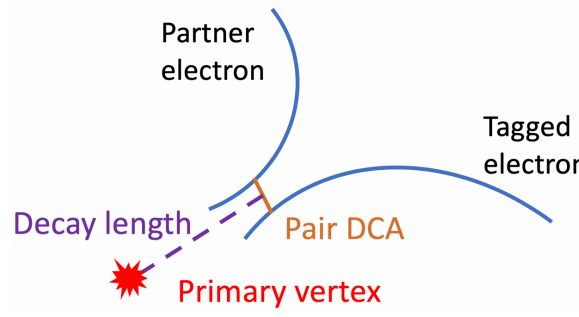
(a) Pairing tagged electrons with partner electrons
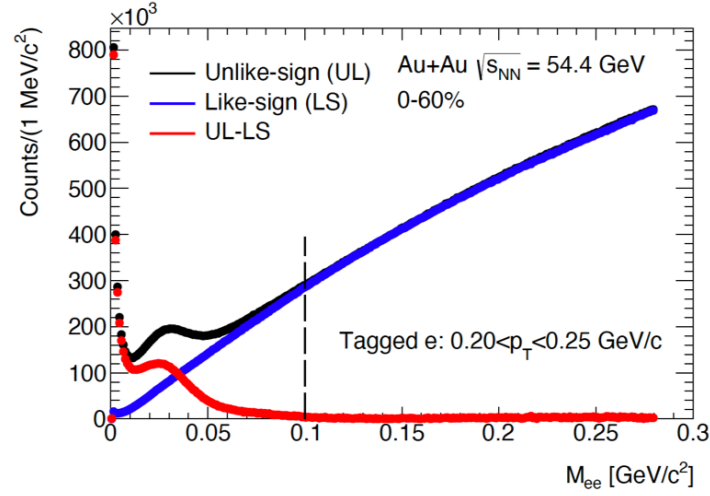
(b) The black data point are the reconstructed photonic electron Ulike-sign signal. The com-
binatorial background is recontructed by Like-sign method. The red data point are the
signals after background subtruction.

Fig. 3.11   Photonic electron tagging.

3.5   Photonic electron reconstruction efficiency

3.5.1   Photonic electron embedding

The reconstruction efficiency is evaluated by standard embedding method. The whole STAR detector is simulated with GEANT3. Monte Carlo particles are embedded into the simulated detector. They fly through the detector, leaving MC hits at the detector sectors. MC tracks are embedded into real events and mixed with hits from real tracks. The real events are randomly selected among entire data sets. Then the embedded events would be reconstructed again following the same procedure as real data process. To avoid disturbing track fitting procedure, the start position of MC particles is set as the primary vertex of the original event, and the number of MC tracks are constrained within certain percentage of event multiplicity. Above procedure is called "embedding". MC tracks and reconstructed tracks are able to be associated by comparing their common hits.

In this analysis, $\pi^0/\eta/\gamma$ are embedded into the simulation[115]. π^0/η are defined as having 100% Datliz decay branching ratio. π^0/η are embedded with 10% event multiplicity while γ is embedded with 100% event multiplicity because conversion probability in STAR is about 1%. Photonic electron will be reconstructed similar as real data analysis, which has been described in section 3.4. The reconstruction efficiency is calculated using reconstructed electron tracks, requiring nCommonHits>10 and passing all of the track quality cuts for tagged electrons. Secondary photon, such as from electron radiation, are excluded in the efficiency study due to their very small momentum. Secondary γ from Dalitz decay will not be considered too because their contribution is negligible as we will discuss later on.

$$\epsilon_{reco} = \frac{\text{Partner electron pass quality cut\&\&electron pair pass reconstruction cuts}}{\text{Total reconstructed electron}}$$

(3.9)

p_T weight need to be set for $\pi^0/\eta/\gamma$, as originally the particles are embedded into the detector with flat p_T distribution. $\pi^\pm/\pi^0$ spectra in Au+Au 39 and 62.4 GeV are used as the input for π^0 spectra, as currently there is no published data for π^0 or $\pi^\pm$ in Au+Au 27 and 54.4 GeV. $\pi^\pm/\pi^0$ data from STAR and PHENIX measurements[116-118] is collected and then fitted with modified Hagedorn function:

$$E\frac{d^3N}{dp^3} = A(e^{-(ap_T+bp_T^2)} + \frac{p_T}{p_0})^n$$

(3.10)

We assume that η particle spectra follow the m_T scaling based on measurements from PHENIX in other collision energies and systems[119-120]. The fitted π spectra is shown

in Fig. 3.12. We replace p_T in π spectra to η p_T, shown in Eq. 3.11, and then scale with normalization factor $\eta/\pi^0 = 0.48$.

$$p_{T\,(\pi)} = \sqrt{p^2_{T\,(\eta)} + m^2_{0\,(\eta)} - m^2_{0\,(\pi)}} \tag{3.11}$$

The input γ spectra have 2 sources: $\pi^0(\eta) \rightarrow \gamma\gamma$ and direct photon. We can decay $\pi^0(\eta) \rightarrow \gamma\gamma$ by PYTHIA. To ensure the detector acceptance, we sample π^0/η kinematics within $|\eta| < 1.5$ and $p_T < 15$ GeV/c. The p_T weight for π^0 and η is set according to their spectra gotten above, and then we are able to calculate invariant yield for γ from π^0/η decay. The direct photon spectra follows N_{coll} scaling under different energies and systems while $N_{coll} \simeq (\frac{dN_{ch}}{d\eta})^{1.25} + C[121]$, shown in Fig. 3.15. For the low p_T, we directly take the data point in Au+Au collisions. For high p_T, we scale the spectra in p+p collisions to Au+Au collisions according to $\frac{dN_{ch}}{d\eta}$ in different centralities. For p+p $\sqrt{s_{NN}} = 62$ GeV collisions, the experiment data points are taken from [121-124]. There is no direct photon measurements in p+p collisions at 39 GeV, so we take the value from pQCD calculation [121, 125]. The direct photon spectra is fitted with function[126]:

$$\frac{d^2N}{2\pi p_T dp_T dy} = T_{AA} \times \frac{A_{pp}}{(1 + p^2_T/p_0)^n} \tag{3.12}$$

The p_T weight for electrons in the embedding are set according to their parent p_T. But one should remember to normalize the number of embedded parent particles in a event, because the number of embedded parent particles in each event is proportional to the event multiplicity. In summary, the total weight for photonic electrons yield is given as:

$$p_T \text{ weight} \times \text{B.R.} \times \text{multiplicity weight} \times \text{normalization factor}$$

- p_T weight: dN/dp_T^{parent}
- B.R. : decay branching ratio.
- multiplicity weight: $1/N^{parent}$, N^{parent} is the number of embedded parent particles $\pi^0/\eta/\gamma$ in each event. To avoid fluctuation in low multiplicity events, one may take the average of this factor under each centrality bin, instead of normalizing in each event. The two methods yield a consistent result in the photonic electron yield.
- normalization factor: (p_T range) $\times$(η range). The embedded particles are sampled with a flat distribution in certain p_T and η range.

The tagged electrons in the embedding are corresponding to the photonic electrons that pass track quality cuts. The distribution of tagged electron from different sources and their relative fraction to total photonic electrons are shown in Fig. 3.16. The dominate sources for the photonic electron at low p_T are from π^0 Dalitz decay, while $\pi^0 \rightarrow \gamma\gamma$, $\gamma \rightarrow e^+e^-$ make the largest contribution at $p_T > 1$ GeV/c. Dalitz decay will also produce

γ, such as $\pi^0 \to e^+e^-\gamma$. But considering the branching ratios, its relative contribution (B.R. 1.2%) is very small comparing to $\pi^0 \to \gamma\gamma$ (B.R. 98.8%×2). The impact on the final photonic electron efficiency is negligible.
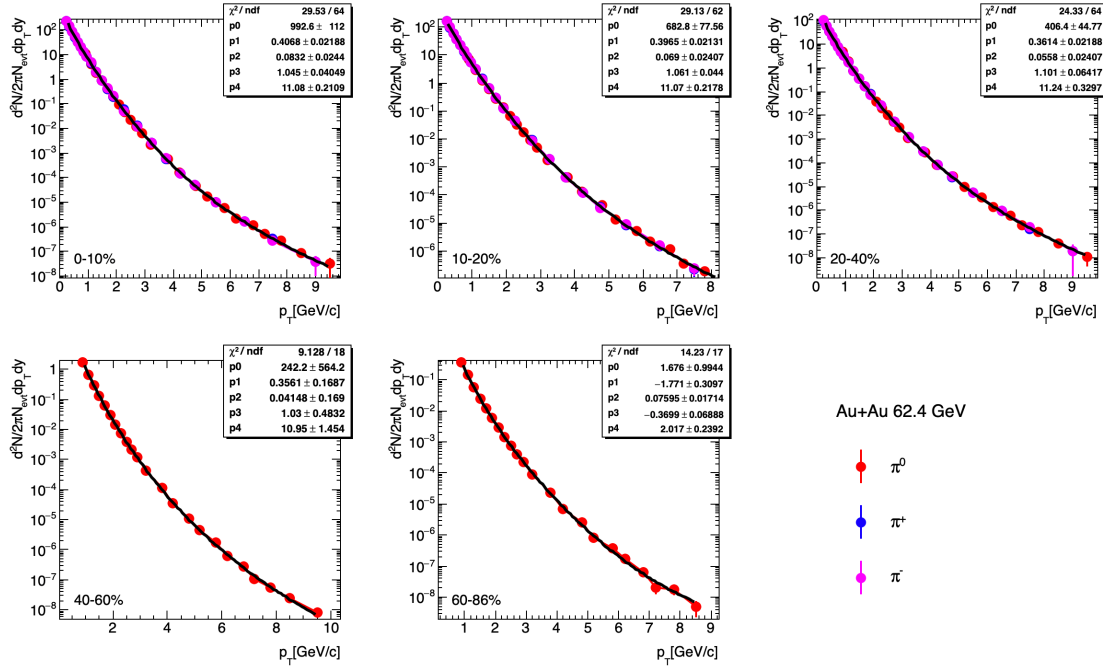
Fig. 3.12 π spectra in Au+Au 62.4 GeV collisions
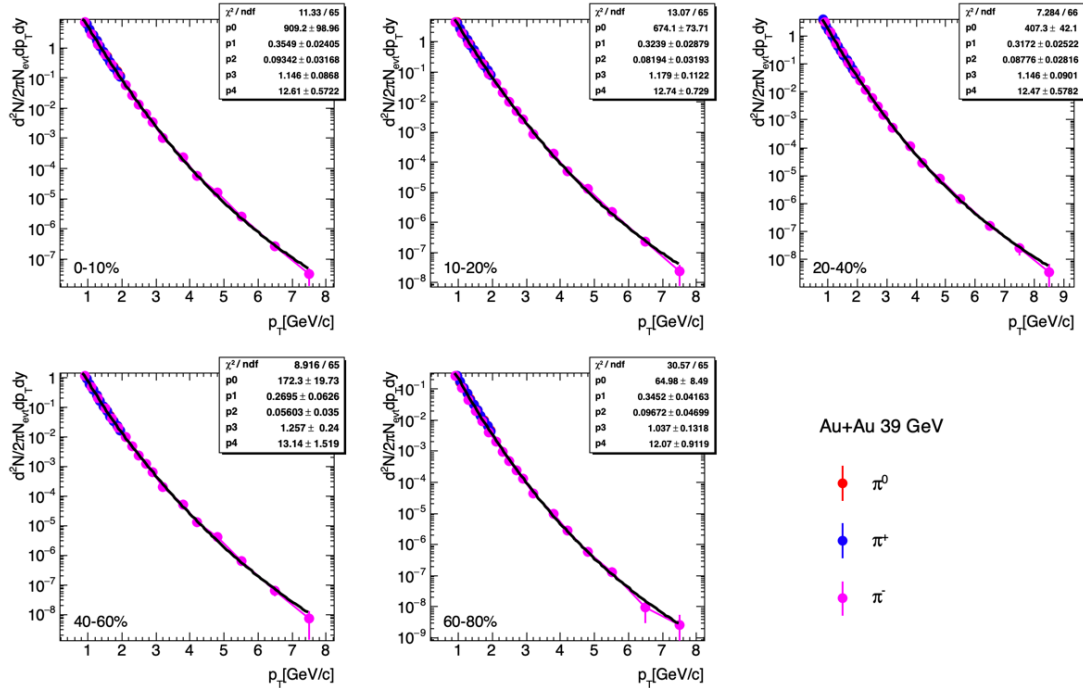
Fig. 3.13 π spectra in Au+Au 39 GeV collisions

45
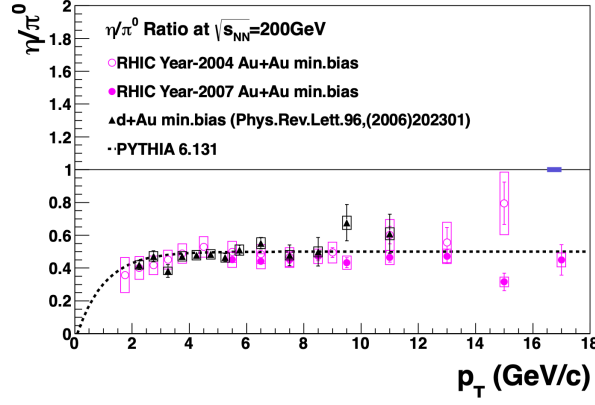
Fig. 3.14 η/π^0 **ratio in Au+Au and d+Au 200 GeV collisions[119]**
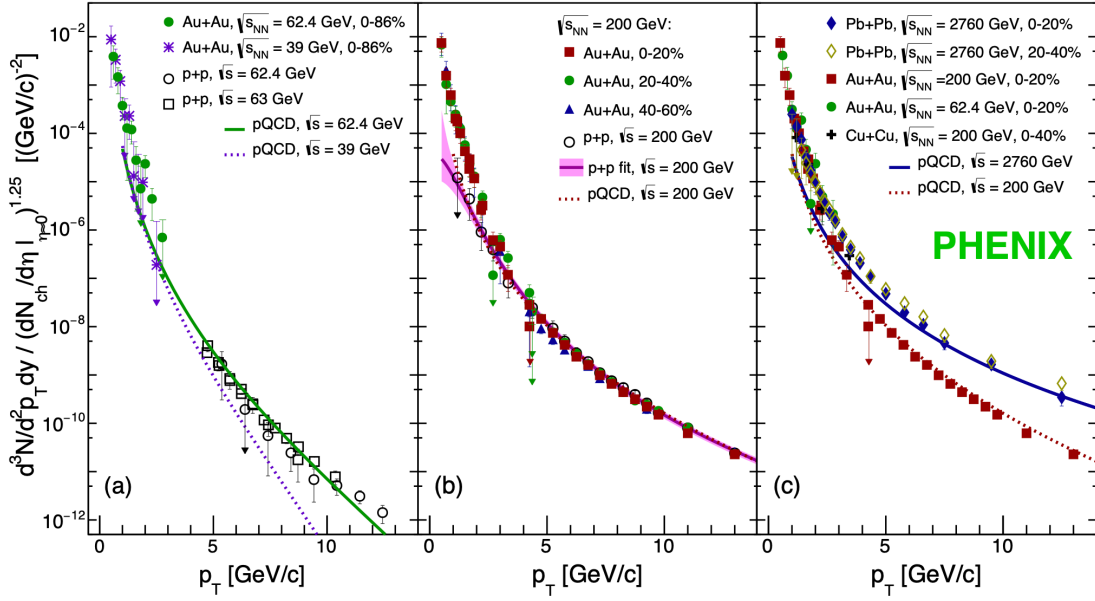
Fig. 3.15   Direct photon spectra normalized by $(dN_{ch}/d\eta)^{1.25}$ in different systems and energies[121]

3.5.2   Embedding QA and Systematic uncertainties

As the reconstruction efficiency is estimated by simulation, it is important to carry out a detailed comparison between simulation and real data to ensure that systematic uncertainty is under control. Fig. 3.40, Fig. 3.41, Fig. 3.18 are the electron pair pair DCA, invariant mass and decay length distribution. The reconstruction efficiency are dominated lost by the p_T cut on partner electron. Fig. 3.17 shows the partner electron p_T distribution. As we can see from these plots, the simulation can describe the data very well. The systematic uncertainties for cuts on partner electron p_T is estimated by comparing the ratio of partner electron yield at $p_T > 0.25$ GeV/c and $p_T > 0.3$ GeV/c from data and simulation. The ratio is calculated by:

$$R(\text{partner electron } p_T) = \frac{\text{Integral yield at } p_T > 0.25 \text{ GeV/}c}{\text{Integral yield at } p_T > 0.3 \text{ GeV/}c} \qquad (3.13)$$
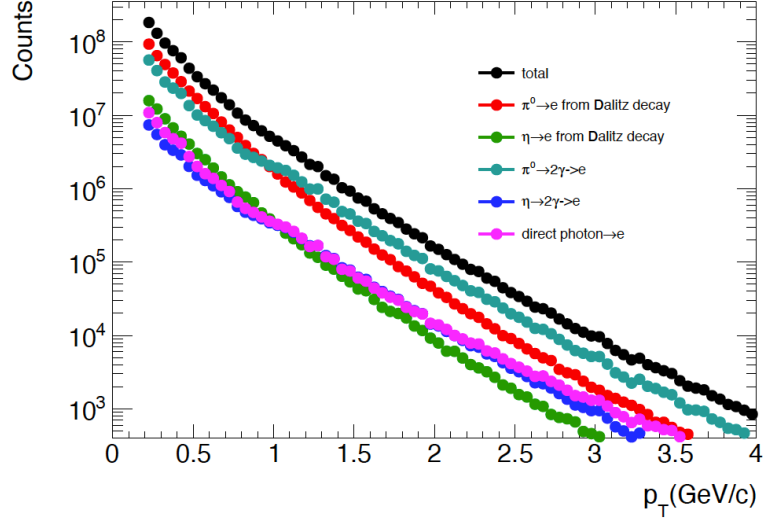
(a) The scaled tagged electron distribution from different sources
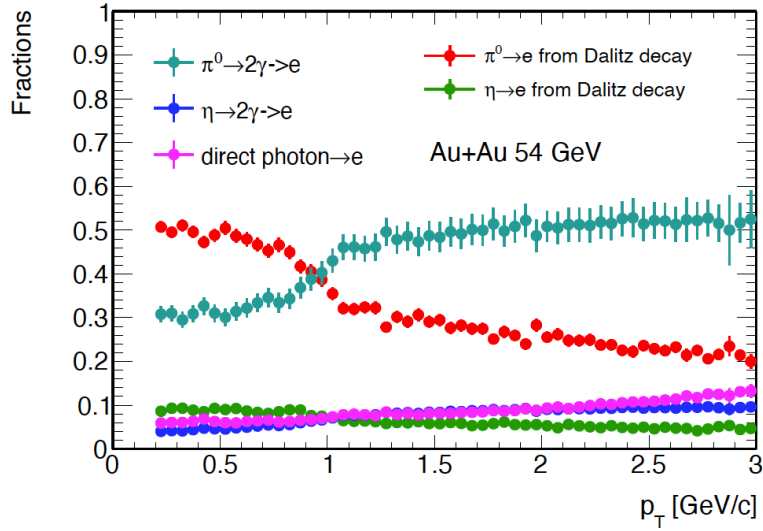
(b) The relative fraction of electrons from different sources in total photonic electrons

Fig. 3.16   Photonic electron sources

Then the relative systematic uncertainty can be calculated as:

$$\text{Sys. Error} = abs\left(\frac{R^{MC} - R^{data}}{R^{data}}\right) \tag{3.14}$$

Similarly, the systematic uncertainty of partner electron nHitsFit cuts is evaluated by the ratio:

$$R(\text{partner electron nHitsFit}) = \frac{\text{Integral yield at nHitsFit} > 25}{\text{ntegral yield at nHitsFit} > 20} \tag{3.15}$$

The systematic uncertainty of electron pair DCA is evaluated by the ratio:

$$R(\text{pair DCA}) = \frac{\text{Integral yield at pair DCA} < 1\text{cm}}{\text{Integral yield at pair DCA} < 1.5\text{cm}} \tag{3.16}$$

The systematic uncertainty of di-electron invariant mass is evaluated by the ratio:

$$R(\text{Invariant Mass}) = \frac{\text{Integral yield at Inv. Mass} < 0.1 \text{GeV/c}^2}{\text{Integral yield at Inv. Mass} < 0.15 \text{GeV/c}^2} \quad (3.17)$$

The simulation might underestimate or overestimate the detector material thickness. To estimate this kind of systematic uncertainty, we scale the yield of $\gamma \to e$ from simulation to 130% and 70%, and take the final combined efficiency difference as the systematic uncertainty.

$$\text{Sys.Error(conversion probability)} =$$
$$\text{Max} \left(\left| \frac{\text{Eff}^{\gamma \to e \times 130\%} - \text{Eff}^{\gamma \to e \times 100\%}}{\text{Eff}^{\gamma \to e \times 100\%}} \right|, \left| \frac{\text{Eff}^{\gamma \to e \times 70\%} - \text{Eff}^{\gamma \to e \times 100\%}}{\text{Eff}^{\gamma \to e \times 100\%}} \right| \right) \quad (3.18)$$
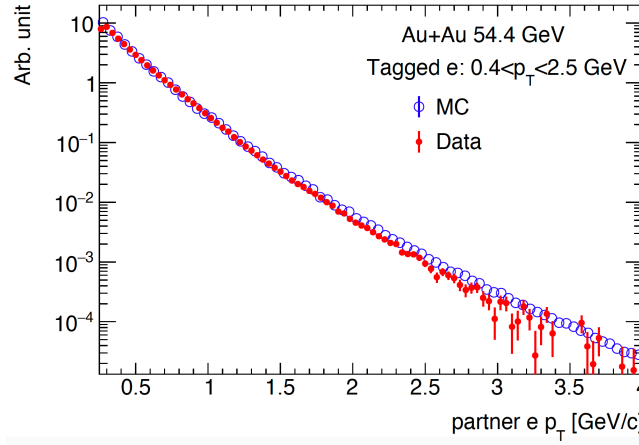
Fig. 3.17   The p_T distribution of partner electron at Au+Au 54 GeV from simulation and data.
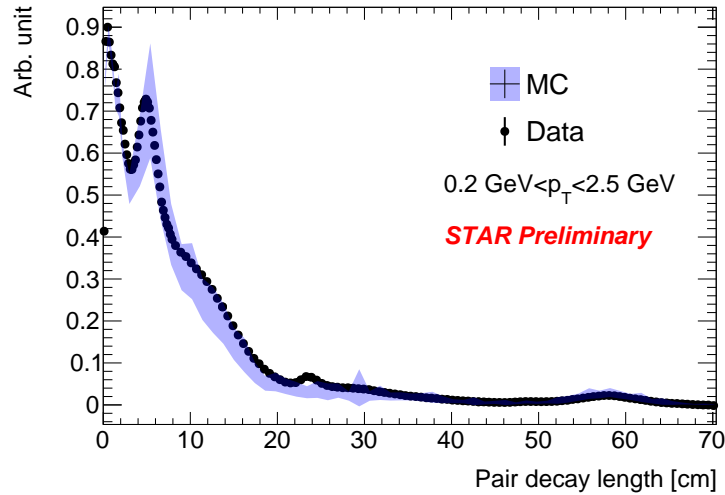
Fig. 3.18   The decay length distribution of the electron pair at Au+Au 54 GeV from simulation and data.

In decay length plot (Fig. 3.18), the peaks around 0 cm are from Dalitz decay while the peaks around 4-5 cm are coming from gamma conversion in the beam pipe, and
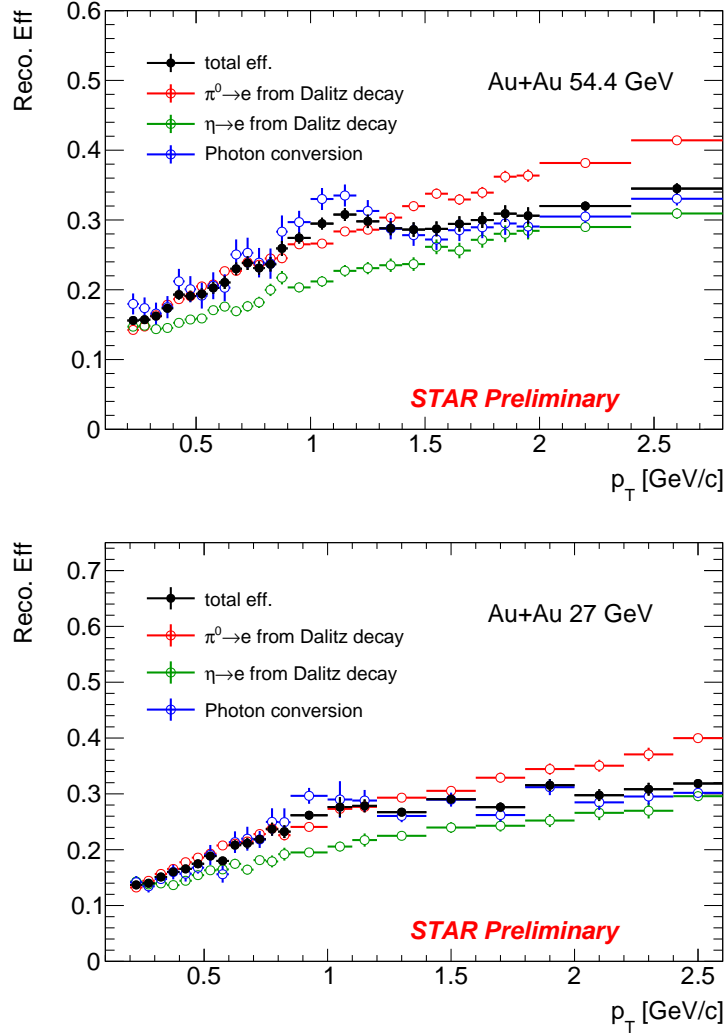
Fig. 3.19   Photonic electron reconstruction efficiency from different sources.

the small bump around 50 cm are from conversion electrons at field cage. From decay length comparisons, we can see the simulation can describe the relative fraction of electrons from gamma conversion and Dalitz decay, which means, the detector simulation can describe the material density distribution of the STAR detector.

3.5.3   Check on the bump structure in efficiency plots

One may observe the bump structure in the reconstruction efficiency plots (Fig. 3.19) around 0.8 GeV/c. After careful investigation, the conversion electrons from the TPC inner field cage account for this bump structure. We split tracks in two groups according to whether the radius of their start vertex in XY plane is large than 40 cm or not. For those tracks converted far away from the primary vertex, only when they match certain conditions, they are able to pass the track quality cuts, such as requiring it to be primary track and global DCA cuts. As a result, TPC inner field cage electrons (radius

(a) The reconstruction efficiency of photon conversion electrons.

(b) The estimated yield of reconstructed electrons from photon conversion.
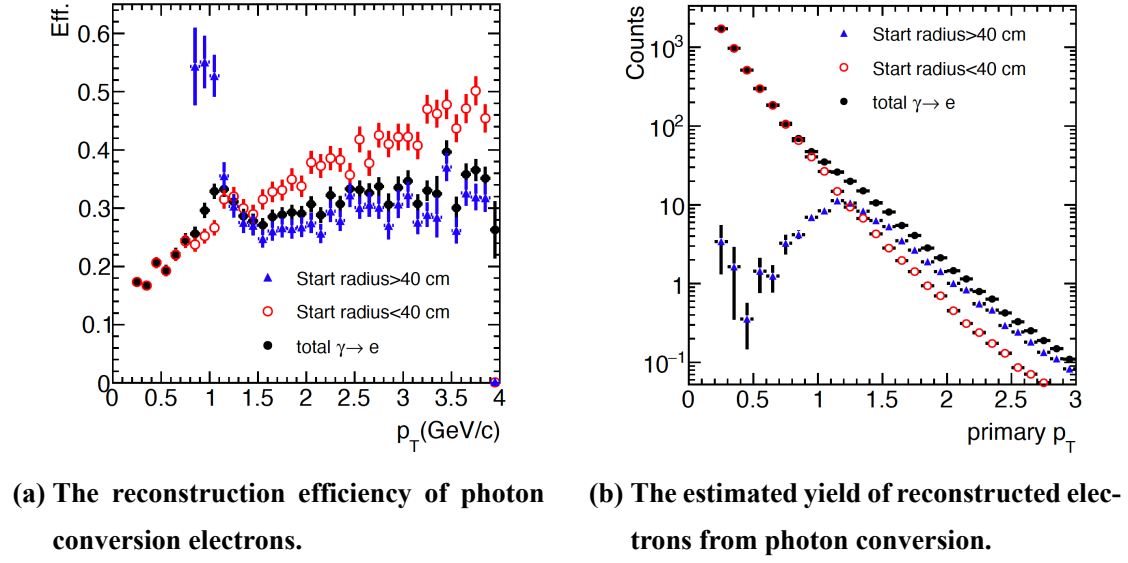
Fig. 3.20   **The electron tracks in the $\gamma \rightarrow e^+e^-$ embedding samples are split into two categories based on start vertex position radius=$\sqrt{x^2 + y^2}$ in XY-plane. The electron tracks with radius> 40 cm are dominantly converted at TPC inner field cage (blue triangle points). Red open circle points are the electron tracks with radius< 40 cm. The black points are total reconstructed electrons from photon conversion. Plot (a) shows the reconstruction efficiency of photon conversion electrons. The electrons converted in the TPC inner field cage tend to have higher possibility to be reconstructed at $p_T < 1.5$ GeV/c. Plot (b) shows the estimated yields of the reconstructed conversion electrons.**

> 40 cm) have higher reconstruction efficiency compared to the electrons converted at the beam pipe (radius < 10 cm), as is shown in Fig. 3.20a. Fig. 3.20b shows TPC field cage electrons are the dominated source of γ conversion electron at $p_T > 1$ GeV/c. Fig. 3.21 shows the track start-vertex radius as a function of momentum resolution R^{Mom}=(rc p_T-mc p_T)/(mc p_T). Track quality cuts have already applied to all the tracks in Fig. 3.21. From this plot, it indicates that reconstructed momentum has correlation with track start-vertex. If the start vertex of the track is away from the primary vertex, the reconstructed primary p_T tend to shift to higher momentum compared to MC p_T.

3.5.4   Reconstruction efficiency results

Systematic uncertainty from different sources are added quadratically. The total systematic uncertainty for is given in Fig. 3.22. Figure 3.23 shows the combined reconstruction efficiency with systematic error band. The error bars represent statistic error from embedding samples. Note, the heavy flavor electron here haven't subtracted
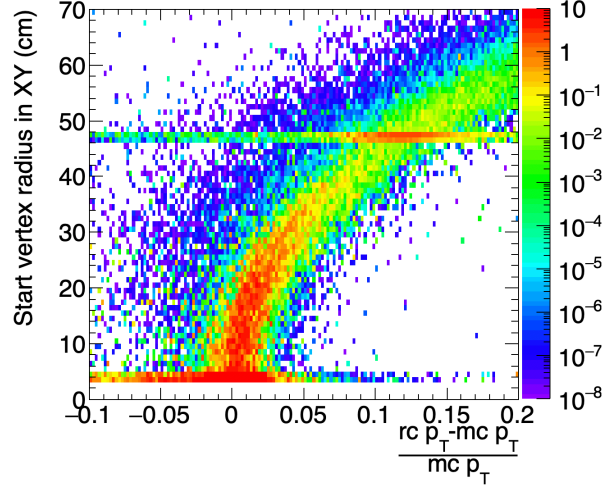
Fig. 3.21   **This plot shows the start-vertex radius of γ conversion electron in XY plane as a function of R^{Mom}=(rc p_T-mc p_T)/(mc p_T) after track quality cuts applied, where rc p_T is the reconstructed primary momentum, and mc p_T is the momentum of the associated MC track. The band at radius ~ 46 cm is contributed by photon conversion electrons converted at the TPC field cage, while the band at radius ~ 4 cm is contributed by electrons converted at the beam pipe.**
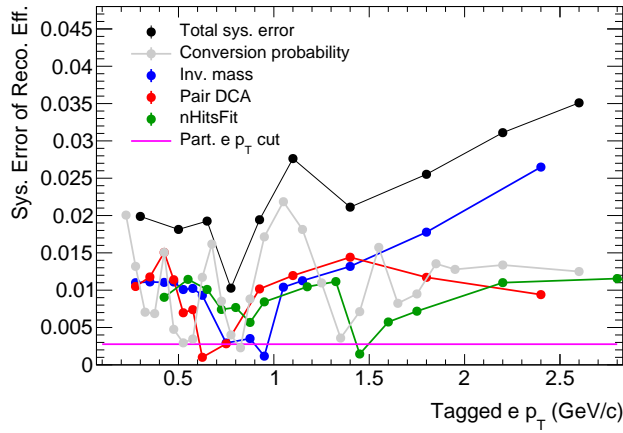
Fig. 3.22   **Systematic uncertainty for reconstruction efficiency from gamma conversion probablity, invariant mass, pair DCA, nHitsFit, .**

contribution from weak kaon decays $K_{e3} \to e$.

$$e^{HF} = e^{inc} \cdot purity - e^{pho} \tag{3.19}$$

$K_{e3} \to e$ contribution can be suppressed by global DCA cut. The estimated K_{e3} contribution at Au+Au 62.4 GeV/c is $\simeq 30\%$ at $p_T < 0.5$ GeV/c and $\simeq 10\%$ at $0.5 < p_T < 3$ GeV/c. With the reconstruction efficiency obtained from the embedding simulation, we are able to calculate the signal to background ratio, e^{HF}/e^{pho}, shown in Fig. 3.24.

$$e^{HF}/e^{pho} = \frac{purity \cdot e^{inc} - e^{pho}}{e^{pho}} \tag{3.20}$$

51

The charm quark production cross section is decreasing when the collision energy goes
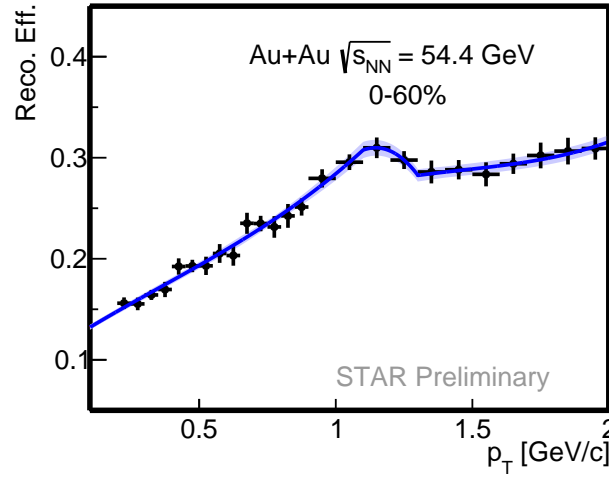
Fig. 3.23 **The photonic electron reconstruction efficiency in Au+Au 54.4 GeV collisions. The date points are directly obtained from embedding. The blue line is the fitting function and the blue band shows the systematic uncertainties.**
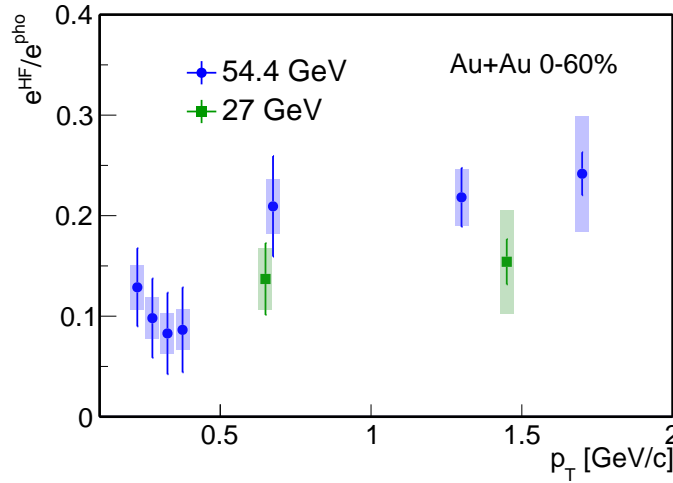
Fig. 3.24 **The non-photonic electron over photonic electron yield ratio as a function of p_T in Au+Au $\sqrt{s_{NN}}$ =54.4 (blue points) and 27 GeV (green points) collisions.**

down, and this kind of decreasing is faster than the production cross section of light flavor quarks. So the signal to background ratio at Au+Au 27 GeV collisions is lower than that of 54 GeV collisions.

3.6　Inclusive electron v_2

The elliptic flow of inclusive electron is extracted by event plane $\eta-$sub method. The estimated reaction plane is called event plane, and in this analysis TPC tracks are used for event plane reconstruction. If the electron has a negative η and then we will

use the tracks within $0.05<\eta<1$ and $0.2<p_T<2$ GeV/c to reconstruct the event plane, as illustrated in Fig. 3.25. The track quality cuts for event plane reconstruction are listed below:

- η gap: 0.05;
- primary track, $0.2<p_T<2$ GeV/c, $|\eta|<1$, $|gDCA|<1.5$ cm;
- nHitsFit>20, nHitsDedx>15, nHitsFit/nHitsMax>0.52.

The first step is to calculate raw event flow vector $\vec{Q}_n$, where n=2 for elliptic flow:

$$q_x = p_T \cdot \cos(2\phi), q_y = p_T \cdot \sin(2\phi) \tag{3.21}$$

$$Q_x^{raw} = \sum q_x, Q_y^{raw} = \sum q_y \tag{3.22}$$

$$\Phi_2^{raw} = \frac{1}{2} \cdot \tan^{-1} \frac{Q_y}{Q_x} \tag{3.23}$$

The event plane Φ_2 should be isotropic. However, raw Φ_2 is not a uniform distribution because the detector acceptance is non-uniform and anisotropic in the real laboratory system. To remove the bias, the simplest method is known as "recentering", which is used in this analysis. The detector system can be regarded as the same in a single run, so recentering correction is done run by run. The corrected $\vec{Q}_2$ and Φ_2 is calculated as:

$$Q_x^{recenter} = Q_x^{raw} - \langle Q_x \rangle_{run} = \sum q_x - \langle q_x \rangle_{run} \tag{3.24}$$

$$Q_y^{recenter} = Q_y^{raw} - \langle Q_y \rangle_{run} \sum q_y - \langle q_y \rangle_{run} \tag{3.25}$$

$$\Phi_2^{recenter} = \frac{1}{2} \cdot \tan^{-1} \frac{Q_y^{raw}}{Q_x^{raw}} \tag{3.26}$$

But recentering method cannot fully eliminate second (and higher) order harmonics of Φ_2^{raw} distribution, so the event plane need to be further flattened by shift method[127]:

$$\Delta\Phi_n = \frac{1}{n} \sum_{i=1}^{i_{max}} \frac{2}{i} \left[-\langle \sin(in\Phi_n) \rangle \cos(in\Phi_n) + \langle \cos(in\Phi_n) \rangle \sin(in\Phi_n) \right] \tag{3.27}$$

$$n = 2, i_{max} = 21 \tag{3.28}$$

$$\Phi_2^{shift} = \Phi_2^{recenter} + \Delta\Phi_2 \tag{3.29}$$

Φ_2^{shift} is the final event plane. The event plane distribution before and after correction is shown in Fig. 3.26a. As we are using $\eta-$sub method, the correlation of two sub-event (a) and (b) can be written as:

$$\langle \cos(2(\Phi^a - \Phi^b)) \rangle = \langle \cos(2(\Phi^a - \Phi_r)) \rangle \cdot \langle \cos(2(\Phi^b - \Phi_r)) \rangle \tag{3.30}$$

The event plane resolution for each sub-event is expected to be the same as the multiplicity is supposed to be equal in $0.05 < \eta < 1$ and $-1 < \eta < -0.05$. Then the event

plane resolution R can be written as:

$$R = \langle \cos(2(\Phi^a - \Phi_r)) \rangle = \langle \cos(2(\Phi^b - \Phi_r)) \rangle = \sqrt{\langle \cos(2(\Phi^a - \Phi^b)) \rangle} \qquad (3.31)$$

The event plane resolution as a function of centrality under different collision energies is shown in Fig. 3.26b. The centrality dependence of event plane resolution in Au+Au $\sqrt{s_{NN}} = 54.4$ GeV collisions follows the similar tendency as 39 and 62.4 GeV collisions. Generally, the event plane resolution is approximately proportional to square root of the event multiplicity multiply the strength of flow v_n [128]. It reaches the highest value in 20-30% centrality. The inclusive electron v_2 is calculated by:

$$v_2 = \langle \frac{\cos 2(\phi - \Phi_{EP})}{R} \rangle \qquad (3.32)$$

The inclusive electron v_2 result is shown in Fig. 3.27.
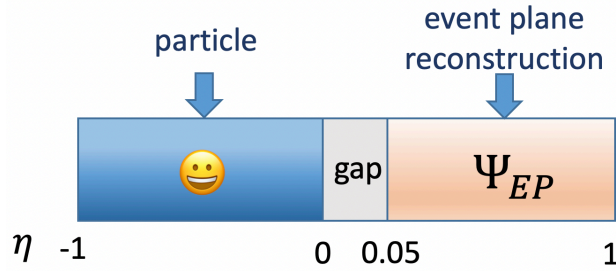
Fig. 3.25   Event plane is reconstructed by $\eta-$sub method

(a) Event plane distribution.

(b) Event plane resolution.
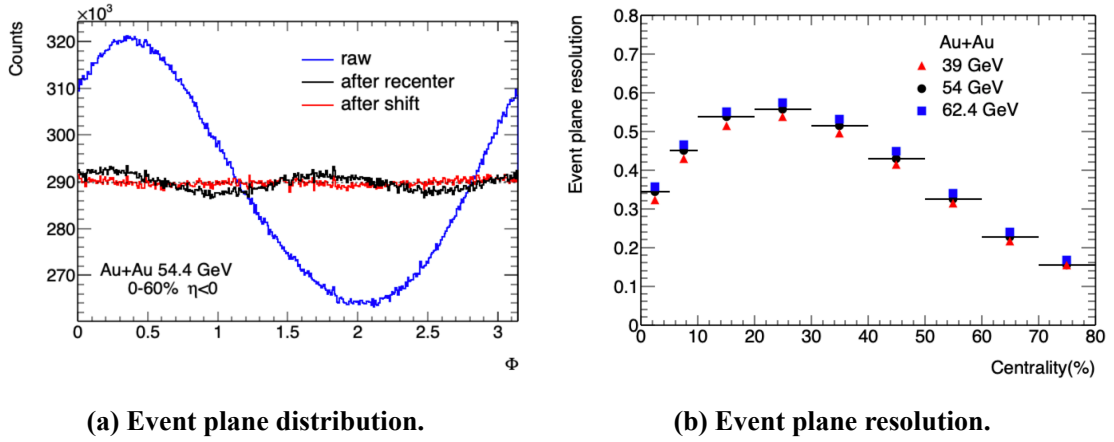
Fig. 3.26   Plot (a) shows the distribution of event plane in 0-60% centrality in Au+Au collisions at $\sqrt{s_{NN}} = 54.4$ GeV. The raw event plane distribution is shown in blue line. After re-centering correction, the event plane distribution still remain 2nd or higher order harmonics, shown in black line. Red line shows the further flattened event plane distribution with shifting method. Plot (b) is the centrality dependence of event plane resolution with $\eta-$sub method in different collision energies.
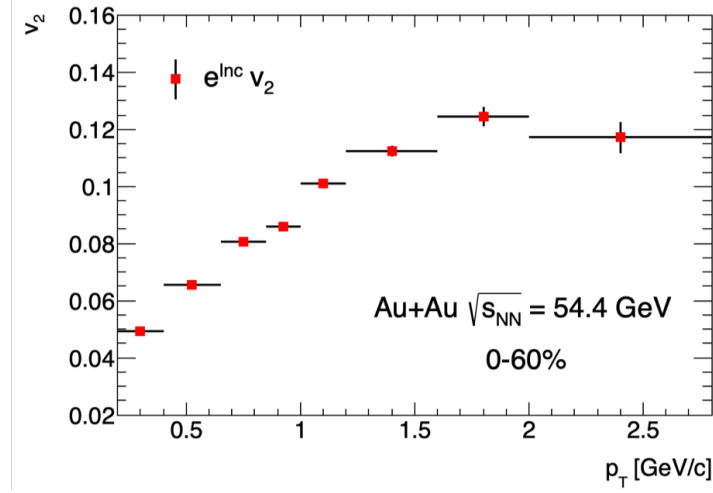
Fig. 3.27 **The inclusive electron v_2 as a function of p_T at 0-60% centrality in Au+Au $\sqrt{s_{\mathrm{NN}}} =$ 54.4 GeV collisions. The inclusive electron v_2 is measured by event plane $\eta-$sub method.**

3.7 Photonic electron v_2

3.7.1 Photonic electron v_2 simulation

As we have mentioned above, the number of photonic electrons can be extracted by reconstruction method statistically. However, due to p_T cuts on partner electrons as well as reconstruction cuts on electron pairs, the mean p_T of the parents of the reconstructed electrons is higher than that of total photonic electrons. As a result, the elliptic flow of reconstructed electrons is higher than that of total photonic electrons at same low p_T because elliptic flow is p_T dependent. Hence, the photonic electron v_2 is calculated using the Monte Carlo embedding data with the input parent particle v_2 determined based on experimental measurements. The flow chart is shown in the Fig. 3.30. Combine with the sentence before.

Firstly, we sample random event plane Φ_2. According to the definition of v_2 in Eq. 3.2, the ϕ weight for electrons is set according to the v_2 of their parent:

$$1 + 2v_2(p_T^{parent}) \cdot \cos(2(\phi^{parent} - \Phi_2)) \tag{3.33}$$

Then the total weight for photonic electrons is:

p_T weight $\times \phi$ weight $\times$ B.R.$\times$ multiplicity weight $\times$ normalization factor

The simulated photonic electron v_2 can be calculated by filling $dN/d\Delta\phi$ histogram with weight ($\Delta\phi = \phi_e - \Phi_2$), and then fitting with $A(1 + 2v_2 \cos \Delta\phi)$.

Because of the centrality dependence of elliptic flow, photonic electron v_2 is calculated in fine centrality bins and then combined together later for minimum bias result. Due to lack of published low energy measurements, we use Au+Au $\sqrt{s_{\mathrm{NN}}} = 62.4$ GeV

measurements as the input for Au+Au 54.4 GeV collisions, and Au+Au 39 GeV for Au+Au 27 GeV collisions. The input pion v_2 is fitted with polynomial function at low p_T and linear function at high p_T. To take into account the potential energy dependence of light flavor hadrons elliptic flow between 62.4 and 54.4 GeV, we will use reconstructed electron v_2 for re-calibration. We combines both $\pi^\pm$ and π^0 measurements and then take the fitting function as the input v_2 for π^0. There is no measurement for η elliptic flow at low energies. Assuming that the η elliptic flow follows m_T scaling like π/K, we directly take K_s and $K^\pm$ flow measurements as replacement for the input of η elliptic flow. Because the rest mass for η and K is very close (Mass(η) = 547.86 MeV/c^2 and Mass(K)= 493.67 MeV/c^2 [10]). To obtain the elliptic flow of $\pi^0/\eta \to \gamma\gamma$, again, we decay π^0/η by PYTHIA, then set ϕ and p_T weight for daughter γ according their parent invariant yield and v_2. The input direct photon v_2 is from Au+Au 200 GeV measurements [129]. Fig. 3.28 shows input γ spectra from different sources, and Fig. 3.29 is v_2. At low p_T, γ dominantly comes from pseudo-scalar meson decay, while at high p_T direct photon makes the largest contribution. In this analysis, the low p_T region is more interested in this analysis.
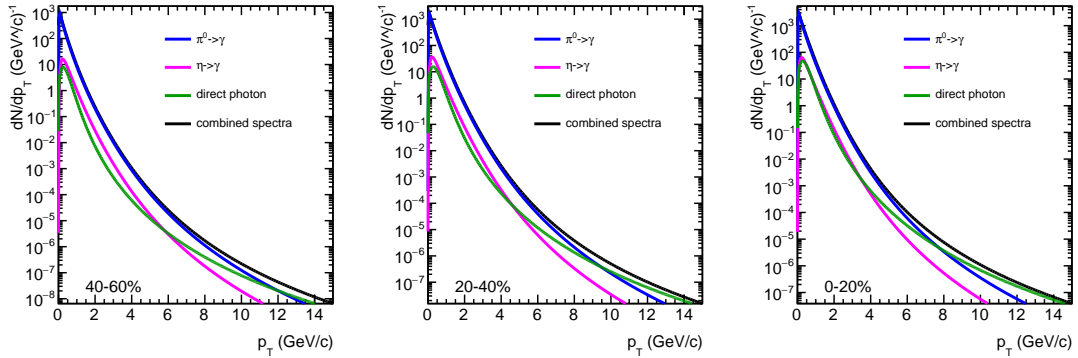
Fig. 3.28   Input γ spectra from different sources for Au+Au 54.4 GeV
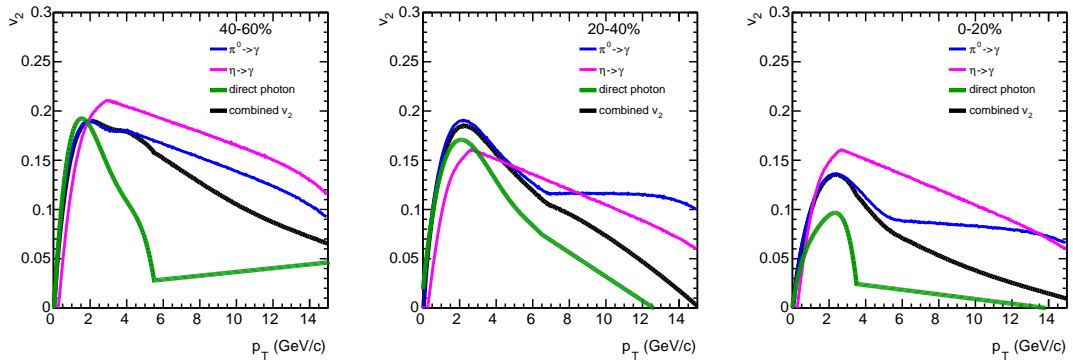
Fig. 3.29   Input γ v_2 from different sources for Au+Au 54.4 GeV

56

Due to the limit of statistics of embedding samples, the embedded $\pi^0/\eta/\gamma$ might have large fluctuation in ϕ direction before weighting, compared to the magnitude to the v_2, although they might have quite uniform distributions as function as p_T and η. Because the event plane angle is random, so if the statistic is high enough, $\Delta\phi = (\phi - \Phi_{EP})$ should be a uniform distribution regardless the geometry of the detector. To minimize statistic fluctuation in ϕ direction, we do a normalization and flatten the $\Delta\phi$ distribution of photonic electron tracks under fine p_T bin. Fig. 3.33 shows that after ϕ normalization, the statistic fluctuation of v_2 is much smaller.
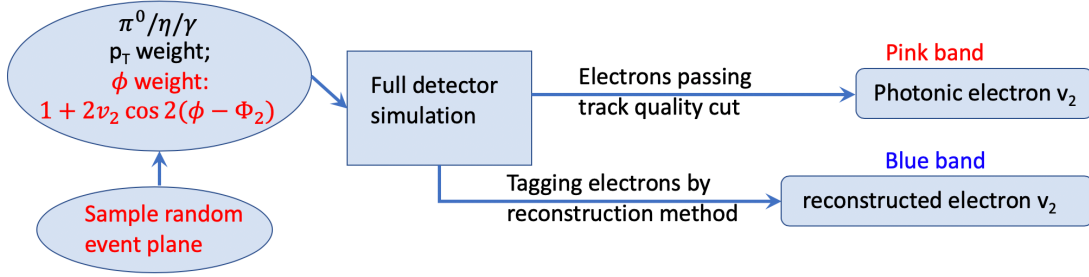
Fig. 3.30　Flow chart of photonic electron v_2 simulation.
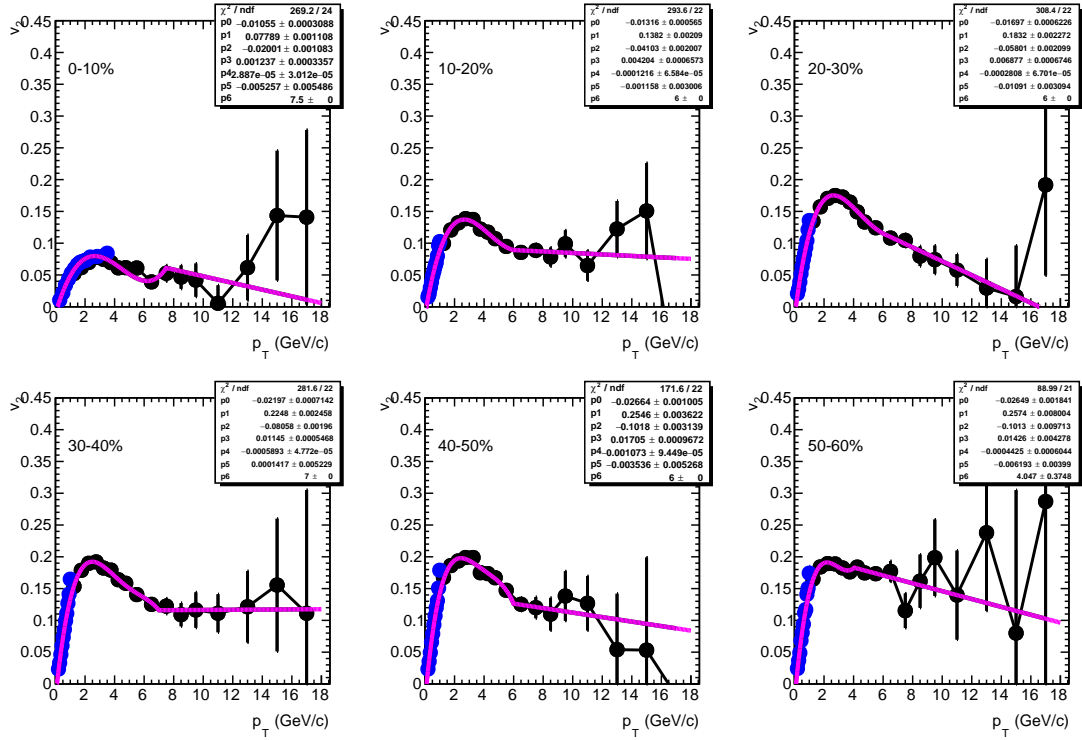
Fig. 3.31　Input pion v_2 for Au+Au 54 GeV.
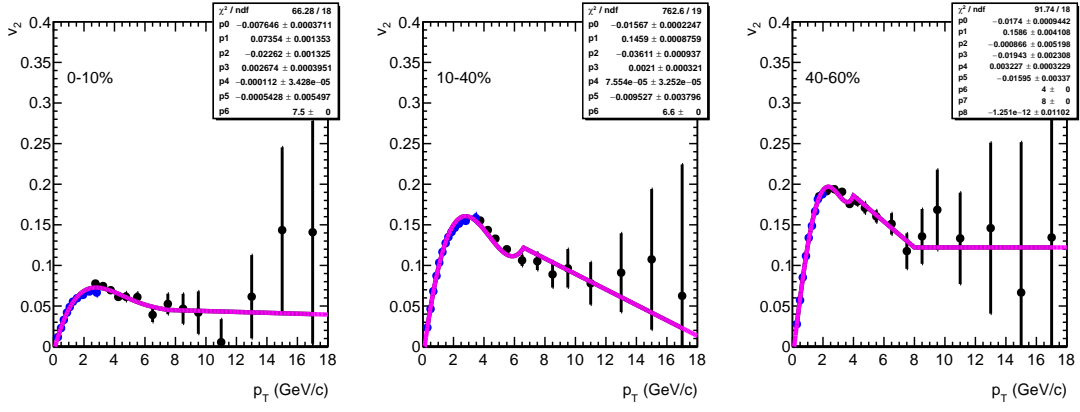
Fig. 3.32   Input pion v_2 for Au+Au 27 GeV.
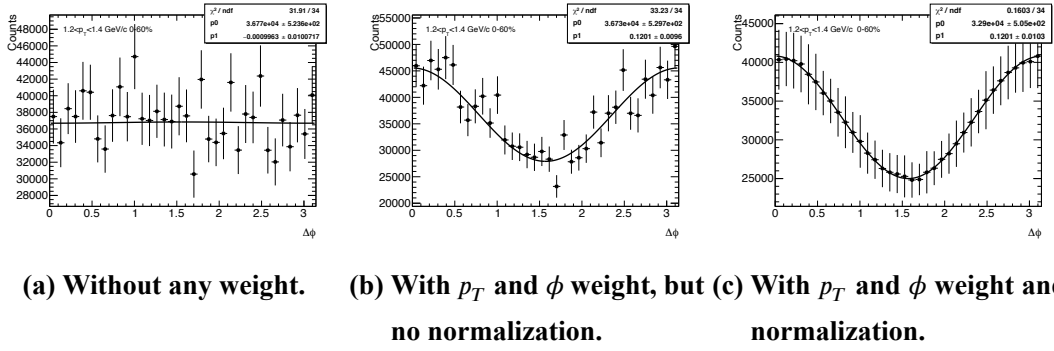
**(a) Without any weight.   (b) With p_T and ϕ weight, but   (c) With p_T and ϕ weight and
no normalization.   normalization.**

**Fig. 3.33   The $\Delta\phi$ distribution of photonic electron tracks in the embedding at $1.2 < p_T < 1.4$
GeV/c. Plot (a) shows raw $\Delta\phi$ distribution with no weight; Plot (b) is $\Delta\phi$ distribution
after p_T and ϕ weight; Plot (c) is after p_T and ϕ weight, and $\Delta\phi$ normalization. To
reflect the statistic fluctuation, the error bar shown in the Plot (c) is kept the same
as Plot (b).**

3.7.2   Systematic uncertainty of photonic electron v_2

To estimate the performance of photonic electron v_2, we compare reconstructed electron v_2 from both data and simulation as the reference. The reconstructed electron v_2 from real data is calculated by the following equation with event plane η-sub method:

$$N^{reco} \cdot v_2^{reco} = N^{UL} \cdot v_2^{UL} - N^{LS} \cdot v_2^{LS}$$
$$N^{reco} = N^{UL} - N^{LS} \tag{3.34}$$

$$\text{UL : unlike sign, LS : like sign}$$

As the input parent particle v_2 are from Au+Au 62.4 GeV measurements, so first we fit the reconstructed electron v_2 from embedding and get fitting function F^{reco}. Then multiply this function with a free parameter, $c \cdot F^{reco}$, to fit reconstructed electron v_2 from data and determine the scale factor c. Both reconstructed electron and photonic electron v_2 would be scaled with this factor in later on analysis. We use the simulated v_2 data

point instead of fitting function because it is easier to deal with wide p_T bin. The scale factor for 54.4 GeV is c=0.96, and for 27 GeV is c=0.93. The systematic uncertainty is estimated by calculating root mean square (RMS) of reconstructed electron v_2:

$$RMS = \sqrt{\frac{1}{N}\sum_N \left(\frac{v_2^{sim} - v_2^{data}}{v_2^{data}}\right)^2} \tag{3.35}$$

Where N is the number of points used in the systematic uncertainty estimation, while v_2^{sim} and v_2^{data} are reconstructed electron v_2 from simulation and data. The final total photonic electron v_2 is shown as the pink band in Fig. 3.34. The estimated systematic uncertainty of photonic electron v_2 is 3.0% for Au+Au 54 GeV and 3.7% for 27 GeV collisions.
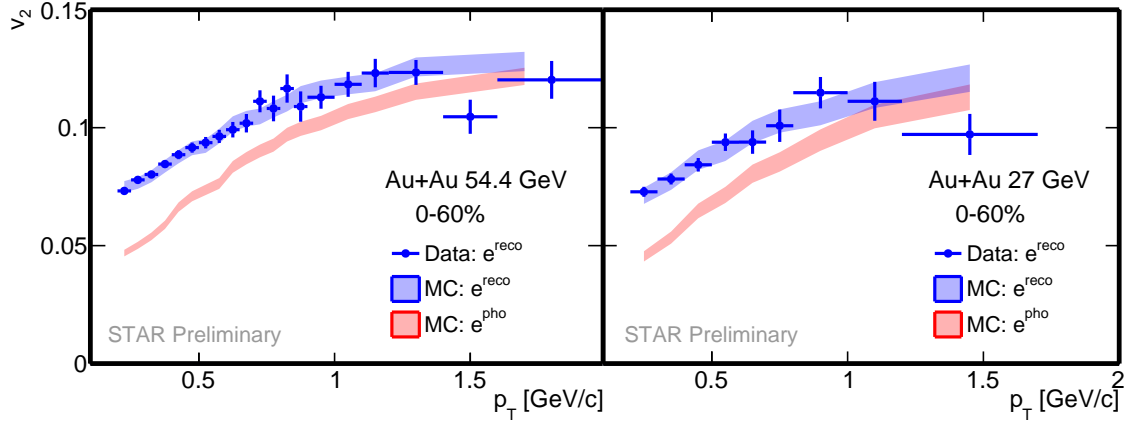
Fig. 3.34   Photonic electron v_2 from data and simulation. The pink bands refer to the total photonic electron v_2 from simulation. The blue bands and blue data points refer to the reconstruced electron v_2 from simulation and data.

3.8   Non-photonic electron v_2 and systematic uncertainty

To this step, every ingredient for NPE v_2 calculation has been obtained. The final result is calculated with following formula:

$$N^{HF}v_2^{HF} = N^{inc}v_2^{inc} - N^{pho}v_2^{pho} - \sum_h f_h \cdot N^{inc}v_2^h \tag{3.36}$$

Where f_h is the hadron contamination fraction obtained from purity fitting procedure. The hadron v_2 is using Au+Au 62.4 GeV STAR published result. The errors from each component are propagated according to error propagation law:

$$[\Delta f(x_1, ..., x_i)]^2 = \sum_{x_i}(\frac{\partial f}{\partial x_i})^2(\Delta x_i)^2 \tag{3.37}$$

Based on Eq. 3.36 and Eq. 3.37, Δv_2^{HF} can be written as:

$$
\begin{aligned}
(\Delta v_2^{HF})^2 &= \left(\frac{N^{inc}}{purity \cdot N^{inc} - N^{pho}} \right)^2 \times (\Delta v_2^{inc})_{stat}^2 \\
&+ \left[\frac{purity \cdot N^{pho} \cdot v_2^{pho} - (v_2^{inc} - \sum f \cdot v_2^h) \cdot N^{pho}}{(purity \cdot N^{inc} - N^{pho})^2} \right]^2 \times (\Delta N^{inc})_{stat}^2 \\
&+ \left[\frac{N^{inc} \cdot (v_2^{inc} - \sum ratio \cdot v_2^h) - purity \cdot N^{inc} \cdot v_2^{pho}}{(purity \cdot N^{inc} - N^{pho})^2} \right]^2 \times ((\Delta N^{pho})_{stat}^2 + (\Delta N^{pho})_{sys}^2) \\
&+ \left(\frac{N^{pho}}{purity \cdot N^{inc} - N^{pho}} \right)^2 \times (\Delta v_2^{pho})_{sys}^2
\end{aligned}
$$

$$(3.38)$$

Where ΔN^{pho} is uncertainty from the number of photonic electrons, which is calculated as:

$$
\begin{aligned}
N^{pho} &= \frac{N^{UL-LS}}{\epsilon_{reco}} \\
(\Delta N^{pho})_{stat}^2 &= N^{pho} \times \left[\left(\frac{(\Delta N^{UL-LS})_{stat}}{N^{UL-LS}} \right)^2 + \left(\frac{(\Delta \epsilon_{reco})_{stat}}{\epsilon_{reco}} \right)^2 \right] \\
(\Delta N^{pho})_{sys}^2 &= N^{pho} \times \left(\frac{(\Delta \epsilon_{reco})_{stat}}{\epsilon_{reco}} \right)^2
\end{aligned}
$$

$$(3.39)$$

In summary, we consider the following items for statistic uncertainty:

Δv_2^{inc}: inclusive electron v_2;

ΔN^{inc}: the number of inclusive electron, which can be ignored;

ΔN^{pho}: the number of photonic electron, including statistic uncertainty of reconstruction efficiency $\Delta \epsilon_{reco}$ from embedding and photonic electron signal extraction ΔN^{UL-LS}.

The following items would be taken into systematic uncertainty calculation:

Δv_2^{pho}: photonic electron v_2;

ϵ_{reco}: photonic electron reconstruction efficiency, which is contributed to ΔN^{pho}.

From Eq. 3.20 and 3.38, we can infer that $S/B = N^{HF}/N^{pho}$ will affect overall uncertainty. Smaller S/B will result in larger uncertainty. Fig. 3.35 reflect relative fraction of uncertainties from different sources in total uncertainty. In this analysis, systematic uncertainties from photonic electron v_2 makes largest contribution to the final results.

One may have noticed that uncertainties from electron purity is not transported in Eq. 3.38, because we need to consider hadron contamination too. We calculate final e^{HF} v_2 result with electron purity and hadron fraction gotten under different purity fitting methods, and take the largest difference compared to the default method as the
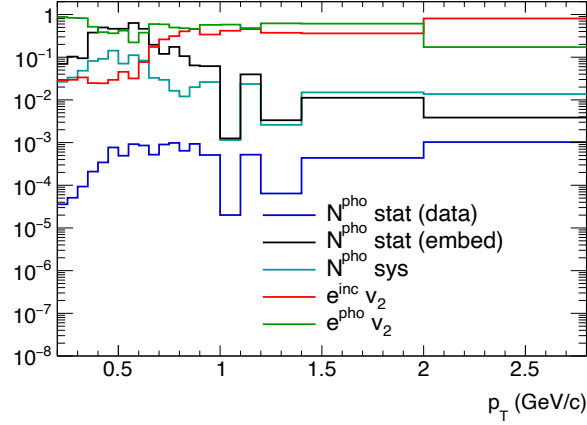
Fig. 3.35   Relative fraction of NPE v_2 uncertainty from different sources in Au+Au 54.4 GeV collisions. Y-axis represent $\Delta_i^2/\Delta_{total}^2$. Δ_{total}^2 includes both systematic and statistic uncertainty.

final systematic uncertainty. But as we have selected high electron purity region, purity uncertainty only makes small contribution to final result. Fig. 3.36 shows e^{HF} v_2 in Au+Au 27 and 54.4 GeV collisions.
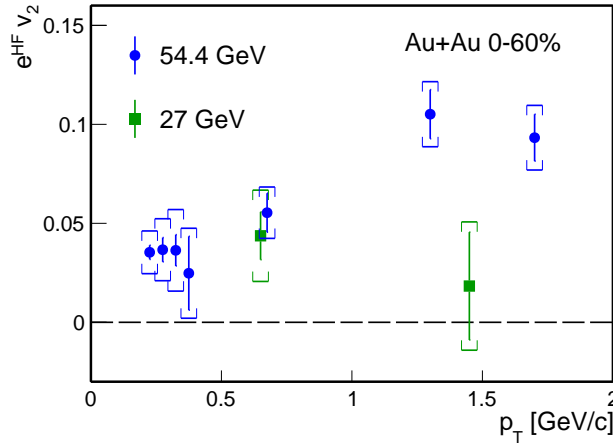
Fig. 3.36   NPE v_2 in Au+Au 27 and 54.4 GeV collisions.

3.9   Non-flow estimation

The non-flow contribution is estimated by PYTHIA8 [75] in this analysis. It has been tested in [75] that PYTHIA calculation will give similar non-flow estimation result as p+p data in 200 GeV collisions. The estimation is based on following assumption:

- Heavy flavor decay electrons are predominantly produced in the initial hard scattering processes, its yield scales with the number of binary nucleon-nucleon collisions.
- The shape of the correlation function of heavy flavor decay electrons and hadrons

61

are the same in Au+Au collisions and p+p collisions at the same collision energy. Two particle correlation method will be used for non-flow calculation. Following symbols will be used for the derivation:

N_e^{pp} - number of NPE in p+p event

N_h^{pp} - number of hadrons used in reference flow calculation in p+p (PYTHIA)

N_e^{AA} - number of NPE in Au+Au event

N_e^{AA} - number of hadrons used in reference flow calculation in Au+Au collisions

$v_2^{e,pp}$ - heavy flavor electron non-flow in p+p collisions

$v_2^{h,pp}$ - "reference flow" for p+p collisions

$v_2^{e,AA}$ - heavy flavor electron non-flow in Au+Au collisions

$v_2^{h,AA}$ - reference flow for Au+Au collisions

$\langle ... \rangle$ - this operator refers to taking the average over all events

Suppose the number of heavy flavor electrons have no correlation with event multiplicity, then we can take the approximation:

$$\left\langle N_e^{pp} N_h^{pp} \right\rangle \simeq \left\langle N_e^{pp} \right\rangle \left\langle N_h^{pp} \right\rangle$$
$$\left\langle N_e^{AA} N_h^{AA} \right\rangle \simeq \left\langle N_e^{AA} \right\rangle \left\langle N_h^{AA} \right\rangle$$

Two particle moment in p+p collisions is calculated as:

$$
\begin{aligned}
M_2^{pp} = v_2^{e,pp} v_2^{h,pp} &= \left\langle \left\langle \cos\left[2(\phi_e - \phi_h) \right] \right\rangle \right\rangle \\
&= \left\langle \frac{\sum_e^{N_e^{pp}} \sum_h^{N_h^{pp}} \cos[2(\phi_e - \phi_h)]}{N_e^{pp} N_h^{pp}} \right\rangle \\
&\simeq \frac{\left\langle \sum_e^{N_e^{pp}} \sum_h^{N_h^{pp}} \cos[2(\phi_e - \phi_h)] \right\rangle}{\left\langle N_e^{pp} \right\rangle \left\langle N_h^{pp} \right\rangle}
\end{aligned}
\tag{3.40}
$$

Two particle moment in Au+Au collisions is calculated as:

$$
\begin{aligned}
M_2^{AA} = v_2^{e,AA} v_2^{h,AA} &= \left\langle \left\langle \cos\left[2(\phi_e - \phi_h) \right] \right\rangle \right\rangle \\
&= \left\langle \frac{\sum_e^{N_e^{AA}} \sum_h^{N_h^{AA}} \cos[2(\phi_e - \phi_h)]}{N_e^{AA} N_h^{AA}} \right\rangle \\
&\simeq \frac{\left\langle \sum_e^{N_e^{AA}} \sum_h^{N_h^{AA}} \cos[2(\phi_e - \phi_h)] \right\rangle}{\left\langle N_e^{AA} \right\rangle \left\langle N_h^{AA} \right\rangle}
\end{aligned}
\tag{3.41}
$$

Based on the assumption, only heavy flavor di-jet and other heavy flavor hadron daughters make non-zero contribution to the M_2. The contributions from di-jet and heavy flavor hadrons can be approximated by scaling the correlation from PYTHIA by number

of binary collisions. Then

$$\left\langle \sum_e^{N_e^{AA}} \sum_h^{N_h^{AA}} \cos[2(\phi_e - \phi_h)] \right\rangle = N_{bin} \left\langle \sum_e^{N_e^{pp}} \sum_h^{N_h^{pp}} \cos[2(\phi_e - \phi_h)] \right\rangle \quad (3.42)$$

$$N_e^{AA} = N_{bin} N_e^{pp} \quad (3.43)$$

$$
\begin{aligned}
M_2^{AA} &= v_2^{e,AA} v_2^{h,AA} \\
&\simeq \frac{N_{bin} \left\langle \sum_e^{N_e^{pp}} \sum_h^{N_h^{pp}} \cos[2(\phi_e - \phi_h)] \right\rangle}{\left\langle N_{bin} N_e^{pp} \right\rangle \left\langle N_h^{AA} \right\rangle} \\
&\simeq \frac{\left\langle \sum_e^{N_e^{pp}} \sum_h^{N_h^{pp}} \cos[2(\phi_e - \phi_h)] \right\rangle}{\left\langle N_e^{pp} \right\rangle \left\langle N_h^{pp} \right\rangle} \frac{\left\langle N_h^{pp} \right\rangle}{\left\langle N_h^{AA} \right\rangle} 37 \\
&\simeq M_2^{pp} \frac{\left\langle N_h^{pp} \right\rangle}{\left\langle N_h^{AA} \right\rangle}
\end{aligned}
\quad (3.44)
$$

So the final estimated non-flow can be written as:

$$v_2^{AA} = \frac{M_2^{pp}}{v_2^{h,AA}} \frac{\left\langle N_h^{pp} \right\rangle}{\left\langle N_h^{AA} \right\rangle} \quad (3.45)$$

This is a conservative estimation for the upper limit of non-flow contribution, because such jet-like correlation might be weakened in Au+Au collisions due to jet quenching in QGP. Especially the correlation between heavy flavor electron and the particles produced in the away side direction, whose phi angles satisfy $|\phi^{track} - \phi^e| > 90°$, could be totally uncorrelated due to the multi-scattering inside the QGP medium. So for lower limit estimation for non-flow contribution, we suppose away side particles have no correlation with heavy flavor electrons, and only take near side hadrons into account for reference flow calculation.

The cuts for charged hadrons used in reference flow calculation in PYTHIA is the same as what we used for event plane reconstruction in inclusive electron v_2 calculation: $0.2 < p_T < 2$ GeV/c, $|\eta| < 1$, η gap=0.05. In Eq. 3.45, $v_2^{h,AA} = 0.046$ and $\left\langle N_2^{AA} \right\rangle = 122$, which is the mean v_2 for charged hadrons and average track number used for event plane calculation in 0-60%. Note that, we only take half η range for event plane reconstruction: $0.05 < \eta < 1$ or $-1 < \eta < -0.05$.

Fig. 3.37 shows the estimated non-flow in Au+Au 54.4 GeV collisions. In this plot, We use charged hadrons in full $\Delta\phi$ range for reference flow calculation to estimate the upper limit of non-flow contribution. While for lower limit, we use only near side

hadrons. The overall non-flow contribution in Au+Au 54.4 GeV is a bit lower than 200 GeV collisions.
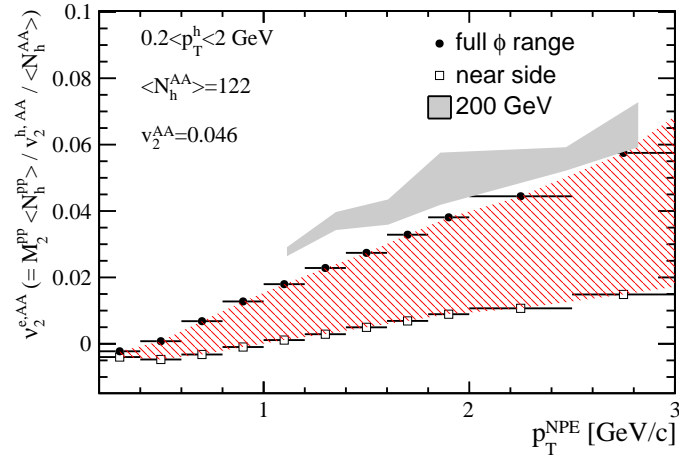
Fig. 3.37   Estimated non-flow in Au+Au 54 GeV. "full ϕ range" gives the upper limit of non flow contribution.

3.10   Appendix

Below are the selected QA plots for photonic electron embedding.
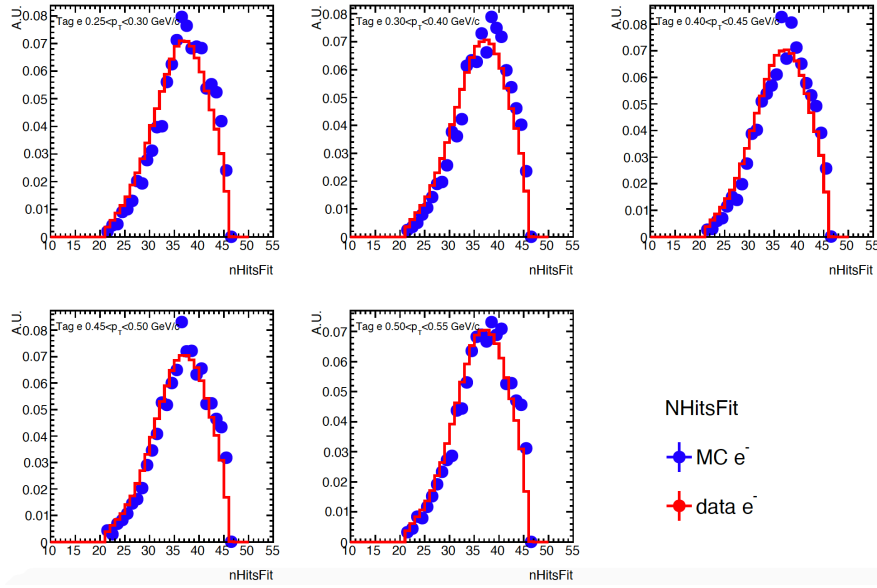
Fig. 3.38   Partner electron nHitsFit versus tagged electron p_T. Blue point: MC; Red line: Data.
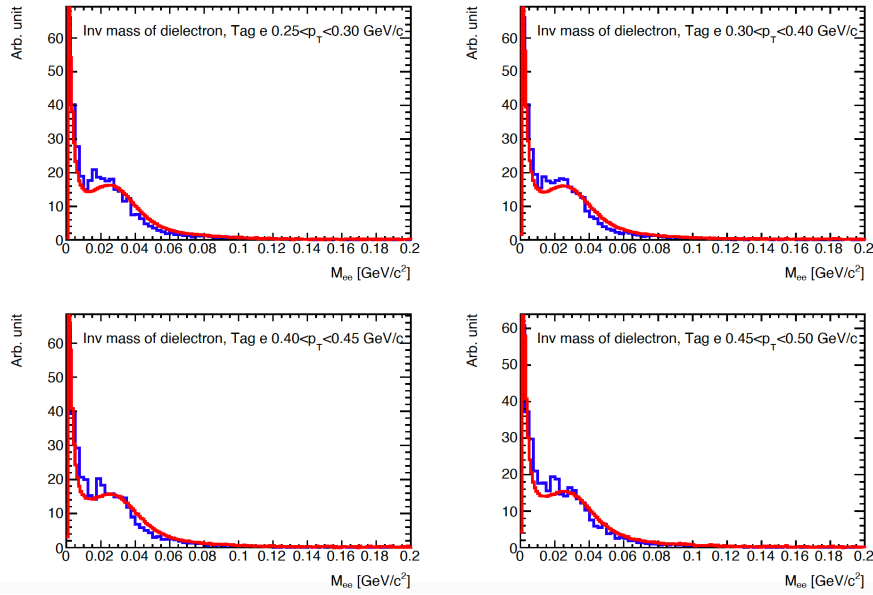
Fig. 3.39   Electron pair invariant mass distribution in different tagged electron p_T bin. Blue line: MC; Red line: Data.
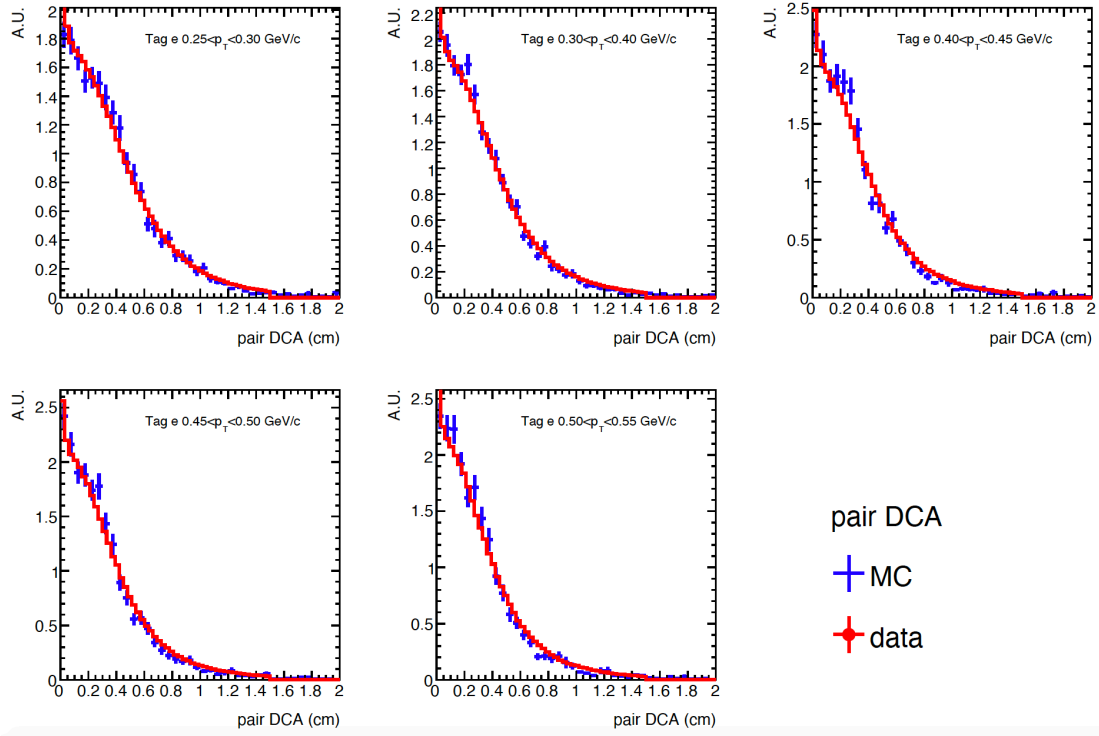
Fig. 3.40   **Electron pair DCA distribution in different tagged electron p_T bin. Blue point: MC; Red line: Data.**
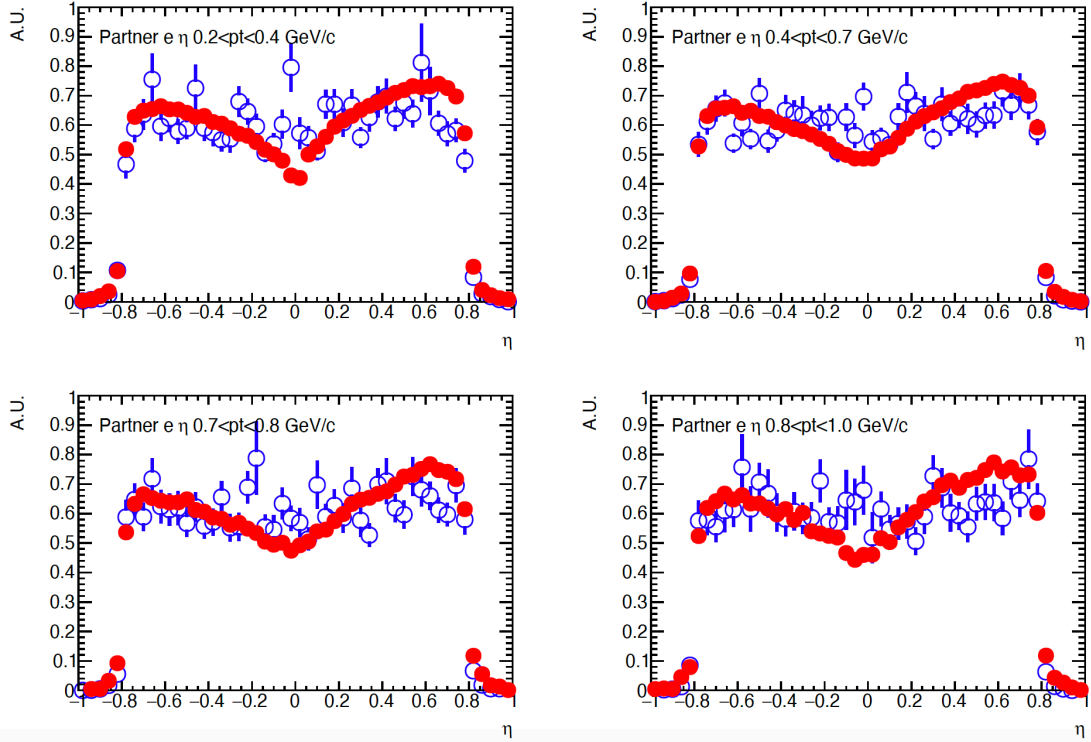
Fig. 3.41   **Partner electron η distribution in different tagged electron p_T bin. Blue open circle: MC; Red close circle: Data.**

Chapter 4 Measurements of D^{*+} production in Au+Au 200 GeV collisions

In this chapter, we will discuss measurements of D^{*+} production. The data samples are collected by STAR with Heavy Flavor Tracker (HFT) detector installed during 2014-2016. With HFT detector, secondary vertex of charm hadrons can be reconstructed precisely. D^{*+} meson is reconstructed via $D^{*+} \to D^0 \pi_s^+$ (67.7%), $D^0 \to K^- \pi^+$ (3.89%) and its charge conjugate channel. D^{*+} reconstruction, efficiency correction and systematic uncertainty estimation will be discussed.

4.1 Data Sets and Event selection

In this analysis, we will use Au+Au $\sqrt{s_{NN}} = 200$ GeV Minbias triggered data collected during RHIC run year 2014 and 2016. The statistics are listed in Table 4.1. Trigger Id are listed below:

Year	Statistics used	library
2014	860M	P16id
2016	1B	P16ij

Table 4.1 Statistics and events number in this analysis

- Run2014: 450050, 450060, 450005, 450015, 450025
- Run2016: 520001, 520011, 520021, 520031, 520041, 520051

The vertex cuts for bad event rejection are summarized below:

- $V_R = \sqrt{V_x^2 + V_y^2} < 2$ **cm.** To match the HFT geometry, a smaller beam pipe is used. Beam pipe radius is 2 cm during 2014-2016.

- $|V_z| < 6$ **cm.** The HFT detector is 20 cm long in Z-axis. This is to ensure that collisions happen in the center of HFT with $|\eta| < 1$.

- $|V_z - V_z^{vpd}| < 3$ **cm**. Because TPC is a slow detector, primary vertex reconstructed by TPC tracks might come from different collisions when pile-up happens. This cut is to reduce pile-up events.

- $|V_x, V_y, V_z| > 10^{-5}$ **cm.** Require the events have valid vertex information.

4.2 D^0 reconstruction

D^0 ($\overline{D^0}$) are reconstructed through the $K\pi$ decay channel with help of the HFT. The method is the same as the STAR published D^0 measurements [83].

4.2.1   Track selection and particle identification

We use global tracks and require them to have HFT hits to ensure good pointing resolution. Spatial resolution is much more precise after HFT detector is added into the track reconstruction process. To increase particle identification (PID) efficiency, hybrid method is used. When the track is matched to valid TOF hit, a combination of TPC dE/dx and TOF $1/\beta$ measurements is used for particle identification; otherwise, only TPC dE/dx information is used. Track quality cuts and PID cuts are summarized below:

Track quality for π and K:

- global tracks;
- $p_T > 0.3$ GeV/c
- $|\eta| < 1$
- nHitsFit>= 20 (only TPC hits, not include HFT hits)
- at least one hit in every layer of PXL and IST

Pion PID cuts:

- $|n\sigma_\pi| < 3$
  if TOF is available: $|\frac{1}{\beta_{th}} - \frac{1}{\beta_{exp}}| < 0.03$

Kaon PID cuts:

- $|n\sigma_K| < 2.0$
  if TOF is available: $|\frac{1}{\beta_{th}} - \frac{1}{\beta_{exp}}| < 0.03$

D^0 daughters Distance of Closet approach (DCA) to primary vertex, as one of the topological parameters, will be discussed in the following section.

4.2.2 D^0 decay topology

Thanks to the excellent DCA resolution provided by HFT detector, D^0 are able to be identified by its decay topology although its life time is short ($c\tau \simeq 123\mu m$). Fig. 4.1 shows the D^0 decay diagram via $D^0 \to K^-\pi^+$. Several topological variables are used to characterize the candidate $K\pi$ pair topology:

- DCA_K and DCA_π: DCA of K/π to the primary vertex.
- DCA_{12}: The closet distance between two daughter tracks.
- DecayLength: The distance between reconstructed D^0 decay vertex and primary
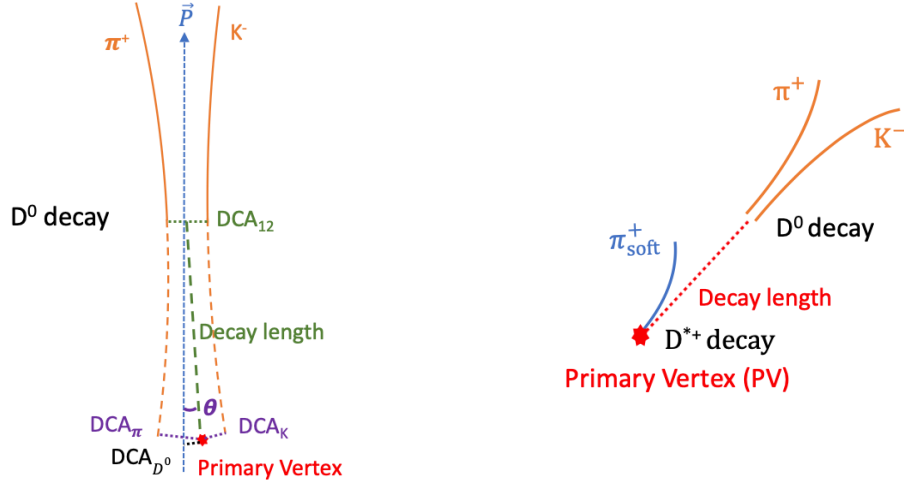
Fig. 4.1   **The schematic diagram of D^0 (left) and D^{*+} (right) decay topology.**

Table 4.2 D^0 topological cuts in Run14

D^0 p_T (GeV/c)	0-1	1-2	2-3	3-5	5-10
$DCA_\pi(\mu m) >$	110	111	86	81	62
$DCA_K(\mu m) >$	103	91	95	79	58
$DCA_{12}(\mu m) <$	84	66	57	50	60
Decay length (μm) >	145	181	212	247	259
$DCA_{D^0}(\mu m) <$	61	49	38	38	40

vertex. D^0 decay vertex position is defined as the middle point of the DCA position of two daugher tracks where the two tracks are closet to each other.

- DCA_{D^0}: DCA of reconstructed D^0 track to the primary vertex.
- $\cos\theta$: θ is the angle between the direction of primary vertex pointing to the decay vertex and the direction of reconstructed D^0 momentum. $\cos\theta$ can be calculated by $\sin\theta = DCA_{D^0}/DecayLength$ and $\cos\theta = \sqrt{1 - \sin\theta^2}$.

The rest of D^0 topological cuts are tuned with "Rectangle cuts" method utilizing Toolkit for Multivariant Analysis (TMVA) package in each centrality and p_T bin[83]. D^0 topological cuts used for Run14 and Run16 are listed in Table 4.2 [130] and Table 4.3 [131]. Fig. 4.2 shows the reconstructed D^0 signal at $2<p_T<10$ GeV/c in 0-80% centrality. The combinatorial background is reconstructed by mixed-event method. The scaling factor for mixed-event Unlike-Sign is calculated by taking the ratio between the integrated counts of same-event Like-Sign and that of mixed-event Like-Sign within $0.152<\Delta M<0.175$ GeV/c^2. In Fig. 4.2, red data points are the D^0 signal

Table 4.3 D^0 topological cuts in 0-10% centrality in Run16

$D^0 p_T (GeV/c)$	0-0.5	0.5-1	1-2	2-3	3-5	5-10
$DCA_\pi (\mu m) >$	133	105	93	97	67	55
$DCA_K (\mu m) >$	138	109	82	94	76	54
$DCA_{12} (\mu m) <$	71	64	70	63	82	80
Decay length $(\mu m) >$	100	199	227	232	236	255
$DCA_{D^0} (\mu m) <$	62	55	40	40	40	44
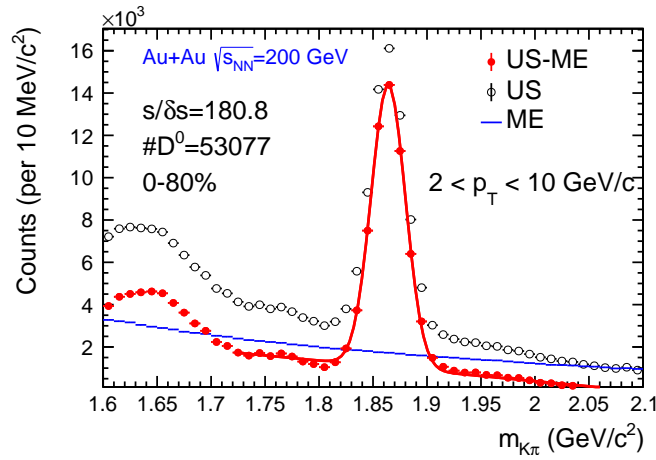
Fig. 4.2   The invariant mass distribution of $K\pi$ pair in 2<p_T<10 GeV/c at 0-80% centrality in Run14. The black open circles represent the Unlike-Sign (US) distribution. The combinatorial background distribution is estimated by Mixed-Event method, shown as the blue histogram. The red full circles depict US distribution after combinatorial background subtracted.

after combinatorial background subtraction. The "bump" structure in D^0 signal around $1.6 < m_{K\pi} < 1.7$ GeV/c^2, are the correlated backgrounds mainly from the partial reconstruction of multi-prong decays, , for example $D^0 \to K^- \rho^+ \to K^- \pi^+ + \pi^0$ (B.R. = 0.108), or jet fragments.

4.3 D^{*+} reconstruction

We pair D^0 candidate with "soft" pion tracks. D^0 signals are fitted with Gaussian function and D^0 candidates are selected within $m_{K\pi} \pm 3\sigma$, where $m_{K\pi}$ is the mean value of Gaussian fit. Fig. 4.4 shows D^{*+} p_T distribution versus its daughter π_{soft} from simulation. In the simulation, D^{*+} is forced to decay to $D^0 \pi$ by PYTHIA. The input p_T distribution for D^{*+} uses D^0 spectra in Au+Au 200 GeV collisions [83]. The momentum

of soft pion is $<\sim$ 0.1 of the momentum of its parent D^{*+} due to the small decay Q-value, so we call it soft pion or slow pion. In this analysis, soft pion p_T is $\in$ [0.15, 1.2) GeV/c. We set a loose cut on the soft pion and do not require it to be a "HFT track" to increase efficiency.

Soft pion:

- nHitsFit>=20
- p_T > 0.15 GeV/c
- gDCA<3 cm
- $|n\sigma_\pi| < 3$
- If TOF available:

  if PtBin[i]<p_T<PtBin[i+1] GeV, LowEdge[i]<$\frac{1}{\beta_{th}} - \frac{1}{\beta_{exp}}$<HighEdge[i]

  double PtBin[6]={0.15,0.2,0.25,0.3,0.35,10};

  float LowEdge[6] = {-0.03,-0.03,-0.03,-0.03,-0.03};

  float HighEdge[6] = {0.85,0.05,0.04,0.035,0.03};

  The particle 1/β distribution is shown in Fig. 4.3.
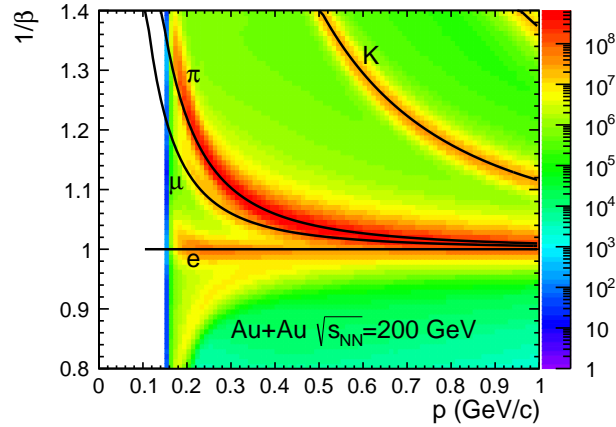
Fig. 4.3 **1/β versus momentum in Run16. The lines in the plot are expected 1/β values for each particles respectively.**

To minimize the contribution from D^0 mass resolution, we calculate $m_{K\pi\pi} - m_{K\pi}$ to get D^{*+} signal. Figure 1.6 shows the $m_{K\pi\pi} - m_{K\pi}$ distribution, a clear narrow peak aroung the $m_{D^{*+}} - m_{D^0}$ is seen. The σ of the peak is found to about 0.75 MeV/c^2. The backgrounds shown in Fig. 4.6 are reconstructed from three different methods:

- **Wrong sign method**: Suppose π^+ and π^- have similar distribution. Similar as like-sign method, we pair $D^0\pi_s^-$($K^-\pi^+\pi_s^-$) and charge conjugate to describe the combinatorial background, shown as the magenta cross in Fig. 4.6. Wrong sign method can well describe the background at $m_{K\pi\pi} > 0.15$ GeV/c^2 and $m_{K\pi\pi} <$
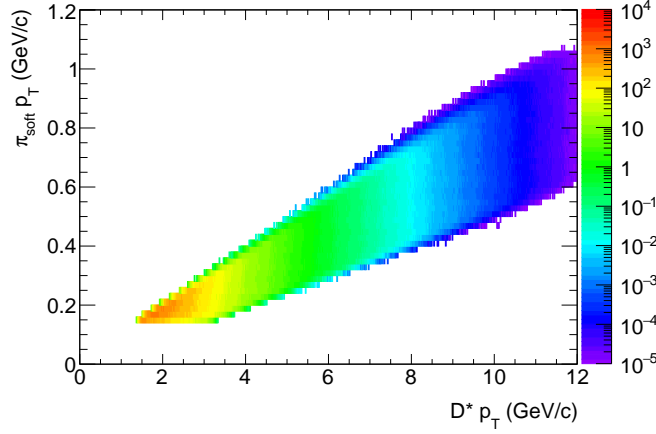
Fig. 4.4 D^{*+} **momentum versus its daughter** π_{soft} **from simulation.** D^{*+} **is forced to decay to** $D^0\pi$ **by PYTHIA. The input** p_T **distribution for** D^{*+} **uses** D^0 **spectra in Au+Au 200 GeV collisions [83].**
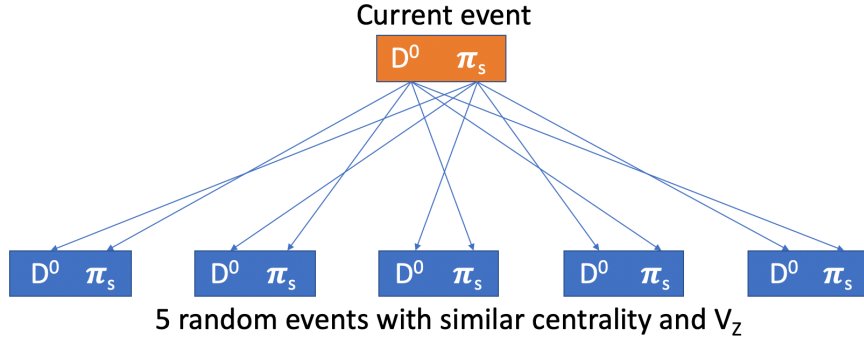
Fig. 4.5 **Current event are mixed with 5 similar property events.**

0.142 GeV/c^2. However, there is a bump structure under the D^* signal peak due to mis-PID. $D^0(K^-\pi^+)$ could be misidentified as $\overline{D^0}(\pi^-K^+)$ due to the mis-identification of both kaon and pion tracks. So D^{*+} wrong-sign background also contains D^{*+} signal, although the mass distribution is distorted.

- **Side band method**: Suppose the background $K^-\pi^+$ pair have similar distribution in side band region $2\sigma < |m_{K\pi}-m_{D^0}| < 4\sigma$ and the peak region $|m_{K\pi}-m_{D^0}| < 2\sigma$. Then we pair side band $K\pi$ with soft pion to describe the shape of D^* combinatorial background. Because the topological cuts largely suppress the combinatorial background of D^0, the Side Band background for D^{*+} is lower than the real background. We scale the Side Band background to match the real background.

- **Mixed-event method**: Suppose the particle distributions are similar in events with similar collision environment. So the uncorrelated background can be reconstructed by pairing particles in current event with those in other similar events, as is demonstrated in Fig. 4.5. In this analysis, the events are classified according to the collision centrality and the position of primary vertex along the beam-line.
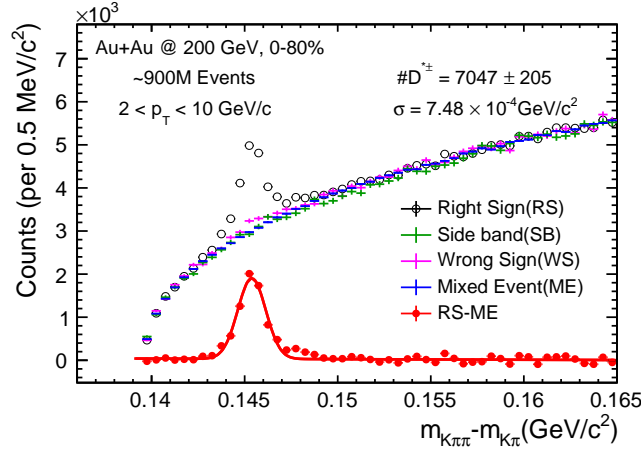
Fig. 4.6   The invariant mass distribution of $m_{K\pi\pi} - m_{K\pi}$ in 2<p_T<10 GeV/c at 0-80% centrality in Run 14. The open circles represent Right-Sign distribution. The green, magenta, and blue crosses represent the combinatorial background distribution estimated by Side-Band (SB), Wrong-Sign (WS), and Mixed-Event (ME) method. The red solid circles are RS distribution with combinatorial background subtracted using MS background.

The events are classified into 9 centrality bins and 10 V_z bins. Only events within the same centrality and V_z bins will be mixed. We also require the events have at least one D^0 candidate. By mixing current event with 5 random events with similar properties, we are able to reconstruct background with about 8-9 times statistics. The scale factor is calculated by taking the ratio of integrated counts within $0.152 < m_{K\pi\pi} - m_{K\pi} < 0.175$ GeV/c^2 between Mixed Event method and the real background.

From above discussions, Mixed-Event method is the best choice for background reconstruction. The red data points in Fig. 4.2 are the D^{*+} signal after mixed-event background subtraction. The signal is fitted with a Gaussian function for the D^{*+} signal plus a linear function for the residual background:

$$f = C \cdot Gaus(\mu, \sigma) + k \cdot x + b \tag{4.1}$$

4.4 D^* efficiency correction

D^{*+} efficiency is factorized as the product of D^0 reconstruction efficiency and single π_s efficiency.

4.4.1　π_s efficiency

The single π_s efficiency includes TPC tracking efficiency and PID efficiency. PID efficiency includes TPC and TOF PID cut efficiency, and TOF matching efficiency.
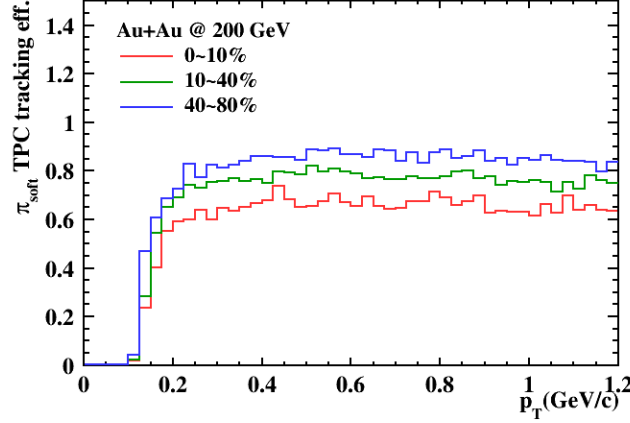
Fig. 4.7　TPC tracking efficiency of π_s as a function of p_T in different centrality bins in Run14.

TPC tracking efficiency is evaluated by STAR standard embedding method. The TPC tracking efficiency is affected by the detector acceptance, TPC response and event multiplicity. The Monte Carlo tracks are generated and processed through the STAR detector material via GEANT3 simulation. The simulated events are embedded into real events and then processed through track reconstruction procedure along with real tracks in the events. The real data samples are randomly selected from full minimum bias events. The number of embedded pion tracks are constrained to about 5% multiplicity of the event to avoid disturbing original tracking efficiency due to the increased occupancy. TPC tracking efficiency is calculated as:

$$\epsilon_{TPC} = \frac{N_{RC} \, (\text{nHitsFit} \geqslant 20 \, \& \, |\eta| < 1 \, \& \, gDCA < 3 \, \& \, \text{nCommonHits} > 10)}{N_{MC}} \quad (4.2)$$

Where RC refers to reconstructed tracks, and MC is Monte Carlo tracks. Because we will fold the pion efficiency into D^{*+} efficiency calculation so the soft pion TPC tracking efficiency is calculated as function as MC p_T, shown in Fig. 4.7.

TOF matching efficiency is evaluated from real data. We select pion samples by TPC $|n\sigma_\pi| < 2$ and estimate the fraction of pions that have valid TOF information. π_s TOF matching efficiency under different centralities is shown in Fig. 4.8.

$$\epsilon_{TOF} = \frac{N_\pi \, (\text{pass track quality cut} \, \& \, \beta > 0)}{N_\pi(\text{pass track quality cut})} \quad (4.3)$$

Efficiency loss caused by PID cuts are evaluated by studying $n\sigma$ and $1/\beta$ distribution of pure particle samples. For TPC PID ($n\sigma_\pi$) efficiency study, pion samples are selected
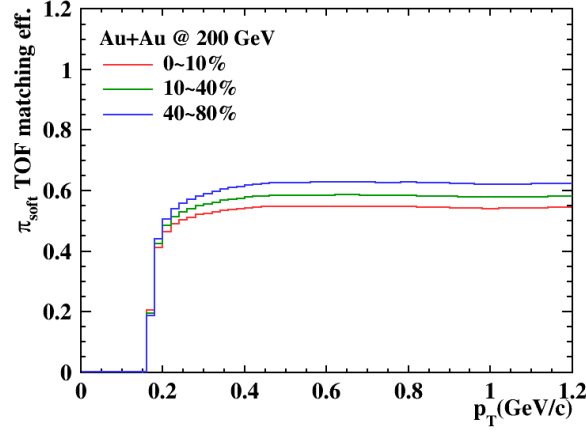
Fig. 4.8   TOF matching efficiency of π_s as a function of p_T in different centrality bins in Run14.
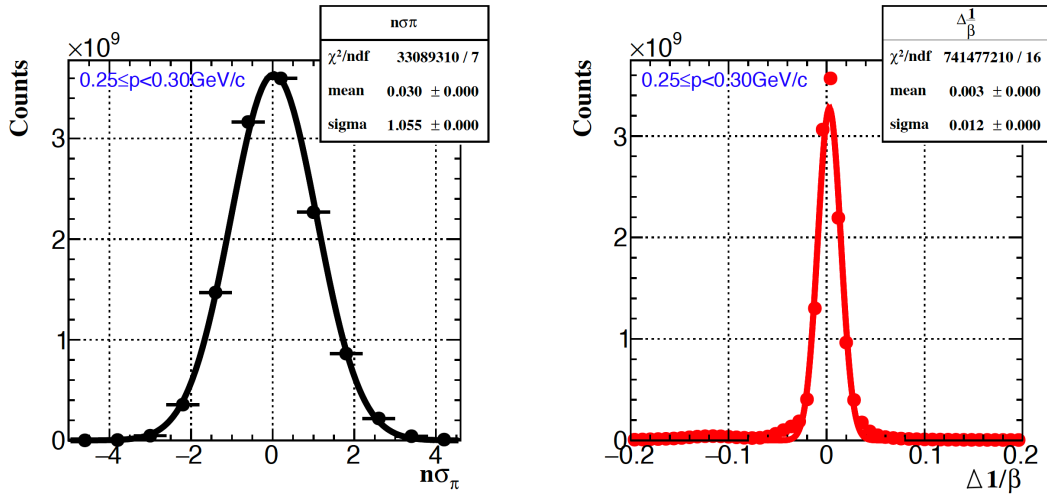
Fig. 4.9   Left: $n\sigma_\pi$ distribution; Right: $1/\beta$ distribution.

by reconstructing $K_s \to \pi\pi$. The $n\sigma_\pi$ distribution is well described by Gaussian function. TPC PID cut efficiency is calculated as:

$$\epsilon_{n\sigma_\pi} = \frac{\text{Integral}(-3, 3) + 1}{\text{Integral}(-5, 5) + 2} \tag{4.4}$$

The integrations in Eq. 4.4 are calculated from fitting functions.

For TOF PID, pion samples can be selected by TPC dE/dx, or by reconstructing $K_s \to \pi\pi$. We set a loose TOF PID cut at $p_T < 0.2$ GeV/c due to TOF calibration shift (Fig. 4.4). Because of the long life time of K_s ($c\tau \simeq 2.68$ cm/c), daughter pions' measured flight time from TOF might larger than their real fight time at low p_T. As the TOF PID cut is very loose, after cross-check with TPC selected pion samples, this effect is negligible compared to our PID cuts. Because $\Delta\frac{1}{\beta}$ distribution is not a perfect Gaussian (Fig. 4.9), so bin counting method will be used instead of Gaussian fit. Pion
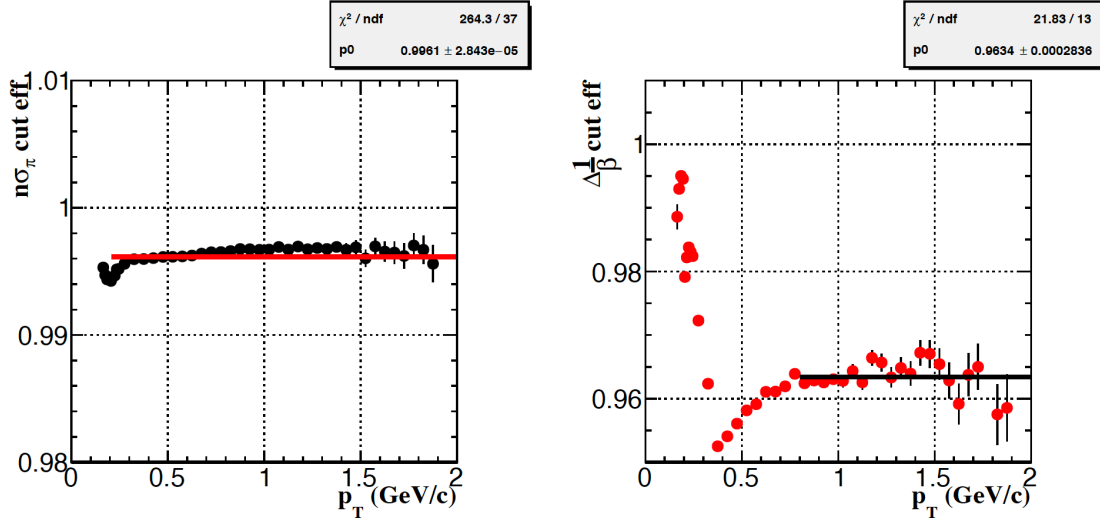
Fig. 4.10   Left: π_s TPC PID cut efficiency; Right: π_s TOF PID efficiency.

samples selected by TPC is not pure enough for bin counting, so we will use pion from K_s for TOF PID cut efficiency calculation.

The PID cut efficiency in Run16 is shown in Fig. 4.10. As hybrid PID is used, the total PID efficiency is then calculated as:

$$\epsilon_{PID} = \epsilon_{n\sigma_\pi} \cdot \epsilon_{TOF} \cdot \epsilon_{\Delta\frac{1}{\beta}} + \epsilon_{n\sigma_\pi} \cdot (1 - \epsilon_{TOF}) \tag{4.5}$$

4.4.2 D^0 reconstruction efficiency

According to Bayes' theorem, the possibility of event A and B happen simultaneously can be described as:

$$P(A\&B) = P(A) \cdot P(B|A) \tag{4.6}$$

Where P(A) refers to event A happening possibility, and P(B|A) refer to the possibility of happening event B when event A happens. Then D^0 efficiency can be described as the convolution of different sources:

$$\epsilon_{D^0}^{reco} = \epsilon_{Accept} \otimes \epsilon_{Track} \otimes \epsilon_{Topo} \tag{4.7}$$

$$\epsilon_{Track} = \epsilon_{TPC} \otimes \epsilon_{HFT} \otimes \epsilon_{PID} \tag{4.8}$$

where

- ϵ_{Accept} denotes efficiency of the detector acceptance cut, such as rapidity, p_T cut on tracks.

- ϵ_{Track} refers to the efficiency of single track selection, such as TPC tracking efficiency ϵ_{TPC}, HFT matching efficiency ϵ_{HFT}, and particle identification ϵ_{PID},

as shown in Eq. 4.8. Similar as π_s efficiency, TPC tracking efficiency is obtained from full detector simulation without requiring HFT response (so called embedding method). PID efficiency of single particle includes TOF matching efficiency, TPC $n\sigma$ and TOF $\Delta\frac{1}{\beta}$ cut efficiency (Eq. 4.5). π and K pure samples are selected from K_s and ϕ reconstruction. HFT matching efficiency is the possibility of qualified TPC tracks (e.g. K/π) having hits on all layers of HFT detector (see section 4.2.1):

$$\epsilon_{HFT} = \frac{N(\text{pass TPC track QA \& pass PID cut \& match HFT QA})}{N(\text{pass TPC track QA \& pass PID cut})} \quad (4.9)$$

HFT matching efficiency has p_T, centrality, particle species dependence.

- ϵ_{Topo} is the efficiency of topological cuts on $K\pi$ pair, as demonstrated in Fig. 4.1. K/π track should be qualified TPC track and meet HFT hit requirements.
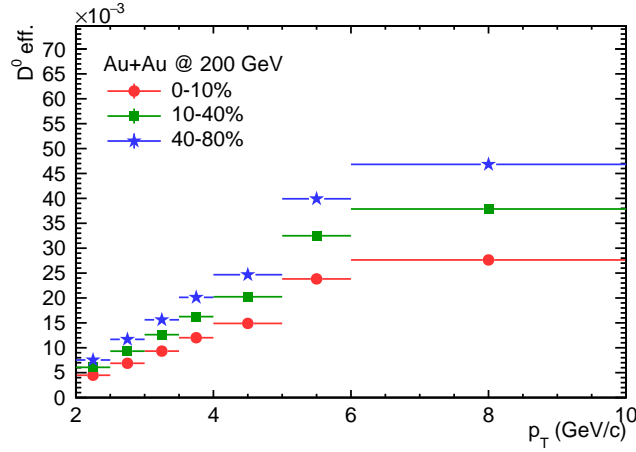
Fig. 4.11 D^0 **reconstruction efficiency as a function of** p_T **in centrality bin of 0-10%, 10-40% and 40-80%.**

In this analysis, the data-driven fast simulation approach will be used to evaluate D^0 efficiency. In the preparation step, we extract the detector response on single tracks. The track spatial resolution is described with global DCA distribution of identified particles. Here assuming the detector DCA resolution of secondary particles decayed from very short life particles are the same as that of primary particles. The 2D distribution of DCA_{XY} versus DCA_Z can better reflect the data than one dimension in order to take into account the correlation between the two. The momentum smearing of the reconstructed track is described by momentum resolution R^{Mom}:

$$R^{Mom} = \frac{p_T^{MC} - p_T^{RC}}{p_T^{MC}} \quad (4.10)$$

Where p_T^{MC} is MC p_T and p_T^{RC} is reconstructed p_T. Momentum resolution of K/π is calculated from embedding. In the simulation, D^0 is decayed by PYTHIA. We also

consider the collision vertex distribution in beam direction (V_Z). Then the detector response is applied to D^0 daughter tracks. The detailed procedures are shown below:

1. Sample V_z distribution according to that in real data.

2. Sample D^0 kinematics. The D^0 is sampled with uniform p_T, ϕ and rapidity distribution. Then p_T weight is set for D^0 according to published D^0 spectra in p+p, which is to ensure that p_T distribution shape is close to real distribution. D^0 is forced to decay into $K^-\pi^+$ by PYTHIA6.

3. Smear K and π momenta according to momentum resolution in Eq. 4.10;

4. Smear K and π start position according to 2D distribution of DCA_{XY} versus DCA_Y from real data;

5. Reconstruct D^0 from its daughters with smeared momentum and position. In this step, topological cuts and acceptance cuts are applied. Efficiency loss due to track reconstruction or PID etc, such as TPC reconstruction efficiency (ϵ_{TPC}), PID efficiency (ϵ_{PID}) and HFT matching efficiency (ϵ_{HFT}), would be applied as the weight.

The D^0 reconstruction efficiency in different centrality bins is shown in Fig. 4.11.

4.4.3 D^0 double counting effect

D^0 reconstructed from $K\pi$ might be regarded as $\overline{D^0}$ and counted twice when both kaon and pion are misidentified. To estimate double counting contribution in D^0 signal, the first step is to extract the possibility of kaon and pion to be misidentified. Similar as PID efficiency evaluation, these can be gotten from pure particle samples. Then invariant mass distribution of both real D^0 signal and fake $\overline{D^0}$ signal from mis-PID can be simulated by fast simulation package, as shown in Fig. 4.12(a, b) . Fig. 4.12(c) shows the estimated double counting fraction to total signal counts within $\pm 2.5\sigma$ mass window (R^{double}). Double counting correction need to be done for D^0 yield when calculating D^{*+}/D^0 ratio.

4.4.4   Vertex resolution correction

In the real data, the reconstructed primary vertex is not exactly the same as the real collision vertex due to finite resolution. In the data-driven simulation, we assume that the vertex resolution is negligible and the single track DCA distributions extracted from data are the true distribution to the true vertex. But in peripheral events, vertex resolution might go to hundreds of μm due to low multiplicity, which is comparable to DCA resolution. Fig. 4.13 shows the Full-Width-at-Half-Maximum (FWHM) of the
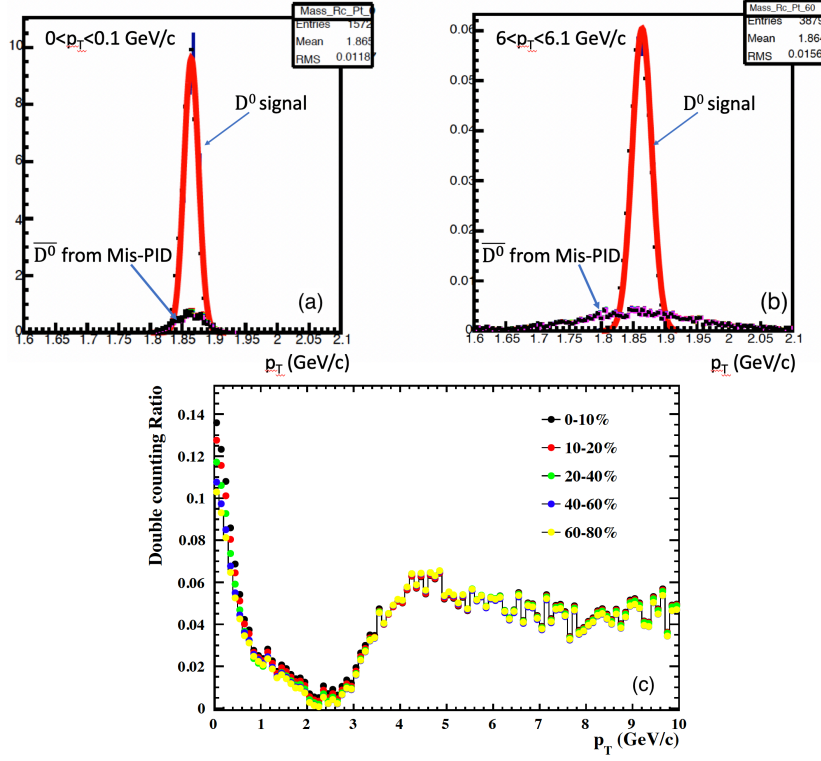
Fig. 4.12   **Plot (a) and (b) is the simulated invariant mass distribution of D^0 signal (red lines) and double counted $\overline{D^0}$ signal (black data points) at $0<p_T<0.1$ GeV/c and $6<p_T<6.1$ GeV/c. Plot (c) is the estimated fraction of double counting effect in reconstructed D^0 signals at different centralities.**

difference in the vertex x-position (V_x) of two randomly-divided sub-events as function as centrality[83]. The large vertex resolution will have additional effect on the D^0 signal counts afters topological cuts applied. To estimate this effect, single PYTHIA $c\bar{c}$ event is embedded into a HIJING Au+Au event, and then the whole event will go through full detector simulation with HFT geometry. In the simulation the detector performance is the same as real data. The vertex resolution correction is calculated as the ratio of D^0 efficiency between HIJING+GEANT simulation and "data-driven" simulation. The correction factor is 1 in 0-50% centrality then decreases to 0.6 in 70-80% centrality.

4.4.5 D^{*+} efficiency

D^* total efficiency is described as the convolution of single soft pion efficiency and D^0 reconstruction efficiency:

$$\epsilon_{D^*} = \epsilon_{D^0}^{reco} \otimes \epsilon_{\pi_s} \tag{4.11}$$

As we have introduced D^0 and π_s efficiency, then D^{*+} efficiency can be simulated from following procedures:

- Decay $D^{*+} \rightarrow D^0 \pi_{soft}$ by PYTHIA. Sample random rapidity $y \in (-1.2, 1.2)$
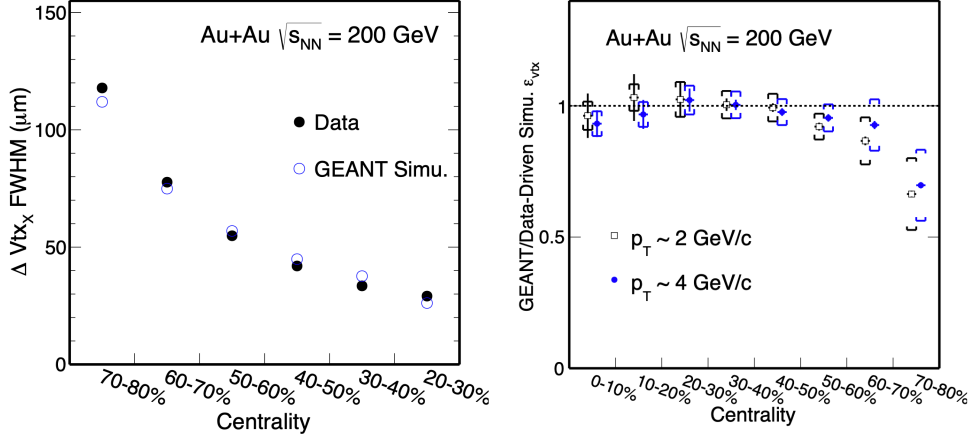
Fig. 4.13   Left: Full-Width-at-Half-Maximum (FWHM) of V_x between two randomly- divided sub-events in various centrality bins[83]; Right: vertex resolution correction factor as function as centrality[83].

and $p_T \in (0, 12)$ GeV/c. The p_T weight w_{p_T} for D^* is set according to D^0 spectra measured in Run14. Suppose D^* and D^0 p_T shape is very close and the difference will not affect efficiency calculation.

- Smear D^0 and π_s p_T. D^0 p_T resolution is from fast simulation while that of π_s is from embedding. D^{*+} is reconstructed using the daughter particles following the same procedure as in real data. After applying acceptance cut $|y| < 1$ as well as p_T weight, we will get D^* distribution without efficiency loss.

- Apply acceptance cuts on D^0 and π_s. Apply weight on D^* according to D^0 and π_s efficiency:

$$\text{weight} = \epsilon_{\pi_s} \otimes \epsilon_{D^0}^{reco} \otimes \epsilon_{D^0}^{mass} \otimes \epsilon_{VTX} \otimes w_{p_T}$$

$$\epsilon_{\pi_s} = \epsilon_{PID} \otimes \epsilon_{TPC} \tag{4.12}$$

$\epsilon_{D^0}^{mass}$ is the correction factor for the cut on D^0 mass and ϵ_{VTX} is the vertex resolution correction for D^0 reconstruction. Because we set a very loss cut ($|gDCA| < 3$ cm) for π_s without requiring matched HFT hits, so there is no further vertex correction for π_s. Then we will get D^* distribution with efficiency loss.

D^{*+} efficiency is calculated in 9 centrality bins (0-5%, 5-10%, 10-20%, .., 70-80%) respectively. Assuming D^{*+} production cross section is proportional to number of binary collisions N_{bin}, D^{*+} in wide centrality bins then can be calculated from the original 9 bins with following equation:

$$\epsilon_{D^*}^{reco} = \frac{\sum_i w_i N_{bin}^i \epsilon_{D^*}^i}{\sum_i w_i N_{bin}^i} \tag{4.13}$$

where w_i refers to events in centrality i. Fig. 4.14 shows D^{*+} total efficiency in 0-10%,
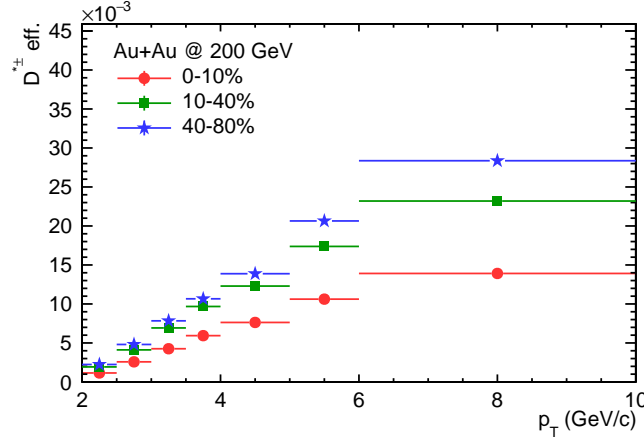
Fig. 4.14   The total efficiency D^{*+} as a function of p_T in different centralties in Run14.

10-40% and 40-80% centralities.

4.5 D^{*+}/D^0 ratio

D^*/D^0 yield ratio is then calculated as:

$$D^*/D^0(p_T) = \frac{N_{D^{*+}}^{raw}/\epsilon_{D^{*+}}^{tot} \times B.r.(D^{*+} \to D^0 \pi_s) \times B.r.(D^0 \to K^- \pi^+)}{N_{D^0}^{raw}/\epsilon_{D^0} \times B.r.(D^0 \to K^- \pi^+)} \qquad (4.14)$$

where $N_{D^*}^{raw}$ and $N_{D^0}^{raw}$ is D^{*+} and D^0 raw counts, and B.R. is short for branching ratio. ϵ_{D^0} is D^0 total efficiency calculated as:

$$\epsilon_{D^0}^{total} = \epsilon_{D^0}^{reco} \otimes \epsilon_{D^0}^{VTX} \otimes (1 - R^{double}) \qquad (4.15)$$

where $\epsilon_{D^{*+}}^{tot}$ is the D^{*+} total efficiency, $\epsilon_{D^0}^{reco}$ is D^0 reconstruction efficiency gotten from data-driven simulation discussed in section 4.4.2, $\epsilon_{D^0}^{VTX}$ is the vertex resolution correction, and R^{double} is the fraction of double counting effect in the D^0 signal. To understand hot medium effect on D^{*+} life time, we also calculate integral yield ratio of D^{*+}/D^0 in $2 < p_T < 10$ GeV/c as function as $N_{<part>}$. As in the efficiency simulation, the input p_T shape might affect final efficiency in very wide p_T bin. So we integral the corrected D^{*+} and D^0 spectra and then take the ratio. The statistic uncertainty is calculated as $\delta_{tot} = \sqrt{\sum_i (\delta_i)^2}$, where δ_i is the statistical uncertainty in fine p_T bin. The statistical uncertainty of D^*/D^0 is calculated by error propagation equation. Final results will be discussed in next chapter.

4.6   Systematic uncertainty

The systematic uncertainty is estimated by varying cuts and then going through the same analysis procedure. The difference between results under different cuts would be

regarded as systematic uncertainty.

$$\Delta_{sys} = \frac{\text{Results(varied cuts)} - \text{Results(default)}}{\text{Results(default)}}$$

$$\Delta_{sys}^{tot} = \sqrt{\sum_i (\Delta_{sys}^i)^2}$$

(4.16)

We consider following systematic sources:

- Soft pion TPC tracking efficiency. Vary nHitsFit>20 to nHitsFit>25.

- p_T cut on daughter tracks. Vary p_T cut for K^-/π for D^0 reconstruction from $p_T > 0.3$ GeV/c to $p_T > 0.6$ GeV/c. Vary p_T cut for π_s from $p_T > 0.15$ GeV/c to $p_T > 0.2$ GeV/c.

- Raw yield extraction. Change fitting method to bin counting method. The integral range for bin counting is within 5σ to include the bump structure.

- D^0 topological cuts efficiency. Change default D^0 topological cuts to tight/loose cuts. The maximum difference to the default value would be regarded as the systematic uncertainty. Because of the limitation of D^{*+} statistics, instead of using default p_T binning, we take wide binning when estimating systematic uncertainty. This uncertainty is only considered for D^{*+} spectra, as this uncertainty would be canceled for D^{*+}/D^0 yield ratio.

- D^0 vertex resolution correction. This uncertainty is only considered for D^{*+} spectra. Regard as a constant of 5%.

The systematic uncertainty from different sources in 10-40% centrality is shown Fig. 4.15.

(a) D^{*+} **spectra** 　　　**(b)** D^{*+}/D^0 **ratio versus** p_T 　**(c)** D^{*+}/D^0 **intetgral yield ratio**
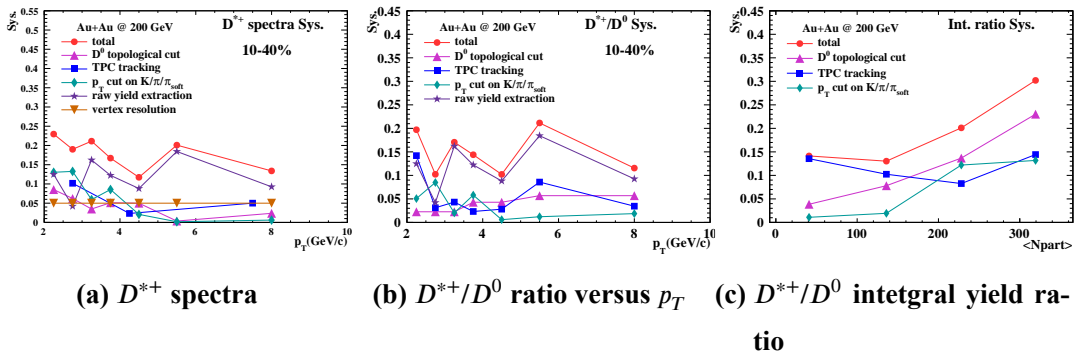
Fig. 4.15　Systematic uncertainty from different sources in 10-40% centrality in Run14.

Chapter 5   Results and discussion

5.1 e^{HF} v_2 at low energy - charm quark collectivity

5.1.1   The energy dependence of e^{HF} v_2

Figure 5.1 shows heavy flavor electron elliptic flow v_2 as a function of p_T at mid-rapidity ($|\eta| < 0.8$) in Au+Au collisions at $\sqrt{s_{\mathrm{NN}}} = 27$ (green square), 54.4 (blue circle) and 200 GeV (gray star) [75]. The shaded area shows an estimation of the upper limit of non-flow contribution as discussed in Section 3.9. It is comparable to that in Au+Au collisions at 200 GeV. The e^{HF} v_2 data points at 54.4 GeV are significantly higher than the estimated upper limit of non-flow contribution. The integrated e^{HF} v_2 at $p_T > 1.2$ GeV/c is 0.109 ± 0.008 (stat) ± 0.014 (sys), while the estimated upper limit of non-flow contribution is 0.024. Heavy flavor electrons are predominately contributed by charm hadrons decay at low energy and low p_T, as is shown in Fig. 5.2(left) from a FONLL pQCD calculation. The significant v_2 of e^{HF} observed in 54.4 GeV indicates that charm quarks also have strong interaction with the medium in Au+Au collisions at 54.4 GeV, although the collision energy is nearly a factor of 4 lower with respect to $\sqrt{s_{\mathrm{NN}}} = 200$ GeV. Figure 5.2 (right) shows the collision energy dependence of total charm quark production cross section in p+p collisions from FONLL and PYTHIA calculations [132-135]. The charm production cross section decreases quickly with decreasing collision energy. The total charm production cross section at 54.4 GeV collisions is lower by one order of magnitude compared to that at 200 GeV collisions. This makes the charm measurements at low energy very challenging.

Figure 5.3 shows the energy dependence of e^{HF} v_2 and comparison to those of light hadrons at $p_T = 1.45$ GeV/c. The points for Au+Au 27 and 54.4 GeV collisions are calculated within $1.3 < p_T < 1.6$ GeV/c. The points for 39, 62.4 GeV collisions are directly obtained from [75]. For Au+Au 200 GeV collisions, we take the shape of TAMU model to fit the data points from [75]. Then the value at $p_T = 1.45$ GeV/c is extrapolated from fitting function. For Pb+Pb collisions at $\sqrt{s_{\mathrm{NN}}} = 2.76$ TeV, we combine the e^{HF} v_2 at 0-10%, 10-20% and 20-40% centrality bins, weighting with $\langle N_{coll} \rangle$ [136], and then do the interpolation. Although generally the e^{HF} v_2 is decreasing at low energy, the strength of charm flow is comparable from $\sqrt{s_{\mathrm{NN}}} = 54.4$ GeV to 2760 GeV. There is a hint that the heavy flavor electron v_2 is much lower in Au+Au $\sqrt{s_{\mathrm{NN}}} = 27$ GeV collisions than those in higher energy collisions. The difference of
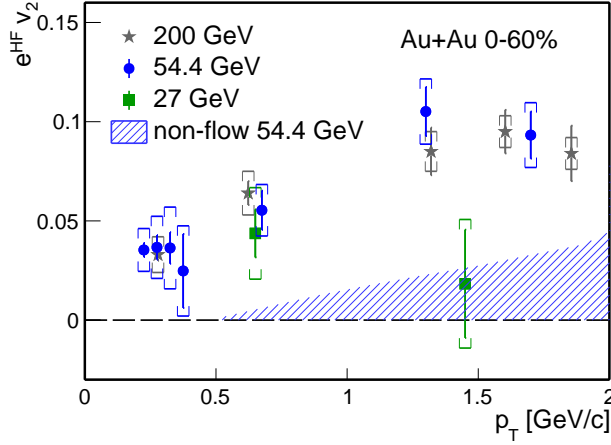
Fig. 5.1   **Measurements of heavy flavor electron v_2 in Au+Au $\sqrt{s_{\rm NN}}$ = 27, 54.4 and 200 GeV [75] collisions. The blue shadow shows the estimated upper limit of non-flow contribution in Au+Au 54.4 GeV collisions.**
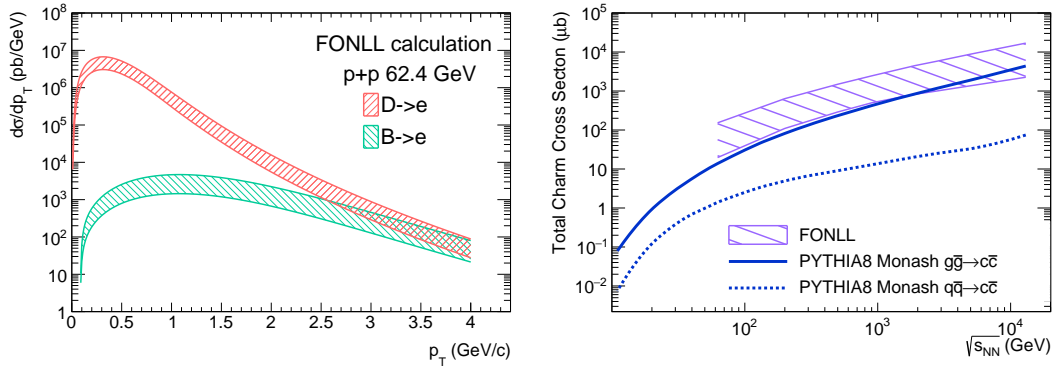
Fig. 5.2   **FONLL and PYTHIA calculations of heavy flavor production in p+p collisions. The error bands of FONLL calculations include uncertainties from scales and masses. (Left) Electron production yield from D or B meson decay. The input D meson spectrum are composed of 70% D^0 and 30% D^+, including the feed down from D^*. (Right) The total charm quark production cross section as a function of collision energy in p+p collisions from FONLL and PYTHIA8.2. FONLL calculation is from [132-133]. The PYTHIA8.2 calculations are obtained with the default Monash tune [134-135].**

heavy flavor electron v_2 in Au+Au 27 and 54.4 GeV collsions is $\Delta v_2 = v_2^{54.4} - v_2^{27} = 0.08 \pm 0.03(stat) \pm 0.03(sys)$ in $1.3 < p_T < 1.6$ GeV/c, which is larger than 0 with a significance of 1.6σ. The decrease of v_2 of light hadrons with energy is slower than charm daughters. The v_2 of pions and kaons keep decreasing very slowly the decreasing collision energy in a center-of-mass energy range from several TeV to $\sim$ 10 GeV. The decrease of ϕ meson v_2 is slow when $\sqrt{s_{\rm NN}} > 20$ GeV. However, ϕ meson v_2 drops quickly when the collision energies are below 20 GeV. With decreasing collision energy, heavier mass particles v_2 drops faster than lighter ones, which suggests there is a change

in the QCD medium properties with decreasing energy.
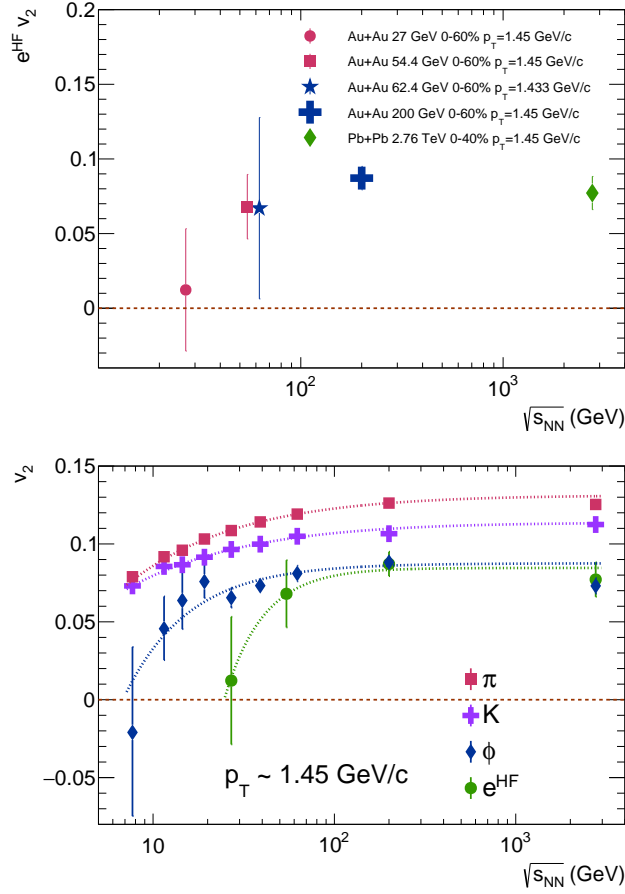
Fig. 5.3 **The collision energy dependence of heavy flavor electron v_2 and light hadrons ($\pi/K/\phi$) at $p_T \sim 1.45$ GeV/c. The error bars include both statistical and systematic uncertainties. (Upper) The heavy flavor electron v_2 at $p_T \sim 1.45$ GeV/c. The data points of Au+Au 27, 39, 54.4 and 62.4 GeV collisions is directly from this measurement and [75]. The data points for Au+Au 200 GeV and Pb+Pb 2.76 GeV collisions are extrapolated to $p_T = 1.45$ GeV/c from measurements [75, 136]. (Bottom) Comparison of v_2 between heavy flavor electron and light hadrons. The data points for heavy flavor electron are the same as the upper plot. The data points for light hadrons are interpolated from [137-138] (Au+Au collisions, 0-80% centrality), and [139-140] (Pb+Pb collisions, 0-50% centrality). The red, magenta, blue and green dash lines are the fit to data points. The fitting functions are $f = p_0 + p_1(1 + \frac{p_2}{\sqrt{s_{NN}}} + \frac{p_3}{\sqrt{s_{NN}}^2})^{p_4}$ for $\pi/K/\phi$, and $f = p_0 + p_1(1 + \frac{p_2}{\sqrt{s_{NN}}^2})^{p_3}$ for e^{HF}.**

5.1.2   Comparison on the p_T dependence of e^{HF} and identified particles v_2

Fig. 5.4 shows comparison of the p_T dependence of elliptic flow for heavy flavor electron and that of light hadrons ($\phi/K/\pi$) in Au+Au 27 and 54.4 GeV collisions. The

strength of heavy flavor electron v_2 is comparable to that of light hadrons at 54.4 GeV collisions. While at 27 GeV collisions, e^{HF} v_2 at $p_T > 1$ GeV/c is relatively lower compared to those of light hadrons. It suggests that charm quarks might be not fully thermalized in $\sqrt{s_{NN}} = 27$ GeV collisions. As the momenta of heavy flavor electrons are smaller than their parents, direct comparison of heavy flavor electrons to that of light hadrons has some ambiguities. To do a more fair comparison, we assume the D^0 follows the NCQ scaling as the light flavors and studied the expected $D \rightarrow e$ v_2 via a Monte Carlo study.
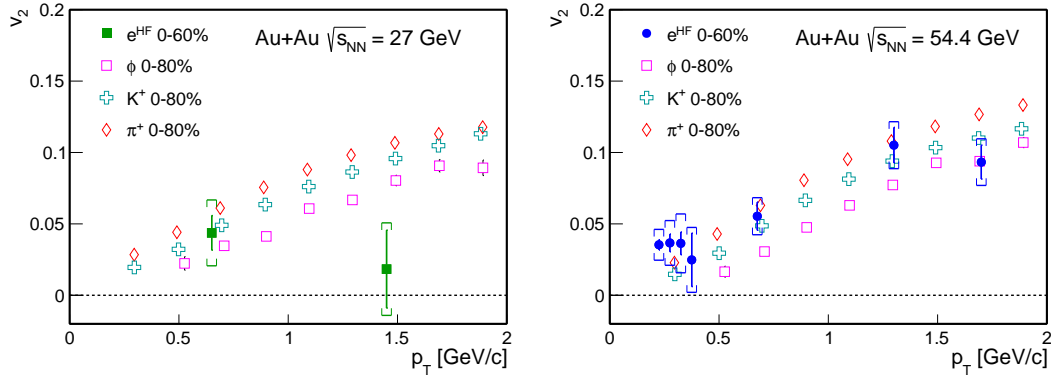
Fig. 5.4   **The elliptic flow of heavy flavor electrons and light hadrons ($\phi/K/\pi$) in Au+Au $\sqrt{s_{NN}} = 27$ and 54.4 GeV collisions in minimum bias events.**

Decay channels	Branching ratio
$D^0 \rightarrow e^+ v_e \rho^-$	3.4%
$D^0 \rightarrow e^+ v_e K^{*-}$	2.7%
$D^0 \rightarrow e^+ v_e \overline{K^0} \pi^-$	0.2%
$D^0 \rightarrow e^+ v_e K^- \pi^0$	0.2%
$D^0 \rightarrow e^+ v_e \overline{K^{*0}} \pi^-$	0.4%
$D^0 \rightarrow e^+ v_e K^{*-} \pi^0$	0.4%
$D^0 \rightarrow e^+ v_e \pi^-$	0.2%
$D^0 \rightarrow e^+ v_e \rho^-$	0.2%
Total	7.7%

Table 5.1   **Decay channels used in the $D^0 \rightarrow e$ v_2 simulation.**

The D^0 is forced to decay in semileptonic channel by PYTHIA6. The channels included in the simulation are listed in Table 5.1. Because v_2 has strong centrality de-
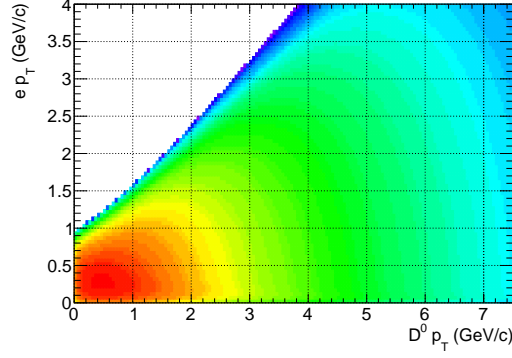
Fig. 5.5 The distribution of daughter electrons p_T versus parent D^0 p_T. The input D^0 spectra shape is taken from FONLL calculation in p+p collisions at 62.4 GeV. The $D^0 \to e$ decay channels are listed in Table 5.1.
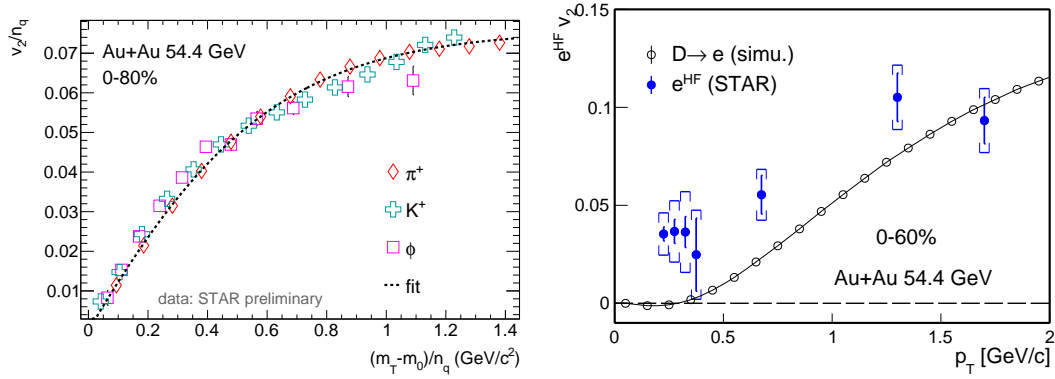
Fig. 5.6 The elliptic flow of light flavor mesons ($\pi/K/\phi$) follows NCQ scaling at Au+Au 54.4 GeV collisions (left plot). The points in the right plot are the estimated $D \to e \, v_2$ with the assumption that D^0 v_2 follows universal NCQ scaling as light flavor hadrons. The shape of D^0 spectra at 54.4 GeV collisions is assuming the same as that of 200 GeV collisions [83].

pendence, and heavy quarks production yields are proportional to $<N_{coll}>$ while light quarks are $<N_{part}>$, so fine centrality bins are desired. The input D^0 spectra and v_2 are divided into 3 centrality bins: 0-10%, 10-40%, 40-80%. The input D^0 spectra shape is taken from FONLL calculations in p+p collsions at 62.4 GeV [132-133]. The D^0 spectra from FONLL calculation is then scaled with $<N_{coll}>$. The $<N_{coll}>$ in different centralities are taken from Au+Au 62.4 GeV collisions[121]. The input v_2/n_q is fitted under 3 centrality bins: 0-10%, 10-40%, 40-80%. The D^0 v_2 is taken into account by applying a weight to the initial D^0 azimuthal angle $w = 2v_2 \cos(2(\phi - \Phi))$, where v_2 is the assumed D^0 elliptic flow. The NCQ scaled v_2 of light mesons ($\pi/K/\phi$) are fitted

with transformed Fermi-Dirac function, shown in Fig. 5.6 (left):

$$v_2/n_q(x) = \frac{a}{1 + e^{-(x-b)/c}} - \frac{a}{1 + e^{b/c}},$$

$$x = (m_T - m_0)/n_q$$

(5.1)

The function is equal to 0 at $p_T = 0$ and becomes flat at high p_T. We will take the fitting function to extrapolate v_2/n_q up to $(m_T - m_0)/n_q < 2.5$ GeV/c^2. For $(m_T - m_0)/n_q > 2.5$ GeV/c^2 ($p_T \sim 6.5$ GeV/c), we assume that D^0 $v_2 = 0$. Because the electrons at $p_T < 2$ GeV/c are dominantly decayed from parents with $p_T < 6.5$ GeV/c, as is shown in Fig. 5.5. The simulated $D^0 \to e$ v_2 is comparable to that of e^{HF} from data at $p_T > 1$ GeV/c within uncertainties, shown in Fig. 5.6 (right). It suggests that the charm quark may be close to thermal equilibrium with the medium at Au+Au $\sqrt{s_{NN}} = 54.4$ GeV too. At $p_T < 0.5$ GeV/c, our measured heavy flavor electron v_2 is systematically higher than the simulated v_2 while the latter is almost zero. In the current measurement, photonic electron backgrounds have been subtracted to obtain the non-photonic electron v_2. The major sources for non-photonic electrons are charm and bottom hadron decays. But there may be a potential contribution from the Kaon→e (K_{e3}). The fraction of K_{e3} in non-photonic electron is very small in Au+Au 200 GeV collisions. The contribution at 54.4 and 27 GeV will need to re-evaluated.

5.1.3   Model comparison

Fig. 5.7 and 5.8 show the experiment measurements compared with TAMU [74] and PHSD [141-142] calculations.   In both TAMU and PHSD model, a strongly coupled ap-
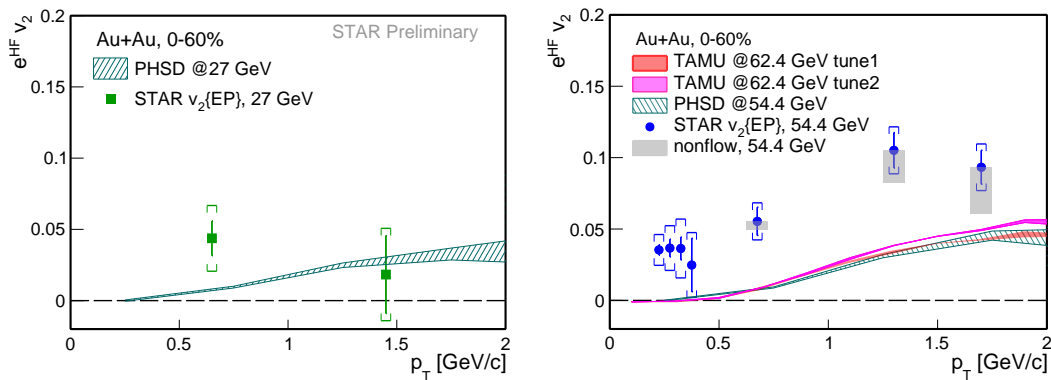
Fig. 5.7   Heavy flavor electron v_2 in Au+Au 27, 54.4 GeV from STAR measurements and models (TAMU: [74], PHSD: [141-142]).

proach is realized, and the heavy quarks interact with the quasi-particles in the medium elastically without gluon radiation process. However, they differ in the approach of solving the transport in the medium.
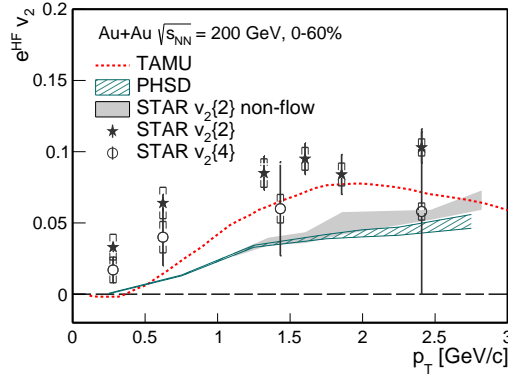
Fig. 5.8   **Heavy flavor electron v_2 in Au+Au 200 GeV collisions from STAR [75] measurements and models [75, 141, 143].**

In TAMU model, the microscope heavy quark interactions with quarks and gluons in the medium are evaluated using a non-perturbative T-Matrix calculations [144-145]. The calculated heavy quark transport coefficients is applied into macroscopic Langevin simulations of heavy quark diffusion through a strong coupled QGP background medium [74, 143]. The initial spectrum of charm and bottom are first generated from FONLL and then smeared with the consideration of cold nuclear matter (CNM) effects. The Cronin effect is believed to be the most important CNM effects in low energy collisions [146-147]. The evolution of the QGP is modeled by ideal 2+1D hydrodynamics. When the system is below the critical temperature, heavy quarks are hadronized through coalescence (using Resonance Recomination Model) and fragmentation. The diffusion of D and B mesons in the hadronic phase is described using effective scattering amplitudes of bulk hadrons.

The PHSD model, short for parton-hadron-string dynamics transport approach, employs a non-equailibrium microscopic transport approach for the QGP dynamics, hadronization, and the hadronic phase [141]. In PHSD calculations, charm quarks interact with the off-shell massive partons in the QGP. The masses and width of the partons and the scattering cross section are given by the dynamical quasiparticle model (DQPM) which is matched to the lattice QCD equation of state. The heavy quark hadronization in PHSD model implement both coalescence and fragmentation mechanism too. The hadronized B and D mesons interact with various hadrons in hadronic phase with the cross sections calculated from an effective Lagrangian [141-142].

e^{HF} v_2 from both TAMU and PHSD calculations are lower than the centroid of data points which are measured by event plane method. If taking account the upper limit of estimated non-flow contribution and the uncertainties, data and model calculations are comparable at p_T >1 GeV/c.

5.1.4   Outlook of this analysis

Fig. 5.9 shows heavy flavor electron v_2 results in Au+Au 54.4 GeV collisions compared with that of 62.4 GeV collisions [75]. The systematic uncertainties are improved compared to those of 62.4 GeV collisions too, despite that the signal to background ratio is expected to be lower due to the faster decrease of charm quark cross section with respect to light quarks with the decreasing of collision energy. This is owing to the better description of the detector in the current STAR simulation (embedding), especially the material budget. Also, the statistical fluctuation of photonic electron v_2 from simulation is reduced. So both photonic electron reconstruction efficiency and v_2 have smaller uncertainties compared to [75]. However, it is still very challenging to reach higher p_T, because the electron purity drops quickly at $p_T > 2$ GeV/c. The current 54.4 GeV data does not include BEMC information. High purity electron samples at $p_T > 1.5$ GeV/c are expected to be extracted from the requested reproduction of 54.4 GeV data with BEMC.
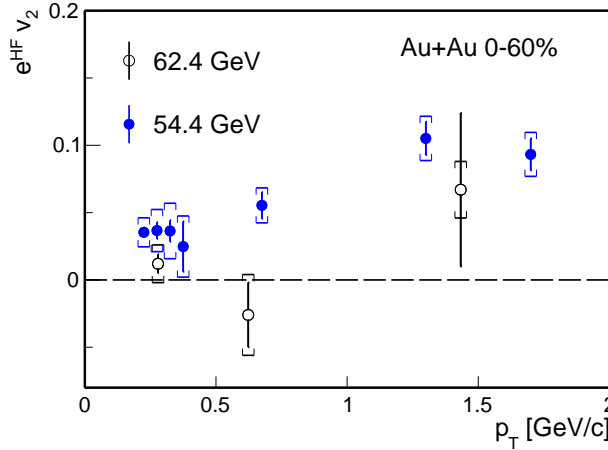
Fig. 5.9   Heavy flavor electron v_2 in Au+Au 54.4 and 62.4 GeV collisions [75]. The data uncertainty is greatly improved in this analysis.

As we have discussed in last section, the contribution of $K \to e$ in non-photonic electrons (NPE) need to be further evaluated too. $K \to e$ reconstruction efficiency and v_2 can be estimated by standard embedding method or fast simulation. To evaluate its fraction in NPE at Au+Au $\sqrt{s_{NN}} = 54.4$ GeV, it also requires a good understanding of input kaon spectra.

5.2 D^{*+} production - charm quark energy loss

To fully understand charm quarks interaction with the hot medium, it is crucial to have measurements on various charm hadron species. The fragmentation branching ratio of $c \rightarrow D^0$ ($\bar{u}c$) is 61.41% while $c \rightarrow D^{*+}$ ($\bar{d}c, J^P = 1^{-1}$) is 23.86% [148] (average of ep/pp/ee collisions). Furthermore, nearly 2/3 of D^{*+} would decay to D^0. So as a complementary to D^0 measurements, it is desired to check if D^{*+} R_{AA} follows similar tendency as that of D^0 in hot medium.
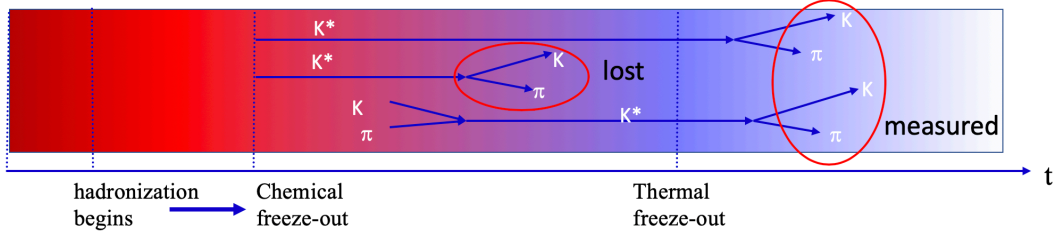
Fig. 5.10   If the K^* decays before thermal freeze out, this K^* cannot be reconstructed by the final state daughter particles due to elastic scattering. On the other hand, a kaon might combine with a pion and K^* is regenerated. The final measured K^* yield is a result of the competition between re-scattering and regeneration.

Apart from fragmentation and D^{*+} feed-down contribution to D^0, possible medium effect on D^{*+} production yield might also modify D^{*+}/D^0 ratio in Au+Au collisions. Re-scattering phenomenon has been observed in K^* ($\bar{d}s, J^P = 1^{-1}$) by STAR experiment [149], as is illustrated in Fig. 5.10. The quark component of K^* and D^* just differ in one quark, replacing $s \rightarrow c$, and the J^P quantum numbers of them are the same. Because the K^* life time is so short ($\tau(K^*(892)) = 4\text{fm}/c$) that it might decay before thermal freeze out. As the medium is in rich of pions, there is a high possibility that its decay daughter will be scattered elastically by the particles in the medium. Then this K^* can not be reconstructed from the final state daughters, and the final measured K^* yield would decrease. Although the life time of D^* in the vacuum is long $\tau \sim 2000$ fm/c, its spectra function is predicted to be broadened in strongly-coupled QGP medium [150]. In other words, D^{*+} life time might be much shorter in the medium, which may result in the lower yield of measured D^*.

5.2.1 D^{*+} spectra

D^{*+} invariant yield is calculated with following equation:

$$\frac{d^2N}{2\pi p_T dp_T dy} = \frac{N^{raw}}{2\pi p_T \Delta p_T \Delta y \times N_{events} \times \epsilon_{D^{*+}}^{tot} \times B.R.} \quad (5.2)$$
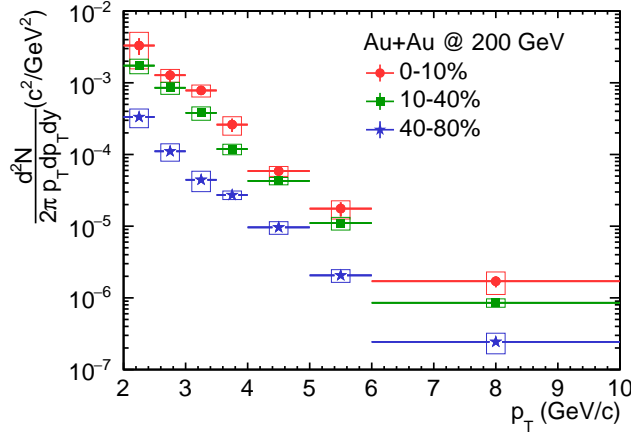
Fig. 5.11 D^{*+} **invariant yield as a function of** p_T **in different centralities (Run14).**

where N^{raw} is D^{*+} raw counts, and B.R. is short for branching ratio=67.7% $\times$ 3.89%. Δy is the rapidity range $\Delta y = 2$ and Δp_T is p_T bin width. $\epsilon^{tot}_{D^{*+}}$ is the D^{*+} total efficiency. Fig. 5.11 shows the final measured D^{*+} spectra in different centralities.

5.2.2 D^{*+}/D^0 ratio
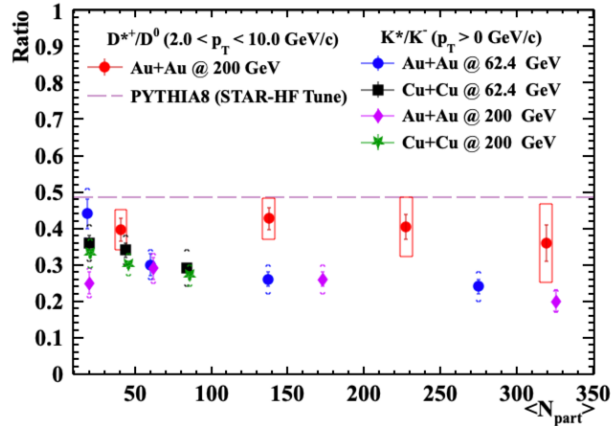
Fig. 5.12 D^{*+}/D^0 **integrated yield in Au+Au collisions at** $\sqrt{s_{NN}} = 200$ **GeV (Run14).** K^*/K^- **ratio is higher in peripheral collisions compared to central collisions, while** D^{*+}/D^0 **ratio have no strong centrality dependence.**

Fig. 5.12 shows the D^{*+}/D^0 integrated yield ratio ($2<p_T<10$ GeV/c) as a function of $<N_{part}>$. If the hot medium significantly shorten the D^{*+} life time, D^{*+}/D^0 ratio is expected to be lower in most central collisions compared to peripheral collisions, because of the lower multiplicity in peripheral collisions. However, there is no obvious centrality dependence observed in Fig. 5.12, which means the rescattering of D^{*+} in hadronic phase has no significant impact on measured D^{*+} yield. So D^{*+} measurements are able to be combined with other charm hadrons for the study of charm diffusion and

energy loss in the medium.

As currently D^{*+} measurements in p+p collisions is limited by statistics [151], R_{AA} calculation will introduce additional uncertainties. Another way is to study the D^{*+}/D^0 ratio and then compare with PYTHIA calculation:

$$R_{AA}^{D^*} = \frac{N_{AA}^{D^*}}{N_{coll} N_{pp}^{D^*}} = \frac{N_{AA}^{D^*}}{N_{AA}^{D^0}} \frac{N_{AA}^{D^0}}{N_{coll} N_{pp}^{D^0}} \frac{N_{pp}^{D^0}}{N_{pp}^{D^*}} = \frac{r_{AA}^{D^*/D^0}}{r_{pp}^{D^*/D^0}} \cdot R_{AA}^{D^0} \tag{5.3}$$

Fig. 5.13 (left) shows D^{*+}/D^0 as a function of p_T under different centralities and PYTHIA calculation. D^{*+}/D^0 at RHIC are comparable to measurements at LHC from ALICE in 0-10% centrality despite 25 times energy difference, shown in the top panel. The rising tendency of PYTHIA calculation at low and intermediate p_T is mainly due to the p_T shift resulting from mass difference of D^0 and D^{*+}. The D^0 R_{AA} in 0-10% centrality at Au+Au 200 GeV collisions are shown as the black and open circles in Fig. 5.13 (right). Similar suppression structure is observed in the D^0 R_{AA} as those of light hadrons. D^0 R_{AA} is strongly suppressed at high p_T. The bump structure of D^0 R_{AA} around $p_T \sim 2$ GeV/c might result from the collective motion of charm quark. The measured D^{*+}/D^0 ratio in Au+Au are consistent with PYTHIA calculations, which means the D^* feed down contribution to ground state D^0 and D^+ is the same as in p+p collisions. It closes the check on charm mesons and confirms that the D^0 R_{AA} structure is not due to the hadronization branching ratio of charm mesons in Au+Au collisions. Furthermore, it can be inferred from the consistency of D^{*+}/D^0 yield ratio in Au+Au and p+p collisions, that the D^{*+} R_{AA} should have similar suppression as that of D^0 [84]. So D^{*+} measurement also indicates that the charm quarks have the strong interaction with the medium.

5.3   Summary

Due to the large masses of heavy quarks, they are predominately produced in the initial hard scattering process in the heavy ion collisions before QGP formation. Thus they are regarded as an excellent probe to QGP dynamics. In this section, we summarize what we have learned from current charm measurements at RHIC and LHC.

5.3.1   Low momentum - Diffusion

Since the masses of heavy quarks (c, b) are much larger than typical QGP temperature, at low momentum, they interact with background medium through multiple elastic scatterings with relatively small momentum transfer. Thus their propagation in QGP at
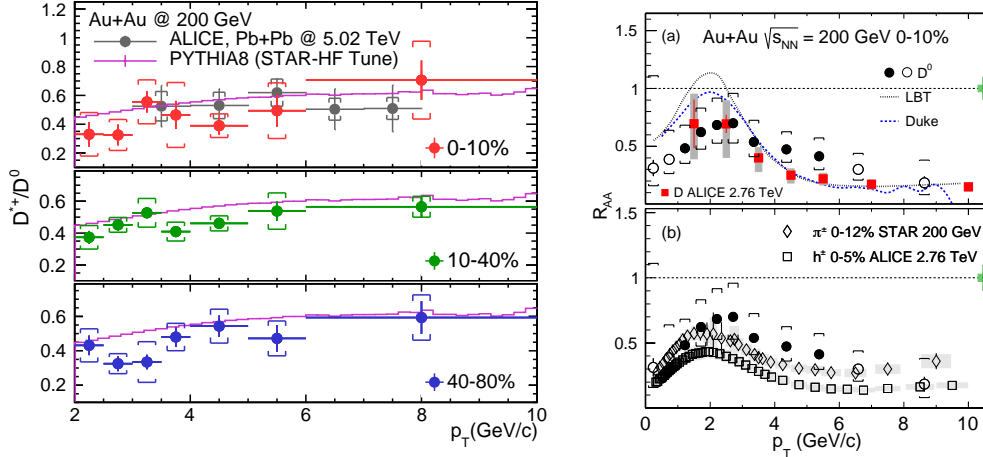
Fig. 5.13   **Left plot: D^{*+}/D^0 ratio in 0-10%, 10-40%, 40-80% centrality bins in Au+Au collisions at $\sqrt{s_{NN}} = 200$ GeV (Run 2014). The results are consistent with PYTHIA calculations (purple line) within uncertainty. Dark Gray points in the top panel are in 0-10% centrality in Pb+Pb $\sqrt{s_{NN}} = 5.02$ TeV collisions [152]. Right plot: The measurement of D^0 R_{AA} in Au+Au $\sqrt{s_{NN}} = 200$ GeV. The plot is taken from [84]. The D^0 R_{AA} has a large suppression up to $p_T \sim 10$ GeV/c.**

low momentum can make analogy to Brownian motion. Heavy quark transport properties are characterized by spatial diffusion coefficient $\mathcal{D}_s$, which reveals the coupling strength of the QGP, for example, $\mathcal{D}_s \sim 1/(\alpha_s^2 T)$ in pQCD [61]. Measurements of nuclear modification factor R_{AA} and elliptic flow v_2 of heavy flavor hadrons or their decay daughters are basic experimental observables to analyze $\mathcal{D}_s$. Fig. 5.14 and Fig. 5.15 show D-meson R_{AA} and v_2 measurements from RHIC and LHC. Measurements show that charm mesons have obtained a large v_2 at low p_T in heavy ion collisions at energies from several TeV [136, 153-155] to 200 GeV [65, 75] (and even down to 54.4 GeV as discussed in this thesis). A local peak around $p_T \sim 2 - 3$ GeV/c is also observed in D^0 R_{AA} at RHIC and LHC, known as "flow bump". These phenomena confirm that D-mesons obtain a considerable collectivity at low momentum in these collision systems. The strength of the v_2 of charm hadrons or their decay daughters is a direct reflection of the coupling strength of the medium at low momentum (although the re-scattering at hadronic phase will also increase the v_2 strength). Fig. 5.16 presents $\mathcal{D}_s$ versus temperature from various theory and model calculations, which we have shown at Chapter 1. Following models are able to qualitatively describe D^0 R_{AA} and v_2 results simultaneously: the PHSD model, the TAMU model, the Nantes model (MC@sHQ). $\mathcal{D}_s$ is increasing with temperature in most of the calculations. Current phenomenology suggests that charm quark $2\pi \mathcal{D}_s$ is about 2-5 near T_{pc}, which are consistent with LQCD calculation in quenched approximation without dynamical quark loops.

94
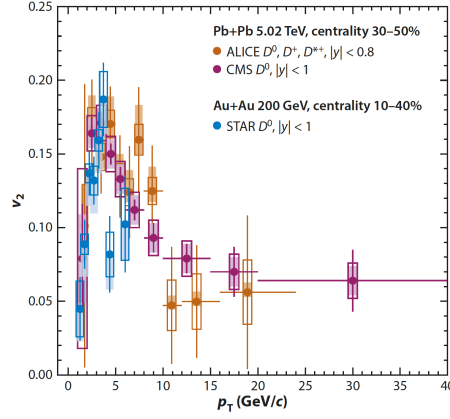
Fig. 5.14   Elliptic flow of D meson in Pb+Pb $\sqrt{s_{NN}} = 5.02$ TeV collisions (30-50%) [153-154], and Au+Au $\sqrt{s_{NN}} = 200$ GeV collisions (10-40%) [65]. The figure is taken from [64].
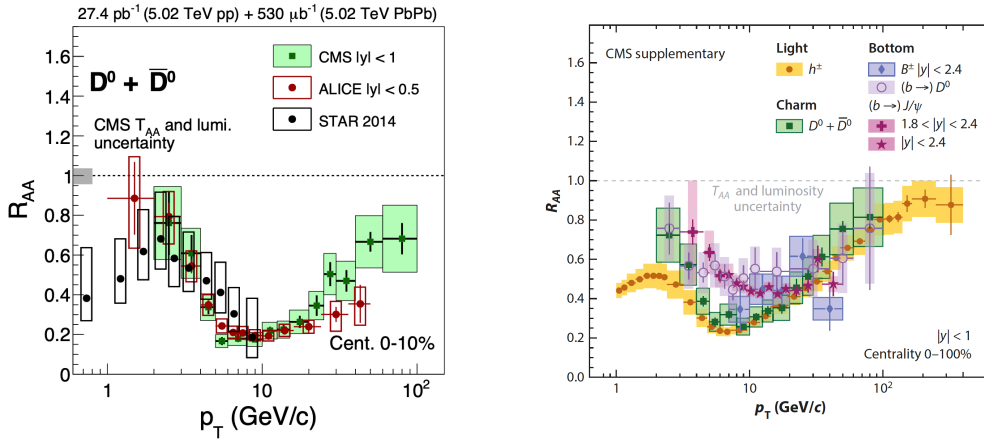
Fig. 5.15   (Left) D^0 R_{AA} as a function of p_T in 0-10% centrality at Au+Au $\sqrt{s_{NN}} = 200$ GeV [83] and Pb+Pb $\sqrt{s_{NN}} = 5.02$ TeV collisions [152, 156]. (Right) R_{AA} as a function of p_T in Pb+Pb $\sqrt{s_{NN}} = 5.02$ TeV collisions in 0-100% centrality from CMS [157] for charged hadrons, prompt D^0, non-prompt D^0, non-prompt J/ψ, B^+. The figures are taken from [64].

5.3.2   Low to intermediate momentum - Hadronization

Since their thermal production rate is strongly suppressed in the medium, the total number of heavy quarks is almost conserved during the evolusion of the system. Thus heavy quarks serve as a good witness for the hadronization process in the QGP. An enhancement of D_s^+/D^0 ratio at LHC and RHIC is observed at intermediate p_T with respect to p+p collisions, just as coalescence mechanism expected because of the strangeness enhancement in the QGP. Hint of B_s/B_0 enhancement in Pb+Pb collisions at LHC is also observed by CMS [158]. A much larger Λ_c^+/D^0 ratio compared to fragmentation baseline is first observed in p+p and p+Pb collisions from ALICE and LHCb [159-160]. Recent development of hadronization via the new color re-connection mode in
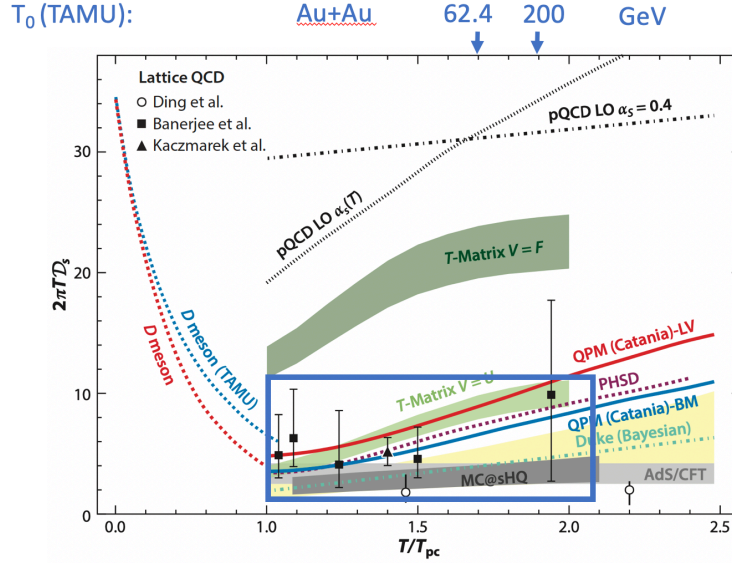
Fig. 5.16 **Charm quark spatial diffusion coefficient $2\pi T \mathcal{D}_s$ as a function of reduced temperature T/T_{pc} from multiple theory and model calculations [62, 66-74]. The picture is taken from [64].**

PYTHIA and color ropes in DEPSY model can enhance the production of Λ_c^+ in p+p collisions. However, these calculations are heavily relied on the choice of a plenty of parameters. Additional enhancement of Λ_c^+/D^0 ratios was found in Au+Au and Pb+Pb collisions with respect to p+p collisions, shown in Fig. 5.17 [109, 161]. Models employing coalescence mechanism can qualitatively describe the data at intermediate p_T [162-165]. STAR collaboration extrapolates their measurements of major ground-state charm hadrons (Λ_c^+, D_s^+, D^0, and D^+) to low p_T. It is found that the estimated total charm cross section in Au+Au collisions is compatible with N_{bin} scaled value from p+p collisions, if considering the enhanced production of D_s^+ and Λ_c^+. The dominate uncertainty in the estimation arise from the limited p_T coverage in Λ_c^+ measurements. More precise measurements of charm baryon are desired to quantify the total charm cross section, which is essential to provide reference for the measurements of charmonia production.

5.3.3   Intermediate to high momentum - Energy loss

Another feature for D-meson v_2 in Fig. 5.14 is that it reaches peak value around $p_T \sim 3$ GeV/c, then drops at intermediate $p_T \simeq 5 - 10$ GeV/c and the value changes quite slow at $p_T > 10$ GeV/c. Similar structure is observed in D-meson R_{AA} too as shown in Fig. 5.15 (left): A local peak structure is appeared at low p_T, then the value decreases to local minimum around $p_T \sim 10$ GeV/c, and increases slowly at $p_T > 10$ GeV/c. These structures suggest the charm and medium interactions transit from elastic-
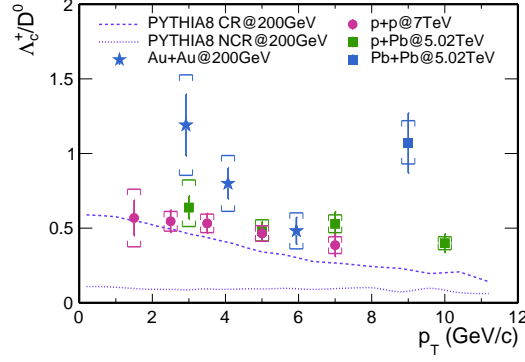
Fig. 5.17 Λ_c/D^0 **ratio as a function of** p_T **in Au+Au** $\sqrt{s_{NN}} = 200$ **GeV/c, Pb+Pb** $\sqrt{s_{NN}} = 5.02$ **TeV, p+Pb** $\sqrt{s_{NN}} = 5.02$ **TeV, p+p** $\sqrt{s_{NN}} = 7$ **TeV collisions. PYTHIA calculations in p+p** $\sqrt{s_{NN}} = 200$ **GeV collisions with default mode (NCR, dash line) and new color reconnection mode (CR, solid line) are also shown in the plot.**

scattering domain at low momentum to radiative-interaction domain at high momentum. Currently it is not very clear when will the radiative energy loss of the heavy quark take over collisional energy loss. If heavy quark elastic interactions at low momentum can be well understood, then it is possible to handle the interplay of elastic and radiative interactions at intermediate momentum. A mass hierarchy of radiative energy loss is expected due to "dead cone" effect (see Chapter 1): $\Delta E_b < \Delta E_c < \Delta E_{u,d,s} < \Delta E_g$. An evidence of charm-bottom hierarchy between the R_{AA} of prompt D^0 and non-prompt D^0 and J/ψ ($b \to D^0, J/\psi$) is observed as shown in Fig. 5.15. Besides of energy loss, R_{AA} is also affected by the modified charm production spectra (due to shadowing effect) and hadronization processes in heavy ion collisions. The differences in initial parton spectra and fragmentation process might account for the phenomena that R_{AA} of charm mesons and light hadrons are very close even at a p_T range where radiative energy loss dominates [166]. At very high p_T when energy-to-mass ratio (Lorenze-γ factor) is large, the mass effect is expected to disappear. As shown in Fig. 5.15 (right), the R_{AA} of charge hadrons and heavy hadrons or their decay products merge at very high p_T.

5.3.4   Perspective

As we have mentioned, despite the success achieved in current charm hadron measurements, there are still questions remaining unsolved. A few topics on heavy flavor measurements in next phase heavy ion experiments are listed here.

- Precise measurements of open bottom production and collectivity over a wide momentum range. Charm quarks might have reached thermalization at RHIC

top energy and LHC. Bottom quark is 3 times heavier than charm quarks, so it is regarded as cleaner probe to QGP dynamics compared to charm. Precise open bottom R_{AA} and v_2 measurements are necessary for the investigation of the role of gluon radiation and elastic scattering in heavy quark energy loss mechanism over a broad momentum range. Besides, a bottom spatial diffusion coefficient can be constrained from open bottom measurements. It also serves as an important cross check to our current understanding of charm quark spatial diffusion coefficient, as it is believed that $\mathcal{D}_s$ is an universal parameter to reflect QGP coupling strength. These measurements are critical to the precise evaluation of total bottom cross section, which are significant for the interpretation of Y measurements.

- Precise measurements of D_s^+ and Λ_c^+ hadrons production, especially at very low p_T to gain deeper understanding of the recombination process of hadron formation in the QGP medium. Although models implementing coalescence mechanism can reproduce the enhancement in intermediate p_T, powerful constrains at low p_T is still vacancy. Furthermore, current measurements indicate that D_s^+ and Λ_c^+ contributes a lot to total charm cross section which are crucial to provide precise reference for charmonia measurements. Similarly, measurements of Λ_b and B_s are desired in the future measurements too, as they make contributions to total bottom cross section and a hint of enhancement of B_s/B^0 in Pb+Pb at LHC has already been observed.

- New observables such as the modification of angular correlations between heavy flavor hadrons in A+A collisions with respect to p+p collisions, which is predicted to be sensitive to energy loss mechanism from low to intermediate momentum [167]. Moreover, heavy flavor tagged jet measurements are sensitive to path length dependence of energy loss mechanism [168].

A new experiment named sPHENIX at RHIC are expected to start running at early 2020s, while the experiments at LHC are preparing detector upgrades for High-Luminosity LHC (HL-LHC) in the late 2020s. We will focus on the sPHENIX detector at RHIC which will be discussed in detail in next chapter.

Chapter 6　Outlook - Future heavy flavor program at RHIC

After over 20 years operation of the Relativistic Heavy Ion Collider (RHIC), experimental measurements have confirmed the existence of Quark Gluon Plasma. We have moved forward to a new stage to probe the inner working of the strong-coupling hot nuclear matter. Heavy quarks serve as an unique probe to the early dynamics of QGP due to their large masses. In this chapter, we will introduce a new generation experiment at RHIC in 2020s - the sPHENIX experiment. The inner most of the sPHENIX tracking system is the Monolithic Active Pixel Vertex (MVTX) detector, which will provide precise secondary vertex reconstruction for heavy flavor measurements. The heavy flavor program at sPHENIX will be introduced. The simulation of Λ_c^+ production measurements in future sPHENIX detector will be discussed.

6.1　The sPHENIX detector

The sPHENIX detector is a next-generation under-construction detector for hard probe measurements at the RHIC at Brookhaven National Laboratory (BNL)[90]. The primary physics goal for sPHENIX includes jets measurements, Υ suppression, heavy flavor physics and cold QCD. The first data taking at sPHENIX is planned to begin at 2023. The current operation plan of the sPHENIX detector scheduled by BNL is 3 years run including p+p, p+Au and Au+Au collisions at $\sqrt{s_{\mathrm{NN}}}$ = 200 GeV.
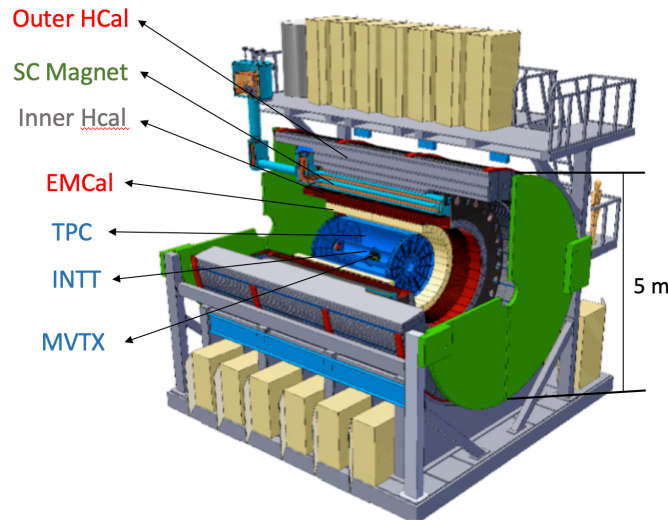
Fig. 6.1　A schematic view of the proposed sPHENIX detector.

The schematic layer of the sPHENIX detector is shown in Fig. 6.2. The detecor is designed as a barrel detector with a coverage of $|\eta| < 1.1$ in pseudo-rapidity for primary vertex within $|Z_{vertex}|$<10 cm and full azimuthal acceptance. The tracking system, from inner most to outer, consists of the Monolithic Active Pixel Vertex (MVTX), the Silicon Strip Intermediate Tracker (INTT) and the Time Projection Chamber (TPC). The detector is also designed with full calorimeter system including an electromagnetic calorimeter (EMCal), and inner and outer hadronic calorimeters (HCal). The sPHENIX detector trigger rate can record 15 kHz in A+A collisions, and the DAQ data rate is higher than 10 GB/s, which enables us to collect sufficient data samples for the future analysis. Detailed introduction for sPHENIX sub-detectors could be found at [169-170].

6.2 MVTX detector and heavy flavor program at sPHENIX

The MVTX detector is a proposed upgrade of sPHENIX detector for heavy flavor measurements and is planned to be available for day-1 physics now. It is a 3-layer silicon pixel vertex detector utilizing the 2nd generation MAPS sensor used for the ALICE ITS2 [171]. The 1st generation MAPS has been utilized in the STAR HFT detector. The MVTX detector will provide a fast integration time ($\sim 5\mu s$) and very low material budget ($\sim 0.3\% \; X_0$) with high tracking efficiency. As we have discussed in Chapter 4, the precise reconstruction of the secondary vertex helps to suppress the combinatorial background of heavy flavor hadrons. The excellent spatial resolution provided by MVTX largely improves the DCA resolution of the tracking system. Besides, the fast readout helps improve the tracking efficiency in high luminosity environment.
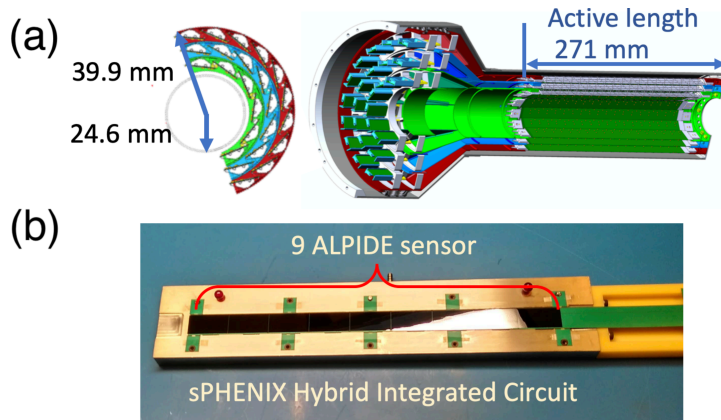
Fig. 6.2 Picture (a) is a schematic view of the MVTX detector. The left plot in picture (a) shows the radius of Picture (b) is MVTX integrated circuit with 9 ALPIDE sensor.

With the MVTX, the sPHENIX detector will enable new and precise measurements

(a) Projected B→D meson R_{CP}.   **(b) Projected B→D meson v_2.**
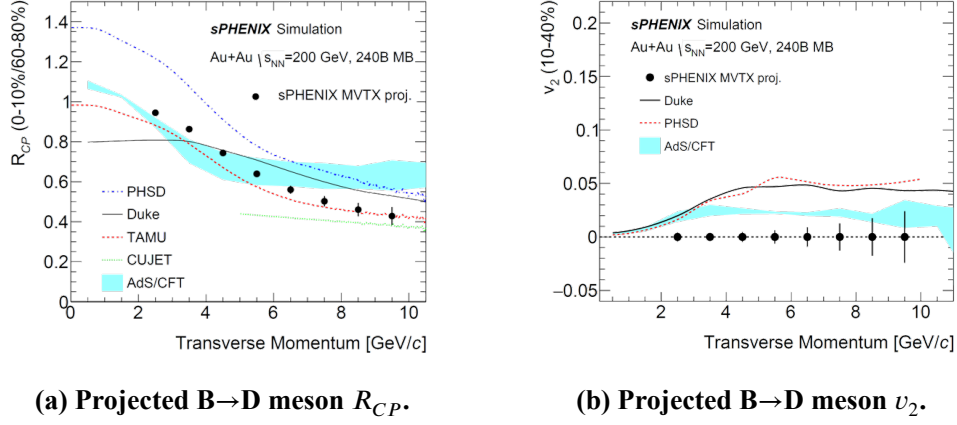
Fig. 6.3   The projected uncertainty of B meson R_{CP} and v_2 with totally 240 billion minimum bias Au+Au events. The precision is enough to separate different models.

on open bottom and charm baryon production that cannot be done before at RHIC energy. Bottom quark is about 3-4 times heavier than charm quark. Fig. 6.3 shows the projected statistic uncertainty of non-prompt D^0 (from B mesons decay). Such precision will provide stringent constraint on heavy quark energy loss and transport models. Apart from B meson studies, rich opportunities on heavy flavor studies would be enabled at sPHENIX, such as b-jet, heavy flavor correlation, heavy flavor baryon production, and so on. Simulation works are carried out to explore the possibility and precision of these measurements in the future sPHENIX experiments. We have done the simulation of Λ_c^+ production, which will be discussed in the following section.

6.3 Λ_c^+ production at sPHENIX

6.3.1   Introduction

Heavy quark hadronization mechanism in the QGP can be studied by measuring the production ratio of different heavy quark hadron species. The STAR experiment have observed strong enhancement of Λ_c^+/D^0 ratio with respect to p+p collisions calculated by PYTHIA 8[109]. An enhancement in baryon-to-meson ratio is expected if the deconfined charm quarks hadronized via coalescence mechanism from the QGP medium. But different coalescence models still have large difference when it goes to the low p_T. Moreover, the enhancement of Λ_c^+/D^0 ratio at low p_T region suggests that Λ_c^+ baryons have sizable contribution to the total charm quark production cross section in QGP. The measurements of total charm cross section provide the baseline for charmonium suppression and coalescence. The charm production cross section from current measurements is largely limited by Λ_c^+ measurements, particularly at low p_T

(p_T<3 GeV/c). In the following sections, we will discuss the performance of Λ_c^+ production measurement in Au+Au collisions at $\sqrt{s_{NN}}$ = 200 GeV in the future sPHENIX experiment with MVTX detector. Based on the projection of the RHIC luminosity, there will be totally 143 billion minimum bias (MB) events recorded for Au+Au collisions within |Vertex$_z$| < 10cm in 3 years run plan with sPHENIX. If it is possible that there are additional 2 years run scheduled, the total recorded MB events is expected to reach 240 billion for Au+Au collisions .

6.3.2   Overview of simulation approach

The full simulation requires us to generate Au+Au event from Hijing and then embed the whole event into the full detector simulation, but it's time-consuming to obtain enough statistics. So in this simulation, a hybrid method will be used, combining full detector simulation and fast simulation. Firstly single particles ($\pi^\pm$, $p/\bar{p}$, $K^\pm$) are embedded into the full Geant4 simulation of the detector and then go through the track reconstruction process. The sub-detector systems include TPC+INTT+MVTX. From this, we are able to extract single track performance, such as DCA 2-dimension distribution, momentum resolution and tracking efficiency. In the second step, the background and signal will be generated by fast simulation package with single track performance applied on the daughter particles. This method have been validated in the D^0 measurement at the STAR experiment [83], when data-driven simulation is applied for calculation of D^0 reconstruction efficiency.
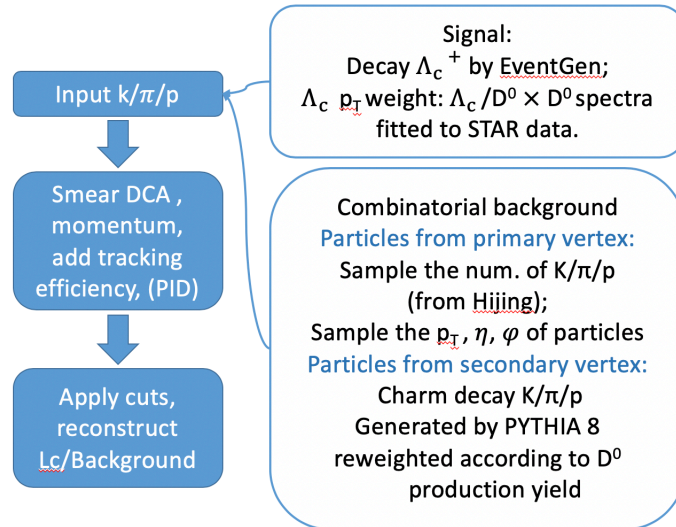
Fig. 6.4   **Flow chart of the hybrid simulation for Λ_c^+ performance calculation with sPHENIX detector.**

The overview of the simulation procedure is summarized as a flow chart in Fig. 6.4

and elaborated below:

1. Sample the primary vertex position in Z-direction (V_z). V_z is fixed to 0 in this simulation.

2. Generate final state particles ($K/\pi/p$) that contribute to the signal and background. The distribution and kinematics of these particles will be determined in this step. Details will be discussed in the following section.

3. Apply detector response on single tracks. Smear the single track kinematics and position. The $K/\pi/p$ momentum is smeared according to momentum resolution while their origin position is smeared according to DCA_{XY} vs DCA_Z 2D distribution. The efficiency loss for the single track is also considered, such as tracking efficiency, TOF matching efficiency (under some scenarios) and PID ability. Four PID scenarios will be discussed in the following sections.

4. Reconstruct the secondary vertex of Λ_c^+ candidate as what we do in real analysis with topological cuts applied. In this simulation, Λ_c^+ is reconstructed through $\Lambda_c^+ \to p\pi^+ K^-$.

6.3.3   sPHENIX detector performance

The assumed detector performance used in this simulation is the same as the $B \to D^0$ projections in MVTX proposal [172]. $K/\pi/p$ are embedded into the full Geant4 simulation of the sPHENIX detector. Fig. 6.5 shows total tracking efficiency for single tracks as a function of p_T, which includes TPC tracking efficiency and MVTX matching efficiency. The tracks is defined as a matched MVTX track only when the track has at least two layers MAPS hits. The tracking efficiency is fitted with following formula:

$$\epsilon_{Tracking} = N \times e^{-(p_T/a)^b} \tag{6.1}$$

To fully describe the particle DCA performance in the barrel-like detector systems (TPC, MVTX etc), 2-dimension distribution of DCA_{XY} vs DCA_z will be used for particle vertex position smearing due to their inner correlations. Fig. 6.6 shows the DCA_{XY} versus DCA_Z 2D distribution at 0.5<p_T<1 GeV/c. DCA is the distance of closet approach between tracks and primary vertex. The detector spatial performance is supposed to be the same no matter the track is from secondary or primary vertex as long as it is within the acceptance. The DCA resolution is extracted by projecting DCA distribution under each p_T bin and then extracting the σ_{DCA} from Gaussian fit. Fig. 6.7 (right) shows the DCA resolution as function as p_T in XY-Plane.

Momentum resolution is also gotten from embedding. Fig. 6.8 (left) shows $K/\pi/p$
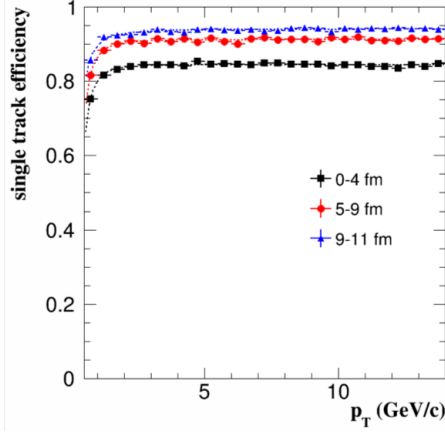
Fig. 6.5　Total tracking efficiency extracted from the full Hijing+Geant4+GenFit2 simulation. The efficiency has included TPC tracking efficiency and MVTX matching efficiency.
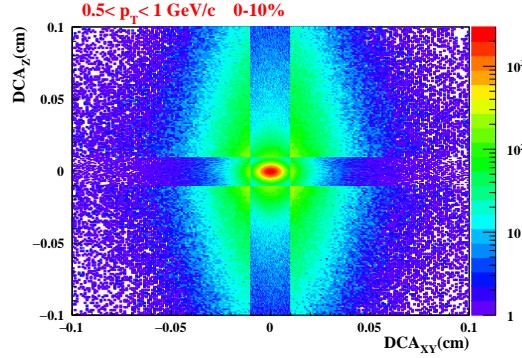
Fig. 6.6　K/p/π DCA$_Z$ VS DCA$_{XY}$ 2D distribution

dp_T/p_T^{true} distribution at $3.1 < p_T < 3.3$ GeV/c. Here, $dp_T = p_T^{rec} - p_T^{true}$, p_T^{rec} is the reconstructed momentum and p_T^{true} is MC p_T. The momentum resolution is evaluated by fitting dp_T/p_T^{true} projection under each p_T bin with Gaussian function. Fig. 6.8 (right) is $\sigma p_T/p_T^{true}$ as function as p_T. The fitting function for Fig. 6.8 (right) is:

$$\frac{\sigma_{p_T}}{p_T} = \sqrt{(\frac{a}{\sqrt{p_T}})^2 + (b \cdot p_T)^2 + c^2} \tag{6.2}$$

6.3.4　Signal

The EvtGen generator is used for Λ_c^+ generation and decay. Λ_c^+ are forced to decay to proton, kaon and pion ($\Lambda_c^+ \to p\pi^+ K^-$). The decay includes three resonant channels as well as the non-resonant channel according to the PDG handbook. We sample uniform rapidity distribution $Y \in (-1, 1)$, and flat ϕ distribution $\phi \in [0, 2\pi)$. For transverse momentum, we first sample flat p_T distribution from 0 to 15 GeV, then set the p_T weight according to the estimated Λ_c^+ p_T spectra. The decay branching ratio (6.23%) will be applied when calculating the signal yield and significance. Fig. 6.9(left) shows current Λ_c^+/D^0 measurements in Au+Au 200 GeV from STAR and comparison with models.

(a) DCA$_{XY}$ distribution at 0.5<p_T<1.0 GeV/c. Different colors refer to different centrality conditions.

(b) DCA$_{XY}$ resolution as function as p_T. The resolution under different centralities are comparible at p_T > 1 GeV/c
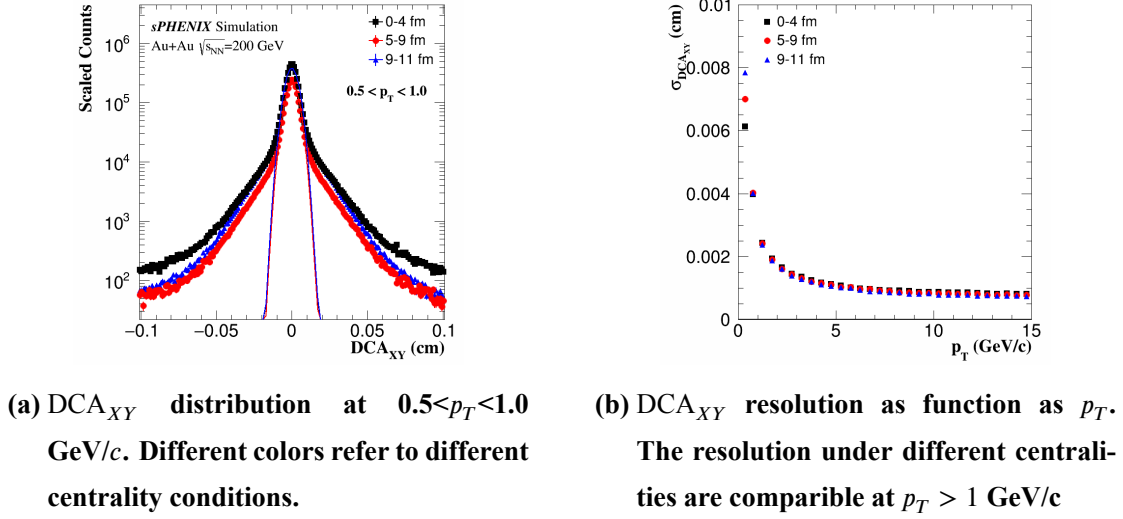
Fig. 6.7   The detector DCA performance in this simulation.
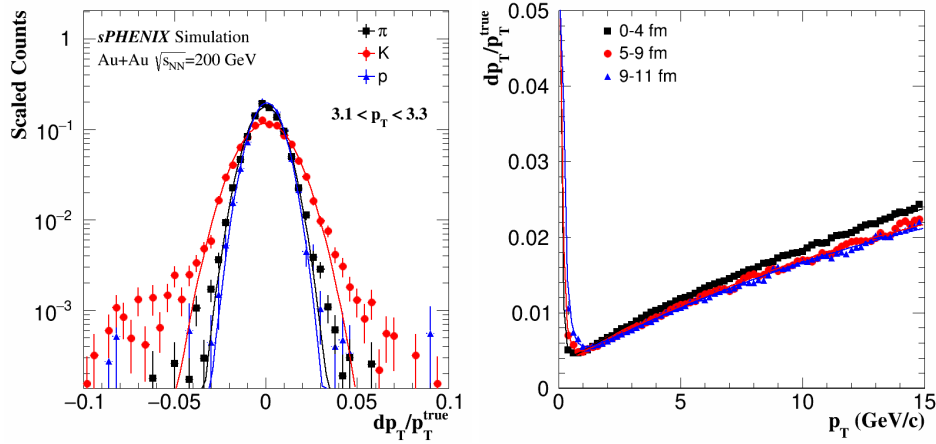
Fig. 6.8   Momentum resolution of K/p/π in this simulation. p_T^{true} is Monte Carlo p_T and dp_T is the difference between MC p_T and reconstructed p_T.

Although model calculations based on coalescence mechanism all predict an enhancement at $3 < p_T < 6$ GeV/c, different models still have large difference at p_T< 3 GeV/c. Furthermore, current experiment measurements of Λ_c^+ spectra at 200 GeV is limited with only 3 p_T bins at 10-80% centrality. To have a better estimation of Λ_c^+ spectra, we combine model calculations with experiment data. Firstly, the Λ_c^+ p_T spectra shape is estimated by $\Lambda_c^+/D^0 \times D^0$ spectra. Λ_c^+/D^0 curves are taken using the average calculation from the following models: Ko: di-quark [173], Ko: three-quark [163], Greco [174], Tshingua [165]. The input D^0 spectra is from STAR at 10-80% centrality, shown in Fig. 6.9 [83]. Then we take Λ_c^+ spectra shapes above to fit the STAR data points to get the model fitted spectrum. The final Λ_c^+ spectra at 10-80% centrality is calculated by taking the mean value of various models fitted spectrum. To scale the Λ_c^+ spectra to a certain centrality, we consider two kinds of weights.

The first weight is the Λ_c^+/D^0 ratio. The Λ_c^+/D^0 ratios as a function of $<N_{part}>$ measured by the STAR Collaboration in $3 < p_T < 6$ GeV/c in 3 centralities are fitted with a quadratic function. The Λ_c^+/D^0 in certain centrality can be interpolated with the fitted function:

$$w_1 = \frac{\Lambda_c^+/D^0(< N_{part} > \text{ at certain centrality})}{\Lambda_c^+/D^0(< N_{part} > \text{ at } 10 - 80\%)} \tag{6.3}$$

0-10%	10-20%	20-40%	40-60%	60-80%
1.37	1.3	1.12	0.89	0.74

Table 6.1   Weights for the centrality dependence of Λ_c^+/D^0 (w_1).

Second is the centrality dependence of D^0 yield. We take the integral yield of D^0 at $2<p_T<10$GeV/c as the reference for the reweighting:

$$w_2 = \frac{\text{Integral yield of D}^0 \text{ at } 2 < p_T < 10 \text{ GeV}/c \text{ at certain centrality}}{\text{Integral yield of D}^0 \text{ at } 2 < p_T < 10\text{GeV}/c \text{ at } 10 - 80\%)} \tag{6.4}$$

The weighting factors for different centrality bins are listed in Table 6.1 and Table 6.2. We combine Λ_c^+ and Λ_c^- statistics together, and assume their yields are the same, so the total weight is $w^{tot} = 2w_1w_2 \times$ branch ratio.

0-10%	10-20%	20-40%	40-60%	60-80%
4.12	2.74	1.51	0.51	0.11

Table 6.2   Weights for the centrality dependence of D^0 spectra (w_2).
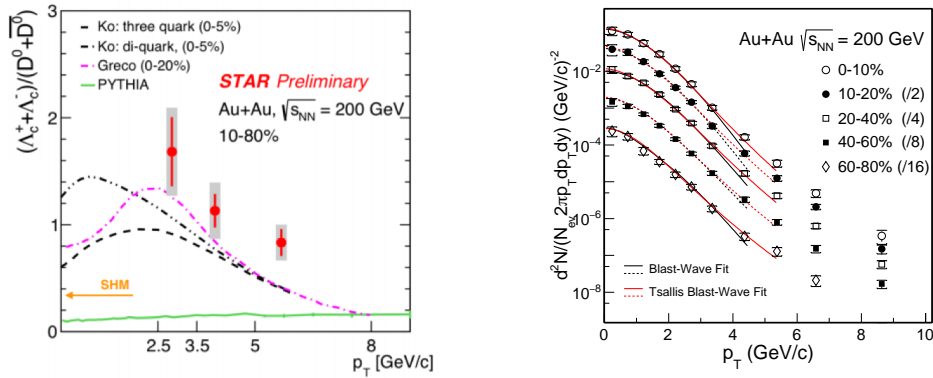
(a) Λ_c^+/D^0 as funcion as p_T in 10-80% cen-
trality measured by STAR.

(b) D^0 spectra in different centralities mea-
sured by STAR.

Fig. 6.9 Λ_c^+ spectra is calculated by multiplying Λ_c^+/D^0 ratio with D^0 spectra. Λ_c^+/D^0 ratio is gotten by fitting data points from STAR with model calculations.

(a) Λ_c^+/D^0 ratio versus $\langle N_{part} \rangle$ measured by STAR.

(b) Λ_c^+/D^0 ratio versus $\langle N_{part} \rangle$ is fitted with a quadratic function.
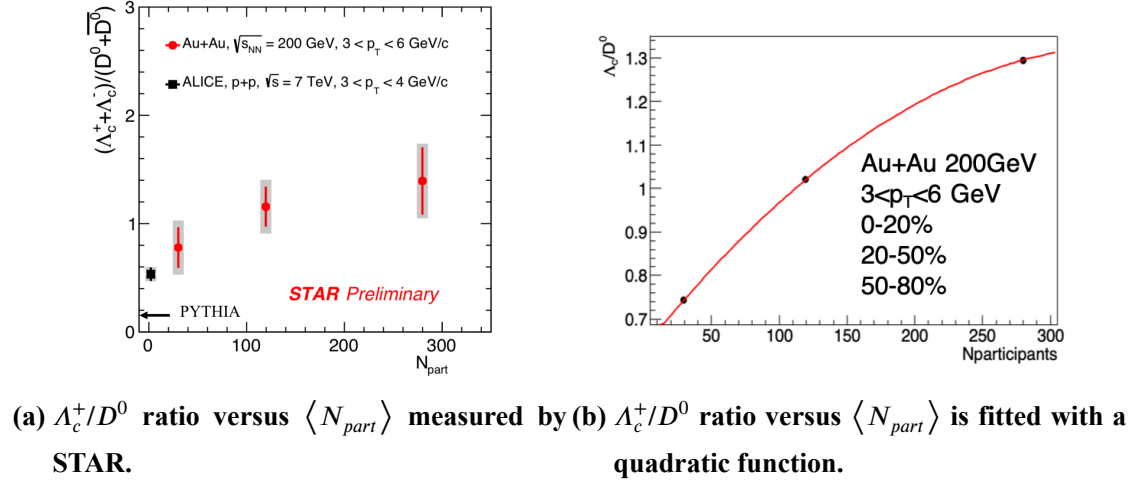
Fig. 6.10 Λ_c^+/D^0 ratio as function as $\langle N_{part} \rangle$.

6.3.5   Combinatorial background

The combinatorial background is estimated from random combination of identified particles (π/K/p). We consider the combination from both primary and secondary tracks. For primary tracks generation:

1. Before running the fast simulation, we extract 3 dimensional distribution of the number of π versus that of K and p in a Au+Au event generated by HIJING, because the yields of identified particles in one event are correlated. These will be used as the input for fast simulation.

2. Sample the number of π/K/p in each event from the distribution above.

3. Sample the uniform η distribution for primary π/K/p. The particles p_T are sampled according to the p_T spectra from STAR and PHENIX measurements [175-177], shown in Fig. 6.11.

For the secondary tracks, we consider π/K/p from charm decay as the first order contribution. We embed a PYTHIA event generator in the track generation process. A p+p event will be generated, and only tracks from charm hadron decay will be selected as candidate tracks for the combinatorial background. To scale the charm production cross section from PYTHIA event to Au+Au events, we take D^0 production yield as the reference. The weight for these secondary tracks are calculated as:

$$w_{sec} = \frac{D^0 \text{ yield } (2 < p_T < 10 \text{GeV/c}) \text{ in PYTHIA8}}{D^0 \text{ yield } (2 < p_T < 10 \text{GeV/c}) \text{ in + Au + Au}} \tag{6.5}$$

Fig. 6.12 shows the D^0 spectra in PYTHIA p+p event after scaling to Au+Au collision at 60-80% centrality. The secondary tracks will be mixed with primary tracks generated above. In later-on reconstruction process, if all the three daughter tracks are secondary

tracks and they come from the same mother Λ_c^+ decay, we will discard this combination.
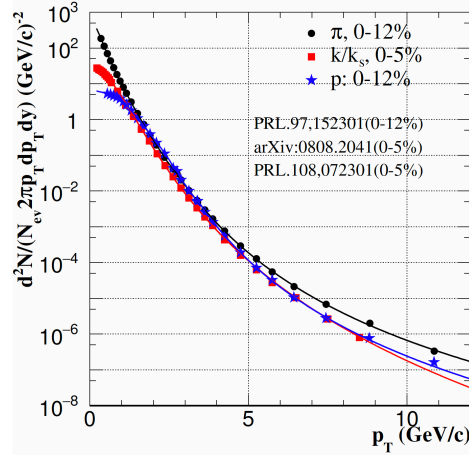
Fig. 6.11   **The primary tracks p_T distribution in this simulation are sampled from identified particle spectrum in Au+Au 200 GeV collisions measured by STAR and PHENIX[175-177].**
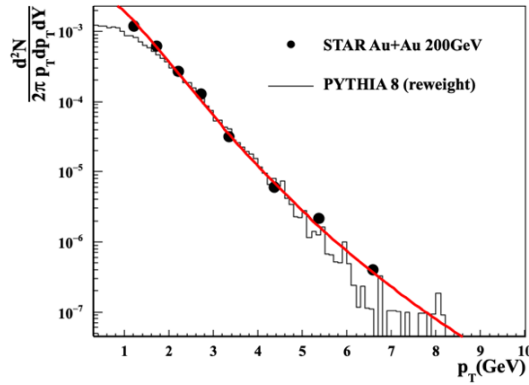
Fig. 6.12   **The black line is D^0 spectra in PYTHIA event after scaling while the data point is that in Au+Au collision at 60-80% centrality from STAR measurements.**

After the background track generation, next step is to apply detector response on these tracks, and then reconstruct combinatorial background (Λ_c^+) candidates. To estimate the contribution of charm decay daughters to the total combinatorial backgrounds, let's define "charm backgrounds" as the background candidates which have more than one track that is from charm hadrons decay. Fig. 6.13 shows the relative fraction of charm backgrounds in the total combinatorial backgrounds. Fig. 6.13 illustrates that charm decay daughters make large contribution to the combinatorial backgrounds at high p_T. This is because charm spectra is harder than the light hadron spectra. While at low p_T due to the large contribution from light flavor particles, charm decay daughter contributions are negligible.
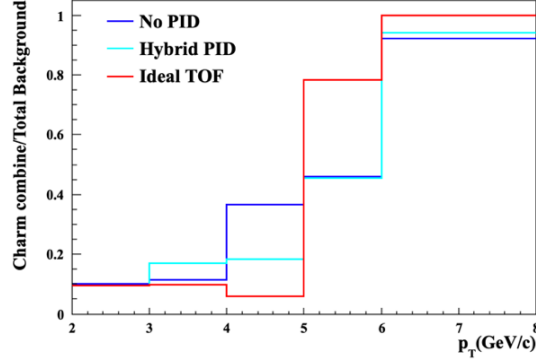
Fig. 6.13   The fraction of the backgrounds with at least one charm decay daughter in the total background ratio at 0-80% centrality.

6.3.6   PID scenario

Currently, sPHENX day-1 detector set up does not contain a specific PID detector. But it still has a 10cm gap reserved between TPC and EMC for possible particle identification detector (e.g. a TOF detector) upgrade in the future. So we consider 4 particle identification (PID) scenarios:

1. "No PID": Suppose the whole detector system have no ability to distinguish $K/\pi/p$.

2. "Clean PID": Particles can be identified at low p_T if the particle is accepted by TOF, while the detector have no PID ability at high p_T. TOF matching efficiency is defined by the fraction of tracks with valid TOF information in total TPC tracks. We assume that the TOF performance is the same as STAR TOF detector, also shown in Fig. 6.14 [83]:
    - K/π can be separated up to 1.6 GeV/c while protons is up to 3 GeV/c. It requires the time resolution of TOF detector is about 30 ps.
    - The TOF matching efficiency is the same as STAR, about 58%.

3. "Hybrid PID": This kind of PID cut is commonly used in the real data analysis to enhance statistics. We require TOF PID if the track have valid TOF informatiion; otherwise there is no PID cut.

4. "Ideal TOF PID": Similar as 2, but assume that the TOF acceptance is ideal with 100% TOF matching efficiency.

6.3.7 Λ_c^+ reconstruction

Λ_c^+ life time is short $c\tau = 59.9\ \mu$m [10]. The MVTX detector in the tracking system enables the measurements of Λ_c^+ baryon via the precise secondary vertex reconstruction.
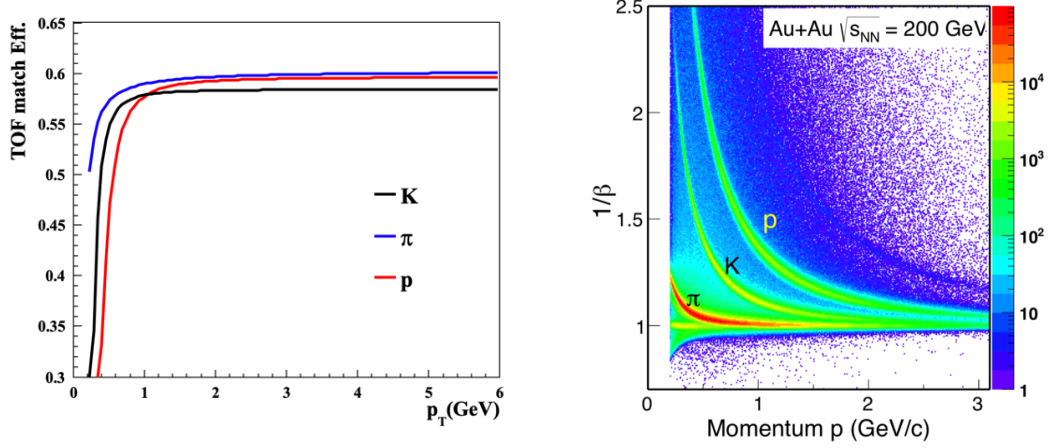
(a) TOF matching efficiency used in this simulation, which is also taken from STAR performance.

(b) STAR $1/\beta$ distribution versus p_T [83]. The band for $K/\pi/p$ can be seen cearly.

Fig. 6.14   TOF detector performance used in this simulation.

Λ_c^+ is reconstructed via the following channel:

$$\Lambda_c^+ \to K^- p \pi^+ \quad 6.23\%$$

$$p\overline{K^*} \quad 1.94\% \times 66.7\%$$

$$K^- \Delta(1232)^{++} \quad 1.07\% \times 99.4\%$$

$$\pi^+ \Lambda(1520) \quad 2.2\% \times 22.5\%$$

$$non-resonant \quad 3.4\%$$

The acceptance cut on single particles is: $p_T > 0.6$ GeV/c and $|\eta| < 1$. The schematic diagram of Λ_c^+ decay topology is shown in Fig. 6.15. The topological variables used for reconstruction are summarized below:

1. gDCA of K/p/π: the distance of closet approach (DCA) of K/π/p tracks to primary vertex (PV).

2. DCA12: The distance of closet approach of each daughter track pairs: $K\pi$, Kp and $p\pi$.

3. decay length: reconstructed Λ_c^+ decay length. For each daughter track pair ($K\pi$, Kp and $p\pi$), we can get the midpoint between their DCA positions. The decay vertex of Λ_c^+ is defined as the geometric average of 3 midpoints.

4. DCA Λ_c^+: The DCA of reconstructed Λ_c^+ track to primary vertex.

5. pointing angle θ: the angle between reconstructed Λ_c^+ track and the line between primary vertex to decay vertex.

As the pointing angle of Λ_c^+ signal is very close to 0, so we set a fix cut on $cos(\theta) >$

110
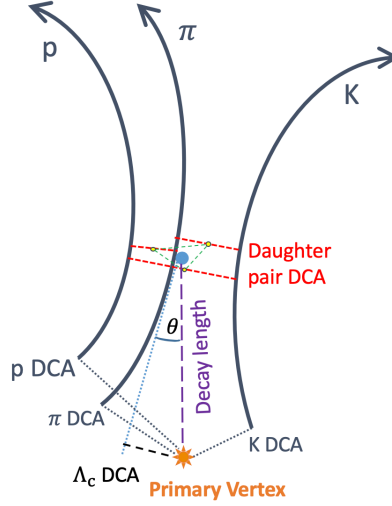
Fig. 6.15   The schematic diagram of Λ_c^+ decay topology.

0.995. We use TMVA package to tune the cuts for topological variables for best signal significance. TMVA tuning rely on appropriate input of signal to background ratio (S/B) to calculate correct significance. S/B strongly depends on centrality and p_T, so we divide in 3 centrality bins: 0-10%, 10-40%, 40-80%, and 3 p_T bins: $[2, 3), [3, 5), [5, 12)$ GeV/c for TMVA training. Besides, we have to treat different PID scenarios separately because PID should be helpful to suppress the background. For the clean PID scenario, we will use the same cuts as "Ideal TOF" scenario because both of them have better S/B than the rest 2 scenarios. We compare two kinds of TMVA methods: rectangle cuts ("CutsSA" in TMVA method) and Boost Decision Tree (BDT) cuts("BDT" in TMVA method). BDT cuts shows slightly improvement on significance compared to rectangle cuts. Actually, one important thing for significance improvement is to tune the cuts with centrality and p_T dependence instead of setting the same cuts on all of the events. After training data and inputting correct signal over background ratio, TMVA will return signal and background efficiency as well as significance as function as cuts applied on evaluated BDT value. An example of TMVA response with BDT method is shown in Fig. 6.16. The higher cuts on BDT value results in lower signal efficiency.

6.3.8   Results and discussion

We estimate the statistical uncertainty for Λ_c^+ production measurements in the future sPHENIX experiment. The Λ_c^+ signal significance and the signal to background ratio are calculated assuming there are totally 240 billion minimum bias events. In the first step, we generate background and signals with enough statistics for TMVA training. After cuts are determined, we scale the counts of signals and backgrounds within $mass \pm 3\sigma$
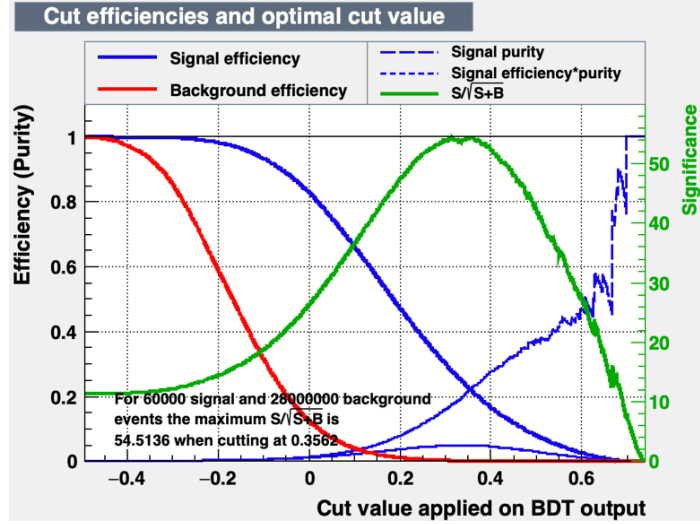
Fig. 6.16   **This plot shows an example of TMVA response with BDT method, such as the background efficiency (red line), signal efficiency (blue line), and estimated significance (green line) as a function of the cuts on the evaluated BDT value.**

to 240B. *mass* and σ are obtained by fitting the signal invariant mass distribution with Gaussian function. The significance is defined as:

$$\text{Significance} = \frac{S}{\sqrt{S+B}} \tag{6.6}$$

Where S is the scaled signal counts and B is the scaled background counts within *mass* $\pm$ 3σ. Fig. 6.18 and Fig. 6.19 show the projected Λ_c^+ invariant mass distributions (signal + background) based on calculated significance under "No PID" senario at minimum bias events and other centralities. The projection procedure is described below:

1. Firstly fit the signal with normalized Gaussian function, and then scale the Gaussian function to 240B events. The background is fitted by a linear function and then do similar scaling as the signal.

2. Combine the signal and background obtained above to generate an expected invariant mass distribution.

3. Resample data point in each invariant mass bin in the expected distribution with Poisson statistics.

The expected significance of Λ_c^+ signal under no PID scenario is 36 in $2 < p_T < 8$ GeV/c at 0-80% centrality. The background is mainly contributed by most central collisions. The projected signal significance and signal to background ratio for future Λ_c^+ measurement at sPHENIX at different centralities are shown in Fig. 6.17, Fig. 6.21 and Fig. 6.22.

As we can see from the plots, with high statistics and better detector performance, precise Λ_c^+ measurement is expected at future sPHENIX experiment. Even supposing
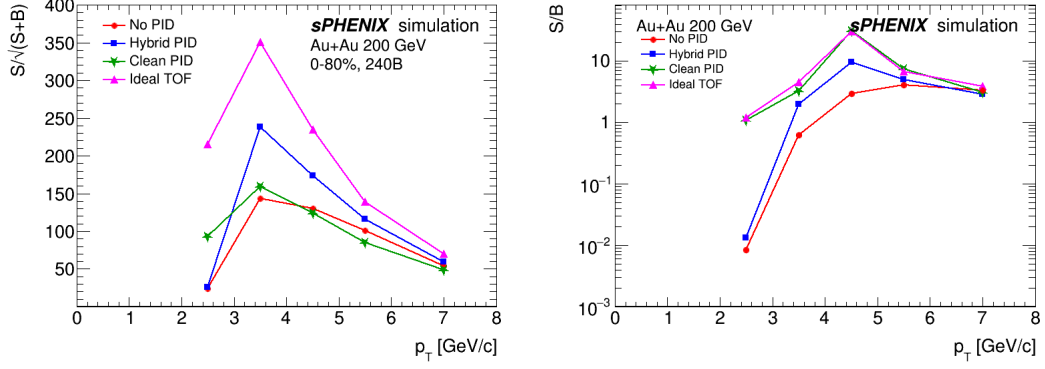
Fig. 6.17   Projected Λ_c^+ invariant mass distribution in minimum bias events under "No PID" scenario. The projection is based on the assumption that we have totally 240 billion minimum bias events.
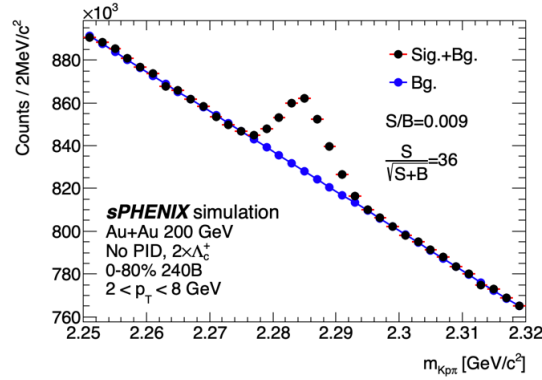
Fig. 6.18   Projected Λ_c invariant mass distribution at 0-80% centrality with total 240 billion events.

that the detector system has no PID ability, the signal significance could reach >20 at 2< p_T <3 GeV/c and > 140 at 3< p_T <4 GeV/c in MB event. Such precision will provide stringent constrain on models calculations, and is helpful for total charm cross section measurements in Au+Au 200 GeV collisions at low p_T. Apart from this, it is also expected to have precise study on the centrality dependence of Λ_c^+ production in the future, such as R_{CP} and Λ_c^+/D^0 vs $<N_{part}>$. The significance of Λ_c^+ signal is around 5 at 2< p_T <3 GeV/c in 0-10% centralty under "No PID" scenario. The S/B ratio is only about 0.003 in this bin, which may introduce sizable systematic uncertainty in the real measurements. The S/B ratio can be improved to 0.45 and the significance would increase to 84 if all daughter particles can be cleanly identified. Fig. 6.20 shows the physics projection plot of Λ_c^+/D^0 at 0-10% centrality. The error bar becomes larger at p_T < 2.5 GeV/c if the detector has no PID ability, while the error bars are small under ideal PID scenario even at low p_T. The PID detector will have a significant improvement to Λ_c^+ measurement particularly at low p_T region.
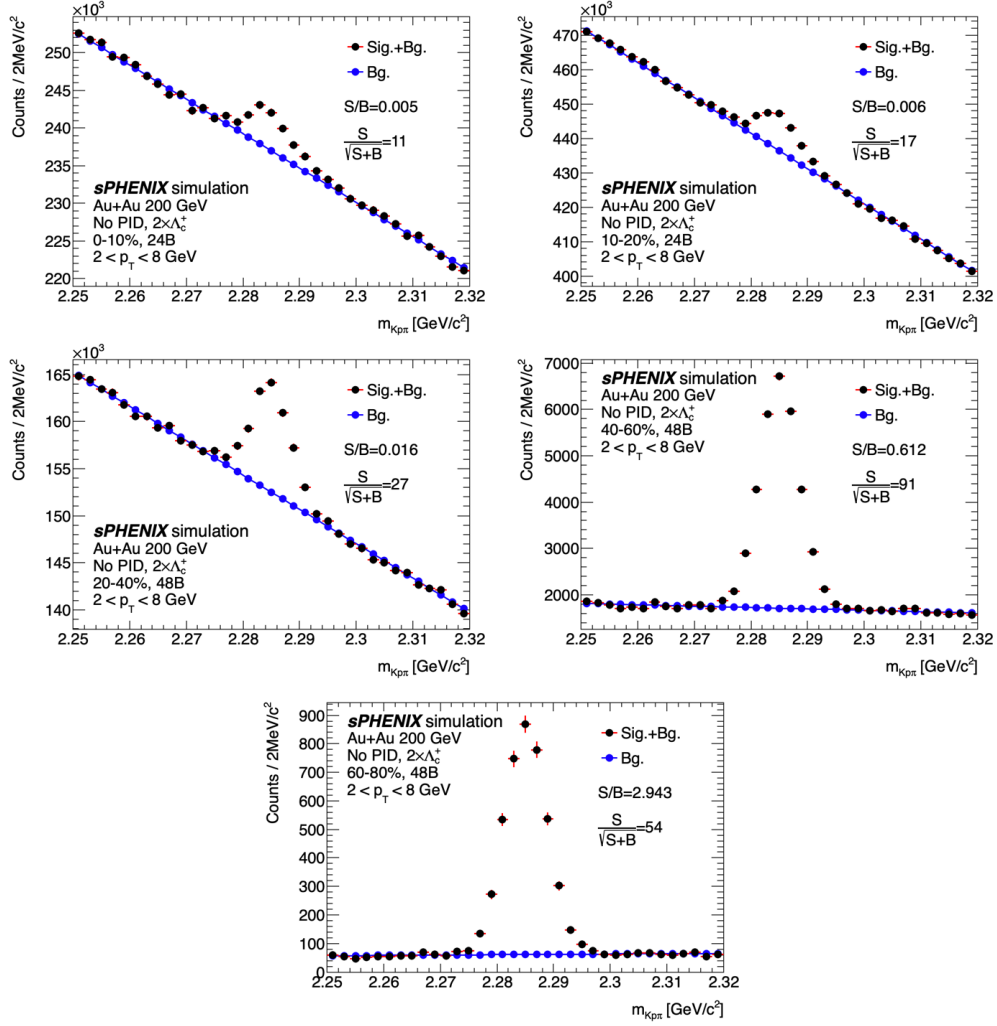
Fig. 6.19   Projected Λ_c^+ invariant mass distribution at different centralities under "No PID" scenario. The projection is assuming that we have totally 240 billion minimum bias events.

6.3.9   Summary

The simulation of Λ_c^+ measurement in Au+Au 200GeV collisions at future sPHENIX is conducted. A hybrid method is used to accelerate the computation process, which combines full Geant4 simulation of the detector and fast simulation package. With high statistics (240B MB events) and good momentum/DCA resolution, Λ_c^+ can be measured precisely by sPHENIX in Au+Au 200 GeV. A PID detector, such as TOF, will be very helpful for low p_T Λ_c^+ measurement in most central collision.
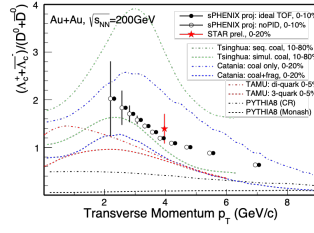
Fig. 6.20   Physics projection plot of Λ_c^+/D^0 at 0-10% centrality and the comparison with model calculations.
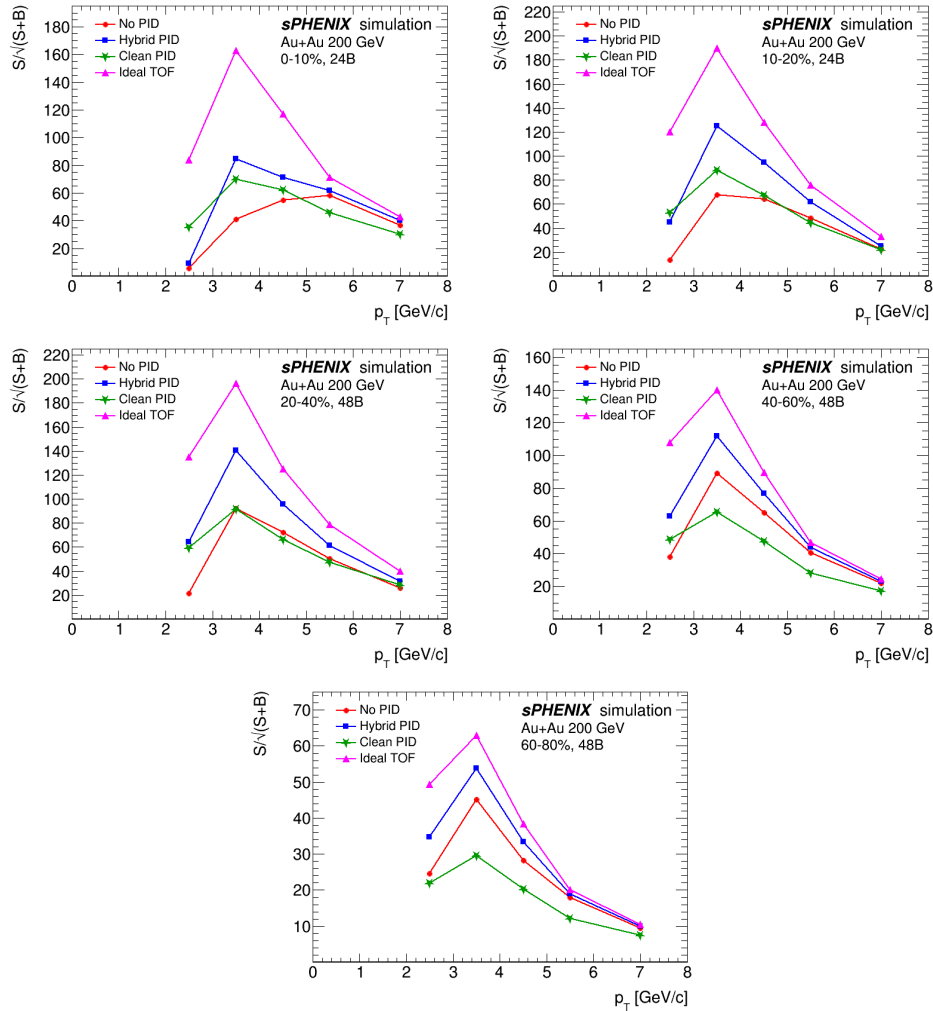
Fig. 6.21   The projected Λ_c^+ signal significance in different centralities under different PID scenarios.

115
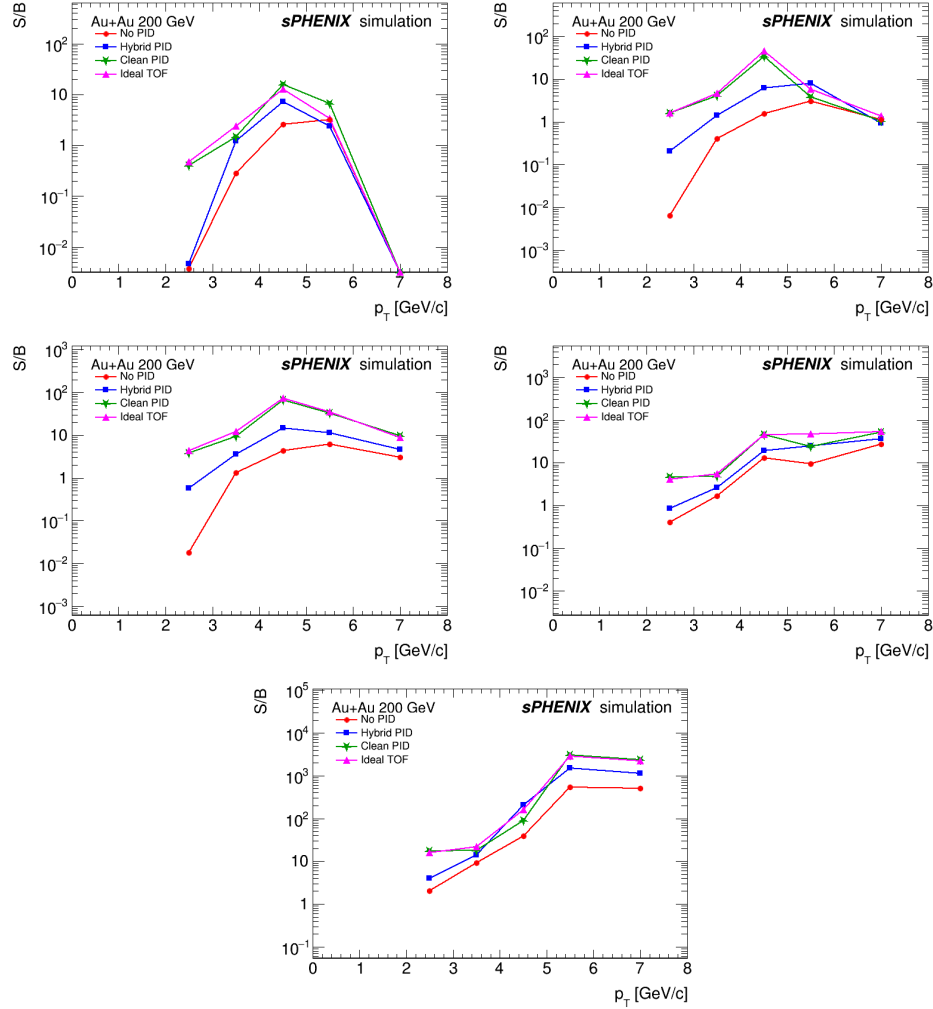
Fig. 6.22   **The projected Λ_c^+ signal to background ratio in different centralities under different PID scenarios.**

Bibliography

[1]   Wikipedia. [EB/OL]. https://commons.wikimedia.org/wiki/File:Standard_Model_of_Eleme
        ntary_Particles.svg.

[2]   HAN M Y, NAMBU Y. Three-triplet model with double SU(3) symmetry[J/OL]. Phys. Rev.,
        1965, 139:B1006-B1010. https://link.aps.org/doi/10.1103/PhysRev.139.B1006.

[3]   GELL-MANN M. Quarks[J/OL]. Acta Phys. Austriaca Suppl., 1972, 9:733-761. DOI:
        10.1007/978-3-7091-4034-5_20.

[4]   FRITZSCH H, GELL-MANN M. Current algebra: Quarks and what else?[J]. eConf, 1972,
        C720906V2:135-165.

[5]   SALAM G P. Elements of QCD for hadron colliders[C]//2009 European School of High-
        Energy Physics. 2010.

[6]   SKANDS P. Introduction to QCD[C/OL]//Theoretical Advanced Study Institute in Elemen-
        tary Particle Physics: Searching for New Physics at Small and Large Scales. 2017: 63-124.
        DOI: 10.1142/9789814525220_0008.

[7]   PICH A. Quantum chromodynamics[C]//1994 European School of High-energy Physics.
        1995: 157-207.

[8]   BRUECKNER K A. Meson-Nucleon Scattering and Nucleon Isobars[J/OL]. Phys. Rev.,
        1952, 86:106-109. DOI: 10.1103/PhysRev.86.106.

[9]   "十一五" 国家重点图书: 核与粒子物理导论[M/OL]. 中国科学技术大学出版社, 2009.
        https://press.ustc.edu.cn/book/1577.

[10]   Particle Data Group. Review of Particle Physics 2018[J/OL]. Phys. Rev. D, 2018, 98:030001.
        https://link.aps.org/doi/10.1103/PhysRevD.98.030001.

[11]   Particle Data Group. Review of Particle Physics 2020[J/OL]. Prog. Theor. Exp. Phys., 2020,
        2020:083c01. https://link.aps.org/doi/10.1103/PhysRevD.98.030001.

[12]   COLLINS J C, SOPER D E, STERMAN G F. Factorization of Hard Processes in QCD:
        volume 5[M/OL]. 1989: 1-91. DOI: 10.1142/9789814503266_0001.

[13]   FRIES R, NONAKA C. Evaluating Results from the Relativistic Heavy Ion Collider with
        Perturbative QCD and Hydrodynamics[J/OL]. Prog. Part. Nucl. Phys., 2011, 66:607-660.
        DOI: 10.1016/j.ppnp.2010.12.001.

[14]   STERMAN G, SMITH J, COLLINS J C, et al. Handbook of perturbative qcd[J/OL]. Rev.
        Mod. Phys., 1995, 67:157-248. https://link.aps.org/doi/10.1103/RevModPhys.67.157.

[15]   GUPTA R. Introduction to lattice QCD: Course[C]//Les Houches Summer School in The-
        oretical Physics, Session 68: Probing the Standard Model of Particle Interactions. 1997:

83-219.

[16] YAGI K, HATSUDA T, MIAKE Y. Quark-gluon plasma: From big bang to little bang: volume 23[M]. 2005.

[17] CAINES H. The Search for Critical Behavior and Other Features of the QCD Phase Diagram – Current Status and Future Prospects[J/OL]. Nuclear Physics A, 2017, 967: 121 - 128. http://www.sciencedirect.com/science/article/pii/S0375947417302580. DOI: https://doi.org/10.1016/j.nuclphysa.2017.05.116.

[18] BUSZA W, RAJAGOPAL K, VAN DER SCHEE W. Heavy Ion Collisions: The Big Picture, and the Big Questions[J/OL]. Ann. Rev. Nucl. Part. Sci., 2018, 68:339-376. DOI: 10.1146/annurev-nucl-101917-020852.

[19] BAZAVOV A, BHATTACHARYA T, DETAR C, et al. Equation of state in $(2 + 1)$-flavor qcd[J/OL]. Phys. Rev. D, 2014, 90:094503. https://link.aps.org/doi/10.1103/PhysRevD.90.094503.

[20] COLLABORATION S. Studying the Phase Diagram of QCD Matter at RHIC[EB/OL]. https://drupal.star.bnl.gov/STAR/starnotes/public/sn0598.

[21] ALFORD M G, SCHMITT A, RAJAGOPAL K, et al. Color superconductivity in dense quark matter[J/OL]. Rev. Mod. Phys., 2008, 80:1455-1515. DOI: 10.1103/RevModPhys.80.1455.

[22] MILLER M L, REYGERS K, SANDERS S J, et al. Glauber modeling in high energy nuclear collisions[J/OL]. Ann. Rev. Nucl. Part. Sci., 2007, 57:205-243. DOI: 10.1146/annurev.nucl.57.090506.123020.

[23] BJORKEN J. Highly Relativistic Nucleus-Nucleus Collisions: The Central Rapidity Region [J/OL]. Phys. Rev. D, 1983, 27:140-151. DOI: 10.1103/PhysRevD.27.140.

[24] SORENSEN P. Elliptic Flow: A Study of Space-Momentum Correlations In Relativistic Nuclear Collisions[M/OL]. 2010: 323-374. DOI: 10.1142/9789814293297_0006.

[25] SCHLICHTING S, TEANEY D. The First fm/c of Heavy-Ion Collisions[J/OL]. Ann. Rev. Nucl. Part. Sci., 2019, 69:447-476. DOI: 10.1146/annurev-nucl-101918-023825.

[26] TEANEY D A. Viscous Hydrodynamics and the Quark Gluon Plasma[M/OL]. 2010: 207-266. DOI: 10.1142/9789814293297_0004.

[27] GELIS F, IANCU E, JALILIAN-MARIAN J, et al. The Color Glass Condensate[J/OL]. Ann. Rev. Nucl. Part. Sci., 2010, 60:463-489. DOI: 10.1146/annurev.nucl.010909.083629.

[28] ROMATSCHKE P, ROMATSCHKE U. Viscosity Information from Relativistic Nuclear Collisions: How Perfect is the Fluid Observed at RHIC?[J/OL]. Phys. Rev. Lett., 2007, 99: 172301. DOI: 10.1103/PhysRevLett.99.172301.

[29] LUZUM M, ROMATSCHKE P. Conformal relativistic viscous hydrodynamics: Applications to rhic results at $\sqrt{s_{NN}} = 200$ gev[J/OL]. Phys. Rev. C, 2008, 78:034915. https://link.aps.o

rg/doi/10.1103/PhysRevC.78.034915.

[30] SCHENKE B, JEON S, GALE C. Elliptic and triangular flow in event-by-event (3+1)D viscous hydrodynamics[J/OL]. Phys. Rev. Lett., 2011, 106:042301. DOI: 10.1103/Phys-RevLett.106.042301.

[31] ADAMS J, et al. Azimuthal Anisotropy at the Relativistic Heavy Ion Collider: The First and Fourth Harmonics[J/OL]. Phys. Rev. Lett., 2004, 92:062301. https://link.aps.org/doi/10.1103/PhysRevLett.92.062301.

[32] ALVER B, et al. Event-by-Event Fluctuations of Azimuthal Particle Anisotropy in Au + Au Collisions at $\sqrt{s_{NN}}$ = 200 GeV[J/OL]. Phys. Rev. Lett., 2010, 104:142301. DOI: 10.1103/PhysRevLett.104.142301.

[33] HEINZ U, SNELLINGS R. Collective flow and viscosity in relativistic heavy-ion collisions [J/OL]. Ann. Rev. Nucl. Part. Sci., 2013, 63:123-151. DOI: 10.1146/annurev-nucl-102212-170540.

[34] BASS S, et al. Microscopic models for ultrarelativistic heavy ion collisions[J/OL]. Prog. Part. Nucl. Phys., 1998, 41:255-369. DOI: 10.1016/S0146-6410(98)00058-1.

[35] NARA Y, OTUKA N, OHNISHI A, et al. Relativistic nuclear collisions at 10A GeV energies from p + Be to Au+Au with the hadronic cascade model[J/OL]. Phys. Rev. C, 1999, 61: 024901. https://link.aps.org/doi/10.1103/PhysRevC.61.024901.

[36] ACKERMANN K, et al. Elliptic flow in Au + Au collisions at $\sqrt{s_{NN}}$ = 130 GeV[J/OL]. Phys. Rev. Lett., 2001, 86:402-407. DOI: 10.1103/PhysRevLett.86.402.

[37] STAR, PHENIX, PHOBOS and BRAHMS. First Three Years of Operation of RHIC[J]. Nuclear Physics A, 2005, 757(1):1 - 283.

[38] ADAMS J, et al. Particle type dependence of azimuthal anisotropy and nuclear modification of particle production in Au + Au collisions at $\sqrt{s_{NN}}$ = 200 GeV[J/OL]. Phys. Rev. Lett., 2004, 92:052302. DOI: 10.1103/PhysRevLett.92.052302.

[39] ADAMS J, et al. Multi-strange baryon elliptic flow in Au + Au collisions at $\sqrt{s_{NN}}$ = 200 GeV[J/OL]. Phys. Rev. Lett., 2005, 95:122301. DOI: 10.1103/PhysRevLett.95.122301.

[40] ABELEV B, et al. Centrality dependence of charged hadron and strange hadron elliptic flow from $\sqrt{s_{NN}}$ = 200 GeV Au + Au collisions[J/OL]. Phys. Rev. C, 2008, 77:054901. DOI: 10.1103/PhysRevC.77.054901.

[41] ADLER S, et al. Elliptic flow of identified hadrons in Au+Au collisions at $\sqrt{s_{NN}}$ = 200 GeV [J/OL]. Phys. Rev. Lett., 2003, 91:182301. DOI: 10.1103/PhysRevLett.91.182301.

[42] ABELEV B, et al. Mass, quark-number, and $\sqrt{s_{NN}}$ dependence of the second and fourth flow harmonics in ultra-relativistic nucleus-nucleus collisions[J/OL]. Phys. Rev. C, 2007, 75:054906. DOI: 10.1103/PhysRevC.75.054906.

[43] FRIES R J, GRECO V, SORENSEN P. Coalescence Models For Hadron Formation From Quark Gluon Plasma[J/OL]. Ann. Rev. Nucl. Part. Sci., 2008, 58:177-205. DOI: 10.1146/annurev.nucl.58.110707.171134.

[44] MOLNAR D, VOLOSHIN S A. Elliptic flow at large transverse momenta from quark coalescence[J/OL]. Phys. Rev. Lett., 2003, 91:092301. DOI: 10.1103/PhysRevLett.91.092301.

[45] LIN Z W, KO C. Flavor ordering of elliptic flows at high transverse momentum[J/OL]. Phys. Rev. Lett., 2002, 89:202302. DOI: 10.1103/PhysRevLett.89.202302.

[46] SHUKLA P. Glauber model for heavy ion collisions from low energies to high energies[J].

[47] KOPELIOVICH B Z, NEMCHIK J, SCHÄFER A, et al. Cronin effect in hadron production off nuclei[J/OL]. Phys. Rev. Lett., 2002, 88:232303. https://link.aps.org/doi/10.1103/PhysRevLett.88.232303.

[48] ACCARDI A, GYULASSY M. Cronin effect versus geometrical shadowing in d + Au collisions at RHIC[J/OL]. Phys. Lett. B, 2004, 586:244-253. DOI: 10.1016/j.physletb.2004.02.020.

[49] AGGARWAL M, et al. Transverse mass distributions of neutral pions from Pb-208 induced reactions at 158-A-GeV[J/OL]. Eur. Phys. J. C, 2002, 23:225-236. DOI: 10.1007/s100520100886.

[50] D'ENTERRIA D G. Indications of suppressed high p(T) hadron production in nucleus - nucleus collisions at CERN-SPS[J/OL]. Phys. Lett. B, 2004, 596:32-43. DOI: 10.1016/j.physletb.2004.06.071.

[51] ADARE A, et al. Neutral pion production with respect to centrality and reaction plane in Au+Au collisions at $\sqrt{s_{NN}}$=200 GeV[J/OL]. Phys. Rev. C, 2013, 87(3):034911. DOI: 10.1103/PhysRevC.87.034911.

[52] CHATRCHYAN S, et al. Study of high-pT charged particle suppression in PbPb compared to pp collisions at $\sqrt{s_{NN}} = 2.76$ TeV[J/OL]. Eur. Phys. J. C, 2012, 72:1945. DOI: 10.1140/epjc/s10052-012-1945-x.

[53] ABELEV B, et al. Centrality Dependence of Charged Particle Production at Large Transverse Momentum in Pb–Pb Collisions at $\sqrt{s_{NN}} = 2.76$ TeV[J/OL]. Phys. Lett. B, 2013, 720:52-62. DOI: 10.1016/j.physletb.2013.01.051.

[54] AAD G, et al. Measurement of charged-particle spectra in Pb+Pb collisions at $\sqrt{s_{NN}} = 2.76$ TeV with the ATLAS detector at the LHC[J/OL]. JHEP, 2015, 09:050. DOI: 10.1007/JHEP09(2015)050.

[55] KHACHATRYAN V, et al. Charged-particle nuclear modification factors in PbPb and pPb collisions at $\sqrt{s_{NN}} = 5.02$ TeV[J/OL]. JHEP, 2017, 04:039. DOI: 10.1007/JHEP04(2017)039.

[56] ADAMS J, et al. Evidence from d + Au measurements for final state suppression of high p(T) hadrons in Au+Au collisions at RHIC[J/OL]. Phys. Rev. Lett., 2003, 91:072304. DOI: 10.1103/PhysRevLett.91.072304.

[57] ADAMS J, et al. Transverse momentum and collision energy dependence of high p(T) hadron suppression in Au+Au collisions at ultrarelativistic energies[J/OL]. Phys. Rev. Lett., 2003, 91:172302. DOI: 10.1103/PhysRevLett.91.172302.

[58] LÉVAI P, MÜLLER B, WANG X N. Open charm production in an equilibrating parton plasma[J/OL]. Phys. Rev. C, 1995, 51:3326-3335. https://link.aps.org/doi/10.1103/PhysRev C.51.3326.

[59] LÉVAI P, VOGT R. Thermal charm production by massive gluons and quarks[J/OL]. Phys. Rev. C, 1997, 56:2707-2717. https://link.aps.org/doi/10.1103/PhysRevC.56.2707.

[60] RAPP R, VAN HEES H. Heavy Quarks in the Quark-Gluon Plasma[C/OL]//2010: 111-206. DOI: 10.1142/9789814293297_0003.

[61] SVETITSKY B. Diffusion of charmed quarks in the quark-gluon plasma[J/OL]. Phys. Rev. D, 1988, 37:2484-2491. DOI: 10.1103/PhysRevD.37.2484.

[62] MOORE G D, TEANEY D. How much do heavy quarks thermalize in a heavy ion collision? [J/OL]. Phys. Rev. C, 2005, 71:064904. DOI: 10.1103/PhysRevC.71.064904.

[63] CAO S, QIN G Y, BASS S A. Heavy-quark dynamics and hadronization in ultrarelativistic heavy-ion collisions: Collisional versus radiative energy loss[J/OL]. Phys. Rev. C, 2013, 88: 044907. DOI: 10.1103/PhysRevC.88.044907.

[64] DONG X, LEE Y J, RAPP R. Open Heavy-Flavor Production in Heavy-Ion Collisions[J/OL]. Ann. Rev. Nucl. Part. Sci., 2019, 69:417-445. DOI: 10.1146/annurev-nucl-101918-023806.

[65] ADAMCZYK L, et al. Measurement of D^0 Azimuthal Anisotropy at Midrapidity in Au+Au Collisions at $\sqrt{s_{NN}}$=200 GeV[J]. Phys. Rev. Lett., 2017, 118(21):212301.

[66] BANERJEE D, DATTA S, GAVAI R, et al. Heavy quark momentum diffusion coefficient from lattice qcd[J/OL]. Phys. Rev. D, 2012, 85:014510. https://link.aps.org/doi/10.1103/Phy sRevD.85.014510.

[67] DING H T, FRANCIS A, KACZMAREK O, et al. Charmonium properties in hot quenched lattice qcd[J/OL]. Phys. Rev. D, 2012, 86:014509. https://link.aps.org/doi/10.1103/PhysRev D.86.014509.

[68] KACZMAREK O. Continuum estimate of the heavy quark momentum diffusion coefficient κ[J/OL]. Nucl. Phys. A, 2014, 931:633-637. DOI: 10.1016/j.nuclphysa.2014.09.031.

[69] VAN HEES H, RAPP R. Thermalization of heavy quarks in the quark-gluon plasma[J/OL]. Phys. Rev. C, 2005, 71:034907. DOI: 10.1103/PhysRevC.71.034907.

[70] HAMBROCK R, HOROWITZ W. AdS/CFT predictions for azimuthal and momentum cor-

relations of $b\bar{b}$ pairs in heavy ion collisions[J/OL]. Nucl. Part. Phys. Proc., 2017, 289-290: 233-236. DOI: 10.1016/j.nuclphysbps.2017.05.052.

[71] DAS S K, SCARDINA F, PLUMARI S, et al. Toward a solution to the R_{AA} and v_2 puzzle for heavy quarks[J/OL]. Phys. Lett. B, 2015, 747:260-264. DOI: 10.1016/j.physletb.2015.06.003.

[72] XU Y, BERNHARD J E, BASS S A, et al. Data-driven analysis for the temperature and momentum dependence of the heavy-quark diffusion coefficient in relativistic heavy-ion collisions[J/OL]. Phys. Rev. C, 2018, 97:014907. https://link.aps.org/doi/10.1103/PhysRevC.97.014907.

[73] RIEK F, RAPP R. Quarkonia and heavy-quark relaxation times in the quark-gluon plasma [J/OL]. Phys. Rev. C, 2010, 82:035201. https://link.aps.org/doi/10.1103/PhysRevC.82.035 201.

[74] HE M, FRIES R J, RAPP R. Modifications of heavy-flavor spectra in $\sqrt{s_{NN}} = 62.4$ gev au-au collisions[J/OL]. Phys. Rev. C, 2015, 91:024904. https://link.aps.org/doi/10.1103/PhysRevC.91.024904.

[75] L. ADAMCZYK J A. Elliptic flow of electrons from heavy-flavor hadron decays in Au + Au collisions at $\sqrt{s_{NN}} = 200$, 62.4, and 39 GeV[J]. Phys. Rev. C, 2017, 95:034907.

[76] DOKSHITZER Y L, KHARZEEV D. Heavy quark colorimetry of QCD matter[J/OL]. Phys. Lett. B, 2001, 519:199-206. DOI: 10.1016/S0370-2693(01)01130-3.

[77] ARMESTO N, SALGADO C A, WIEDEMANN U A. Medium induced gluon radiation off massive quarks fills the dead cone[J/OL]. Phys. Rev. D, 2004, 69:114003. DOI: 10.1103/PhysRevD.69.114003.

[78] BUZZATTI A, GYULASSY M. Jet flavor tomography of quark gluon plasmas at rhic and lhc[J/OL]. Phys. Rev. Lett., 2012, 108:022301. https://link.aps.org/doi/10.1103/PhysRevLett.108.022301.

[79] ADLER S, et al. Nuclear modification of electron spectra and implications for heavy quark energy loss in Au+Au collisions at $\sqrt{s_{NN}}$=200 GeV[J/OL]. Phys. Rev. Lett., 2006, 96: 032301. DOI: 10.1103/PhysRevLett.96.032301.

[80] ADARE A, et al. Energy Loss and Flow of Heavy Quarks in Au+Au Collisions at s(NN)**(1/2) = 200-GeV[J/OL]. Phys. Rev. Lett., 2007, 98:172301. DOI: 10.1103/PhysRevLett.98.172301.

[81] ABELEV B, et al. Transverse momentum and centrality dependence of high-p_T non-photonic electron suppression in Au+Au collisions at $\sqrt{s_{NN}} = 200$ GeV[J/OL]. Phys. Rev. Lett., 2007, 98:192301. DOI: 10.1103/PhysRevLett.98.192301.

[82] ADAMCZYK L, et al. Observation of D^0 Meson Nuclear Modifications in Au+Au Collisions

at $\sqrt{s_{NN}} = 200$ GeV[J]. Phys. Rev. Lett., 2014, 113:142301.

[83] ADAM J, et al. Centrality and transverse momentum dependence of D^0-meson production at mid-rapidity in Au+Au collisions at $\sqrt{s_{NN}} = 200\,GeV$[J]. Phys. Rev. C, 2019, 99(3): 034908.

[84] ADAM J, ADAMCZYK L, ADAMS J R, et al. Centrality and transverse momentum dependence of D^0-meson production at mid-rapidity in Au + Au collisions at $\sqrt{s_{NN}} = 200$ GeV [J/OL]. Phys. Rev. C, 2019, 99:034908. https://link.aps.org/doi/10.1103/PhysRevC.99.034 908.

[85] ADAM J, et al. Transverse momentum dependence of D-meson production in Pb-Pb collisions at $\sqrt{s_{NN}} = 2.76$ TeV[J/OL]. JHEP, 2016, 03:081. DOI: 10.1007/JHEP03(2016)081.

[86] ABELEV B, et al. Energy dependence of pi+-, p and anti-p transverse momentum spectra for Au+Au collisions at s(NN)**(1/2) = 62.4 and 200-GeV[J/OL]. Phys. Lett. B, 2007, 655: 104-113. DOI: 10.1016/j.physletb.2007.06.035.

[87] ABELEV B, et al. Centrality Dependence of Charged Particle Production at Large Transverse Momentum in Pb–Pb Collisions at $\sqrt{s_{NN}} = 2.76$ TeV[J/OL]. Phys. Lett. B, 2013, 720:52-62. DOI: 10.1016/j.physletb.2013.01.051.

[88] LETESSIER J, RAFELSKI J. Hadron production and phase changes in relativistic heavy ion collisions[J/OL]. Eur. Phys. J. A, 2008, 35:221-242. DOI: 10.1140/epja/i2007-10546-7.

[89] HE M, FRIES R J, RAPP R. D_s-Meson as Quantitative Probe of Diffusion and Hadronization in Nuclear Collisions[J/OL]. Phys. Rev. Lett., 2013, 110(11):112301. DOI: 10.1103/PhysRevLett.110.112301.

[90] ADARE A, et al. An Upgrade Proposal from the PHENIX Collaboration[J]. 2015.

[91] EIC white paper. [EB/OL]. https://www.bnl.gov/npp/docs/EIC_White_Paper_Final.pdf.

[92] The Electron-Ion Collider. [EB/OL]. https://www.bnl.gov/eic/.

[93] HAHN H, et al. The RHIC design overview[J/OL]. Nucl. Instrum. Meth. A, 2003, 499: 245-263. DOI: 10.1016/S0168-9002(02)01938-1.

[94] HARRISON M, PEGGS S G, ROSER T. The RHIC accelerator[J/OL]. Ann. Rev. Nucl. Part. Sci., 2002, 52:425-469. DOI: 10.1146/annurev.nucl.52.050102.090650.

[95] BEDDO M, et al. STAR: Conceptual design report for the Solenoidal Tracker at RHIC[J]. 1992.

[96] BEDDO M, et al. The star barrel electromagnetic calorimeter[J/OL]. Nucl. Inst. & Meth. A, 2003, 499(2):725 - 739. http://www.sciencedirect.com/science/article/pii/S0168900202019 708. DOI: https://doi.org/10.1016/S0168-9002(02)01970-8.

[97] BERGSMA F, et al. The STAR detector magnet subsystem[J/OL]. Nucl. Instrum. Meth. A, 2003, 499:633-639. DOI: 10.1016/S0168-9002(02)01961-7.

[98] RUAN L, et al. Perspectives of a Midrapidity Dimuon Program at RHIC: A Novel and Compact Muon Telescope Detector[J/OL]. J. Phys. G, 2009, 36:095001. DOI: 10.1088/0954-3899/36/9/095001.

[99] ANDERSON M, et al. The Star time projection chamber: A Unique tool for studying high multiplicity events at RHIC[J/OL]. Nucl. Instrum. Meth. A, 2003, 499:659-678. DOI: 10.1016/S0168-9002(02)01964-2.

[100] STAR Collaboration. A proposal for star inner tpc sector upgrade (itpc)[EB/OL]. https://drupal.star.bnl.gov/STAR/system/files/STAR_iTPC_proposal_06_09_2015.pdf.

[101] STAR Collaboration. Star inner tpc sector (itpc)[EB/OL]. https://drupal.star.bnl.gov/STAR/subsys/upgr/itpc.

[102] BICHSEL H. Stopping power and ranges of fast ions in heavy elements[J/OL]. Phys. Rev. A, 1992, 46:5761-5773. https://link.aps.org/doi/10.1103/PhysRevA.46.5761.

[103] BICHSEL H. A method to improve tracking and particle identification in TPCs and silicon detectors[J/OL]. Nucl. Instrum. Meth. A, 2006, 562:154-197. DOI: 10.1016/j.nima.2006.03.009.

[104] STAR collaboration. STAR images[EB/OL]. https://drupal.star.bnl.gov/STAR/book/export/html/7278.

[105] ARNOLD L, BAUDOT J, BONNET D, et al. The STAR silicon strip detector (SSD)[J/OL]. Nucl. Instrum. Meth. A, 2003, 499(2):652 - 658. http://www.sciencedirect.com/science/article/pii/S0168900202019630. DOI: https://doi.org/10.1016/S0168-9002(02)01963-0.

[106] CONTIN G, GREINER L, SCHAMBACH J, et al. The STAR MAPS-based PiXeL detector [J/OL]. Nucl. Instrum. Meth. A, 2018, 907:60 - 80. http://www.sciencedirect.com/science/article/pii/S0168900218303206. DOI: https://doi.org/10.1016/j.nima.2018.03.003.

[107] HAO Q. Status and Physics Opportunities of the STAR Heavy Flavor Tracker and the Muon Telescope Detector Upgrades[J/OL]. Journal of Physics: Conference Series, 2014, 509:012026. https://doi.org/10.1088%2F1742-6596%2F509%2F1%2F012026. DOI: 10.1088/1742-6596/509/1/012026.

[108] STAR collaboration. HFT Conceptual Design Report[EB/OL]. https://drupal.star.bnl.gov/STAR/starnotes/public/sn0600.

[109] ADAM J, et al. First Measurement of Λ_c baryon production in Au+Au collisions at $\sqrt{s_{NN}}$ = 200 GeV[J]. Phys. Rev. Lett., 2020, 124(17):172301.

[110] BRONIOWSKI W, FLORKOWSKI W. Geometric relation between centrality and the impact parameter in relativistic heavy-ion collisions[J]. Phys. Rev. C, 2002, 65:024905.

[111] STAR Run18 Au+Au 27 GeV centraltiy definition[EB/OL]. https://drupal.star.bnl.gov/STAR/system/files/Centrality_for_Run18_27GeVAuAu_ZaochenYe_20190827.pdf.

[112] STAR Run17 Au+Au 54.4 GeV centraltiy definition[EB/OL]. https://drupal.star.bnl.gov/ST AR/system/files/SWLan_Centrality.pdf.

[113] STAR collaboration. [EB/OL].

[114] ADAMCZYK L, et al. Measurements of Dielectron Production in Au+Au Collisions at $\sqrt{s_{NN}}$ = 200 GeV from the STAR Experiment[J/OL]. Phys. Rev. C, 2015, 92(2):024912. DOI: 10.1103/PhysRevC.92.024912.

[115] Low energy npe embedding request[EB/OL]. 20191701-04,.

[116] ADARE A, AFANASIEV S, AIDALA C, et al. Evolution of π^0 Suppression in Au + Au Collisions from $\sqrt{s_{NN}}$ = 39 to 200 GeV[J/OL]. Phys. Rev. Lett., 2012, 109:152301. https://link.aps.org/doi/10.1103/PhysRevLett.109.152301.

[117] Systematic measurements of identified particle spectra in pp, d + Au, and Au + Au collisions at the STAR detector, author = Abelev, B. I. and Aggarwal, M. M. and Ahammed, Z.[J/OL]. Phys. Rev. C, 2009, 79:034909. https://link.aps.org/doi/10.1103/PhysRevC.79.034909.

[118] ABELEV B, AGGARWAL M, AHAMMED Z, et al. Energy dependence of $\pi^{\pm}$, p and p^- transverse momentum spectra for Au+Au collisions at $\sqrt{s_{NN}}$ = 62.4 and 200 GeV[J]. Physics Letters B, 2007, 655(3):104 - 113.

[119] ADARE A, AFANASIEV S, AIDALA C. Neutral pion production with respect to centrality and reaction plane in Au+Au collisions at $\sqrt{s_{NN}}$ = 200 GeV[J/OL]. Phys. Rev. C, 2013, 87: 034911. https://link.aps.org/doi/10.1103/PhysRevC.87.034911.

[120] AIDALA C, AJITANAND N N. Production of π^0 and η mesons in Cu + Au collisions at $\sqrt{s_{NN}}$ = 200 GeV[J/OL]. Phys. Rev. C, 2018, 98:054903. https://link.aps.org/doi/10.1103/PhysRevC.98.054903.

[121] ADARE A, AFANASIEV S, AIDALA C, et al. Beam Energy and Centrality Dependence of Direct-Photon Emission from Ultrarelativistic Heavy-Ion Collisions[J/OL]. Phys. Rev. Lett., 2019, 123:022301. https://link.aps.org/doi/10.1103/PhysRevLett.123.022301.

[122] ANGELIS A, et al. Search for Direct Single Photon Production at Large p(T) in Proton Proton Collisions at $\sqrt{s_{NN}}$= 62.4 GeV[J/OL]. Phys. Lett. B, 1980, 94:106-112. DOI: 10.1016/0370-2693(80)90836-9.

[123] AKESSON T, et al. High $p_T \gamma$ and π^0 Production, Inclusive and With a Recoil Hadronic Jet, in pp Collisions at $\sqrt{s}$ = 63 GeV[J]. Sov. J. Nucl. Phys., 1990, 51:836-845.

[124] ANGELIS A, et al. Direct Photon Production at the CERN ISR[J/OL]. Nucl. Phys. B, 1989, 327:541-568. DOI: 10.1016/0550-3213(89)90305-2.

[125] PAQUET J F, SHEN C, DENICOL G S, et al. Production of photons in relativistic heavy-ion collisions[J/OL]. Phys. Rev. C, 2016, 93(4):044906. DOI: 10.1103/PhysRevC.93.044906.

[126] ADARE A, AFANASIEV S, AIDALA C, et al. Centrality dependence of low-momentum

direct-photon production in Au + Au collisions at $\sqrt{s_{NN}}$ = 200GeV[J]. Phys. Rev. C, 2015, 91:064904.

[127] Barrette, J. et al. Proton and pion production relative to the reaction plane in Au + Au collisions at 11A GeV/c[J]. Phys. Rev. C, 1997, 56:3254-3264.

[128] POSKANZER A M, VOLOSHIN S A. Methods for analyzing anisotropic flow in relativistic nuclear collisions[J]. Phys. Rev. C, 1998, 58:1671-1678.

[129] Adare, A. et al. Observation of Direct-Photon Collective Flow in Au + Au Collisions at $\sqrt{s_{NN}}$ = 200 GeV[J/OL]. Phys. Rev. Lett., 2012, 109:122302. https://link.aps.org/doi/10.1103/PhysRevLett.109.122302.

[130] XIE G. Charmed meson and baryon production in Au + Au collisions at $\sqrt{s_{NN}}$ = 200 GeV at RHIC[D]. USTC, 2017.

[131] CHEN X. Prompt and non-prompt D^0-meson production in Au+Au collisions at $\sqrt{s_{NN}}$ = 200 GeV at RHIC[D]. USTC, 2019.

[132] CACCIARI M, GRECO M, NASON P. The P(T) spectrum in heavy flavor hadroproduction [J/OL]. JHEP, 1998, 05:007. DOI: 10.1088/1126-6708/1998/05/007.

[133] FONLL calculation. [EB/OL]. http://www.lpthe.jussieu.fr/~cacciari/fonll/fonllform.html.

[134] SJÖSTRAND T, ASK S, CHRISTIANSEN J R, et al. An introduction to PYTHIA 8.2[J/OL]. Comput. Phys. Commun., 2015, 191:159-177. DOI: 10.1016/j.cpc.2015.01.024.

[135] SEYMOUR M H. The Higgs boson line shape and perturbative unitarity[J/OL]. Phys. Lett. B, 1995, 354:409-414. DOI: 10.1016/0370-2693(95)00699-L.

[136] ADAM J, et al. Elliptic flow of electrons from heavy-flavour hadron decays at midrapidity in Pb-Pb collisions at $\sqrt{s_{NN}}$ = 2.76 TeV[J/OL]. JHEP, 2016, 09:028. DOI: 10.1007/JHEP09(2016)028.

[137] ADAMS J, et al. Particle type dependence of azimuthal anisotropy and nuclear modification of particle production in Au + Au collisions at $\sqrt{s_{NN}}$ = 200 GeV[J/OL]. Phys. Rev. Lett., 2004, 92:052302. DOI: 10.1103/PhysRevLett.92.052302.

[138] ADAMCZYK L, et al. Elliptic flow of identified hadrons in Au+Au collisions at $\sqrt{s_{NN}}$ = 7.7-62.4 GeV[J/OL]. Phys. Rev. C, 2013, 88:014902. DOI: 10.1103/PhysRevC.88.014902.

[139] ABELEV B B, et al. Elliptic flow of identified hadrons in Pb-Pb collisions at $\sqrt{s_{NN}}$ = 2.76 TeV[J/OL]. JHEP, 2015, 06:190. DOI: 10.1007/JHEP06(2015)190.

[140] ABELEV B, et al. Centrality dependence of π, K, p production in Pb-Pb collisions at $\sqrt{s_{NN}}$ = 2.76 TeV[J/OL]. Phys. Rev. C, 2013, 88:044910. DOI: 10.1103/PhysRevC.88.044910.

[141] SONG T, BERREHRAH H, CABRERA D, et al. Tomography of the Quark-Gluon-Plasma by Charm Quarks[J/OL]. Phys. Rev. C, 2015, 92(1):014910. DOI: 10.1103/PhysRevC.92.014910.

[142] SONG T, BERREHRAH H, TORRES-RINCON J M, et al. Single electrons from heavy-flavor mesons in relativistic heavy-ion collisions[J/OL]. Phys. Rev. C, 2017, 96(1):014905. DOI: 10.1103/PhysRevC.96.014905.

[143] HE M, FRIES R J, RAPP R. Heavy-Quark Diffusion and Hadronization in Quark-Gluon Plasma[J/OL]. Phys. Rev. C, 2012, 86:014903. DOI: 10.1103/PhysRevC.86.014903.

[144] HE M, FRIES R J, RAPP R. Thermal Relaxation of Charm in Hadronic Matter[J/OL]. Phys. Lett. B, 2011, 701:445-450. DOI: 10.1016/j.physletb.2011.06.019.

[145] RIEK F, RAPP R. Quarkonia and Heavy-Quark Relaxation Times in the Quark-Gluon Plasma [J/OL]. Phys. Rev. C, 2010, 82:035201. DOI: 10.1103/PhysRevC.82.035201.

[146] VITEV I, GOLDMAN T, JOHNSON M B, et al. Open charm tomography of cold nuclear matter[J/OL]. Phys. Rev. D, 2006, 74:054010. https://link.aps.org/doi/10.1103/PhysRevD.74.054010.

[147] VOGT R. The A dependence of open charm and bottom production[J/OL]. Int. J. Mod. Phys. E, 2003, 12:211-270. DOI: 10.1142/S0218301303001272.

[148] ZENAIEV O, LISOVYI M, VERBYTSKYI A. Combined analysis of charm-quark fragmentation-fraction measurements[J/OL]. PoS, 2016, DIS2016:138. DOI: 10.22323/1.265.0138.

[149] AGGARWAL M M, et al. K^{*0} production in cu + cu and au + au collisions at $\sqrt{s_{NN}} = 62.4$ gev and 200 gev[J/OL]. Phys. Rev. C, 2011, 84:034909. https://link.aps.org/doi/10.1103/PhysRevC.84.034909.

[150] LIU S Y F, RAPP R. T-matrix Approach to Quark-Gluon Plasma[J/OL]. Phys. Rev. C, 2018, 97(3):034918. DOI: 10.1103/PhysRevC.97.034918.

[151] ADAMCZYK L, et al. Measurements of D^0 and D^* Production in $p + p$ Collisions at $\sqrt{s} = 200$ GeV[J/OL]. Phys. Rev. D, 2012, 86:072013. DOI: 10.1103/PhysRevD.86.072013.

[152] ACHARYA S, et al. Measurement of D^0, D^+, D^{*+} and D_s^+ production in Pb-Pb collisions at $\sqrt{s_{NN}} = 5.02$ TeV[J/OL]. JHEP, 2018, 10:174. DOI: 10.1007/JHEP10(2018)174.

[153] ACHARYA S, et al. D-meson azimuthal anisotropy in midcentral Pb-Pb collisions at $\sqrt{s_{NN}} = 5.02$ TeV[J/OL]. Phys. Rev. Lett., 2018, 120(10):102301. DOI: 10.1103/PhysRevLett.120.102301.

[154] SIRUNYAN A M, et al. Measurement of prompt D^0 meson azimuthal anisotropy in Pb-Pb collisions at $\sqrt{s_{NN}} = 5.02$ TeV[J/OL]. Phys. Rev. Lett., 2018, 120(20):202301. DOI: 10.1103/PhysRevLett.120.202301.

[155] AAD G, et al. Measurement of azimuthal anisotropy of muons from charm and bottom hadrons in Pb+Pb collisions at $\sqrt{s_{NN}} = 5.02$ TeV with the ATLAS detector[J/OL]. Phys. Lett. B, 2020, 807:135595. DOI: 10.1016/j.physletb.2020.135595.

[156] SIRUNYAN A M, et al. Nuclear modification factor of D^0 mesons in PbPb collisions at $\sqrt{s_{NN}}$ = 5.02 TeV[J/OL]. Phys. Lett. B, 2018, 782:474-496. DOI: 10.1016/j.physletb.2018.05.074.

[157] SIRUNYAN A M, et al. Studies of Beauty Suppression via Nonprompt D^0 Mesons in Pb-Pb Collisions at $Q^2 = 4\ GeV^2$[J/OL]. Phys. Rev. Lett., 2019, 123(2):022001. DOI: 10.1103/PhysRevLett.123.022001.

[158] SIRUNYAN A M, et al. Measurement of B_s^0 meson production in pp and PbPb collisions at $\sqrt{s_{NN}}$ = 5.02 TeV[J/OL]. Phys. Lett. B, 2019, 796:168-190. DOI: 10.1016/j.physletb.2019.07.014.

[159] ACHARYA S, et al. Λ_c^+ production in pp collisions at $\sqrt{s}$ = 7 TeV and in p-Pb collisions at $\sqrt{s_{NN}}$ = 5.02 TeV[J/OL]. JHEP, 2018, 04:108. DOI: 10.1007/JHEP04(2018)108.

[160] AAIJ R, et al. Prompt Λ_c^+ production in pPb collisions at $\sqrt{s_{NN}}$ = 5.02 TeV[J/OL]. JHEP, 2019, 02:102. DOI: 10.1007/JHEP02(2019)102.

[161] ACHARYA S, et al. Λ_c^+ production in Pb-Pb collisions at $\sqrt{s_{NN}}$ = 5.02 TeV[J/OL]. Phys. Lett. B, 2019, 793:212-223. DOI: 10.1016/j.physletb.2019.04.046.

[162] PLUMARI S, MINISSALE V, DAS S K, et al. Charmed Hadrons from Coalescence plus Fragmentation in relativistic nucleus-nucleus collisions at RHIC and LHC[J/OL]. Eur. Phys. J. C, 2018, 78(4):348. DOI: 10.1140/epjc/s10052-018-5828-7.

[163] OH Y, KO C M, LEE S H, et al. Heavy baryon/meson ratios in relativistic heavy ion collisions [J/OL]. Phys. Rev. C, 2009, 79:044905. DOI: 10.1103/PhysRevC.79.044905.

[164] LI H H, SHAO F L, SONG J, et al. Production of single-charm hadrons by quark combination mechanism in p-Pb collisions at $\sqrt{s_{NN}}$ = 5.02 TeV[J/OL]. Phys. Rev. C, 2018, 97(6): 064915. DOI: 10.1103/PhysRevC.97.064915.

[165] ZHAO J, SHI S, XU N, et al. Sequential Coalescence with Charm Conservation in High Energy Nuclear Collisions[J]. 2018.

[166] DJORDJEVIC M. Heavy flavor puzzle at LHC: a serendipitous interplay of jet suppression and fragmentation[J/OL]. Phys. Rev. Lett., 2014, 112(4):042302. DOI: 10.1103/PhysRevLett.112.042302.

[167] CAO S, QIN G Y, BASS S A. Modeling of heavy-flavor pair correlations in Au-Au collisions at 200A GeV at the BNL Relativistic Heavy Ion Collider[J/OL]. Phys. Rev. C, 2015, 92(5): 054909. DOI: 10.1103/PhysRevC.92.054909.

[168] KANG Z B, REITEN J, VITEV I, et al. Light and heavy flavor dijet production and dijet mass modification in heavy ion collisions[J/OL]. Phys. Rev. D, 2019, 99(3):034006. DOI: 10.1103/PhysRevD.99.034006.

[169] sPHENIX collaboration. sPHENIX Conceptual Design Report[EB/OL]. https://indico.bnl.g

ov/event/4640/attachments/18495/23200/sphenix-conceptual-design.pdf.

[170] sPHENIX Technical Design Report[EB/OL]. https://wiki.bnl.gov/sPHENIX/index.php/MAPS-based_Vertex_Detector_(MVTX)#Proposals.

[171] ABELEV B, et al. Technical Design Report for the Upgrade of the ALICE Inner Tracking System[J/OL]. J. Phys. G, 2014, 41:087002. DOI: 10.1088/0954-3899/41/8/087002.

[172] sPHENIX MVTX proposal[EB/OL]. https://wiki.bnl.gov/sPHENIX/index.php/MAPS-based_Vertex_Detector_(MVTX)#Proposals.

[173] CHO S, SUN K J, KO C M, et al. Charmed hadron production in an improved quark coalescence model[J/OL]. Phys. Rev. C, 2020, 101(2):024909. DOI: 10.1103/PhysRevC.101.024909.

[174] GHOSH S, DAS S K, GRECO V, et al. Diffusion of Λ_c in hot hadronic medium and its impact on Λ_c/D ratio[J/OL]. Phys. Rev. D, 2014, 90(5):054018. DOI: 10.1103/PhysRevD.90.054018.

[175] The STAR collaboration. Systematic measurements of identified particle spectra in pp, d + Au, and Au + Au collisions at the STAR detector[J]. Phys. Rev. C, 2009, 79(3):034909.

[176] The STAR collaboration. Identified Baryon and Meson Distributions at Large Transverse Momenta from Au + Au Collisions at $\sqrt{s_{NN}}$= 200 GeV[J]. Phys. Rev. Lett., 2006, 97(15): 152301.

[177] The STAR collaboration. Strangeness enhancement in Cu + Cu and Au + Au collisions at $\sqrt{s_{NN}}$= 200 GeV[J]. Phys. Rev. Lett., 2012, 108(7):072301.

Acknowledgements (致谢)

在科大和 LBNL 学习科研的这段时间里，值得感谢的老师、师兄师姐、同学、朋友很多，我能顺利完成学业离不开他们的帮助。

首先我要感谢我在科大的导师唐泽波副教授，他带领我敲开的高能物理的大门。从本科毕业设计开始做的探测器研发，到后来博士入门课题 D^* 分析，他给了我大量的指导。他思维敏锐、工作严谨，分析和硬件皆通，即便我即将毕业，也依旧是我在科研路上学习的榜样。我要特别感谢我在 LBNL 的导师董昕研究员，我博士论文的主要工作都是在董昕老师的指导下完成的。董昕老师学识渊博，工作效率高，总能准确定位出问题所在。他为我毕业论文的完成倾注了大量的心血，在他的精心指导和严格要求下，我的科研能力得到了很大的提升。另外我要感谢科大的李澄教授，邵明教授，周意副教授，孙勇杰副教授在硬件工作上的指导，以及科大的张一飞教授，LBNL 的许怒教授和 Grazyna Odyniec 研究员在分析和物理图像上提供的指导。我还要感谢国家留学基金委，我在 LBNL 交流的大部分生活费都是由他们资助的。

感谢我在科大的实验室同学在生活和科研上的帮助。特别感谢陈小龙和谢冠男师兄，在我刚开始入门 STAR 数据分析以及后来做 sPHENIX 模拟时候，两位师兄一直不厌其烦的解答我在工作上遇到的问题。他们的论文、note、代码以及严谨的工作态度，一直是我学习的典范。感谢刘圳和张生辉师姐，她们也是我在研究生期间最好的朋友之一，感谢她们在生活、科研上的交流和开导。感谢赵晓坤、王鹏飞、尤文豪、胡栋东师兄，在硬件工作方面的帮助和讨论。另外还要感谢科大的其他师兄，周龙，杨钱，杨帅，江琨，查王妹在科研工作上给过的建议和指导。

感谢实验室同级的同学和师弟师妹们，宋国峰，巨欣跃，吕游，洪道金，吴奕涛，周健，李子味，李洋，汪新建，曹泽华，王旭，魏凯，李子阳，胡天奇，梁政，沈凯峰，司凡，卢鹏忠，李秀君，吴鑫等等。特别是周健同学，他是我论文答辩的秘书。在 2020 年这个特别的年度，他帮我操办了很多毕业需要的手续，没有他的帮助我无法顺利的进行答辩，同时也感谢其他师弟师妹为此提供过的帮助和支持。在科大的时光，和实验室的小伙伴们一起开文献阅读会、一起上课、郊游，是我研究生期间最愉快的回忆。

感谢我在 LBNL 的工作伙伴，梁裕恒，梁悦，张宇，兰少卫，杨贞贞，Sooraj Radhakrishnan，Matthew Kelsey，谢冠男，和巨欣跃。特别是巨欣跃和梁悦同学，在伯克利和 BNL 时候，在生活上给了我很多帮助。

感谢 STAR 和 sPHENIX 国际合作组，在合作组我学到了很多其他领域无法

提供的东西。感谢 Petr Chaloupka，马荣荣和 Sooraj Radhakrishnan，他们在 STAR Heavy Flavor PWG 担任 convenor 期间，对我在 STAR 的分析工作以及各类报告能够耐心的提出修改意见。感谢 sPHENIX Heavy Flavor convenor 黄进研究员，他为我解答了很多 sPHENIX 技术方面的问题，并且耐心的对我的 QM 报告和 proceeding 提出修改意见，他的软件水平是我学习的标杆。

感谢在 BNL 开会和值班期间认识的小伙伴们，感谢大家在生活和科研规划上提供的交流和建议，感谢曾经的 8A 公寓，解决了不会开车的孩子在没有餐厅的 BNL 值班的生存问题，BNL 小火锅是我在美国最快乐的时光之一。

最后，我要感谢我的父母，没有你们一直以来的支持，我无法顺利完成学业，感谢你们在我情绪低落的时候鼓励我、开导我。

Publications and Presentations List

Publications

1. A novel fast response and radiation-resistant scintillator detector for beam loss monitor

   Y. Ji et al. Journal of Instrumentation, 2017, 12(07):C07042

2. Heavy flavor physics with the sPHENIX MAPS vertex tracker upgrade

   Y. Ji (for the sPHENIX Collaboration), Nuclear Physics A, 2020, xx(xx):xx (Accepted)

3. First Measurement of Λ_c Baryon Production in Au + Au Collisions at $\sqrt{s_{NN}} =$ 200 GeV (Principal Author)

   The STAR Collaboration. Phys. Rev. Lett. 2020, 124(17):172301

Prepare to publish

1. Elliptic flow of electrons from heavy-flavor decays in 54.4 and 27 GeV Au+Au collisions from the STAR Measurement (Principal Author)

   Target Journal: Physics Letter B.

2. D^{*+} and D^+ measurements at Au+Au 200 GeV measured by the STAR experiment (Principal Author)

   Target Journal: Physical Review C.

Presentations

1. A novel fast response and radiation-resistant scintillator detector for beam loss monitor (poster)

   International Conference on Instrumentation for Colliding Beam Physics 2017 (INSTR17), Feb 27-Mar 3, Novosibirsk, Russia.

2. D^{*+} production at Au+Au 200 GeV in STAR experiment (poster)

   The XXVIIth International Conference on Ultra-relativistic Nucleus-Nucleus Collisions (Quark Matter 2018), May 14-19, 2018, Venice, Italy.

3. D^{*+} production at Au+Au 200 GeV in STAR experiment (talk)

   2018 年中国物理学会高能物理学术年会，June 20-40, Shanghai, China.

4. Simulation of Λ_c production at sPHENIX (talk)

   American Physical Society April Meeting 2019, April 12-14, Denver, US.

5. Future Heavy Flavor and Quarkonia Measurements from sPHENIX (talk)
   RHIC & AGS Annual User Meeting 2019, June 4-7, Upton (BNL), US.

6. Elliptic flow of electrons from heavy-flavor decays in 54.4 GeV Au+Au colli-sions from the STAR (poster)
   The XXVIIIth International Conference on Ultra-relativistic Nucleus-Nucleus Collisions (Quark Matter 2019), Nov 4-9, Wuhan,China.

7. Heavy flavor physics with the sPHENIX MAPS vertex tracker upgrade (talk)
   The XXVIIIth International Conference on Ultra-relativistic Nucleus-Nucleus Collisions (Quark Matter 2019), Nov 4-9, Wuhan,China.

8. Elliptic flow of electrons from heavy-flavor decays in 54.4 and 27 GeV Au+Au collisions from the STAR (talk)
   The 10th International Conference on Hard and Electromagnetic Probes of High-Energy Nulcear Collisions (Hard Probes 2020), June 1-5, Online.

9. Simulation of Λ_c production at sPHENIX (poster)
   The 10th International Conference on Hard and Electromagnetic Probes of High-Energy Nulcear Collisions (Hard Probes 2020), June 1-5, Online.